MAGNETOM Flash

Issue Number 72 · 1/2019
SCMR Edition

siemens.com/magnetom-world

Page 04
Editorial Comment
James Carr

Page 08
Adding Value in CMRI with BioMatrix
Johan Dehem

Page 14
Impact of CS Cardiac Cine in a Busy Clinical Practice
Jérome Garot

Page 18
Motion-corrected Whole-heart Simultaneous Cardiac MR/PET Imaging
Camila Munoz, et al.

Page 34
Imaging MINOCA
Jeanette Schulz-Menger, et al.

Page 38
Cardiotoxicity in Cancer Therapy
Bernd Wintersperger, et al.

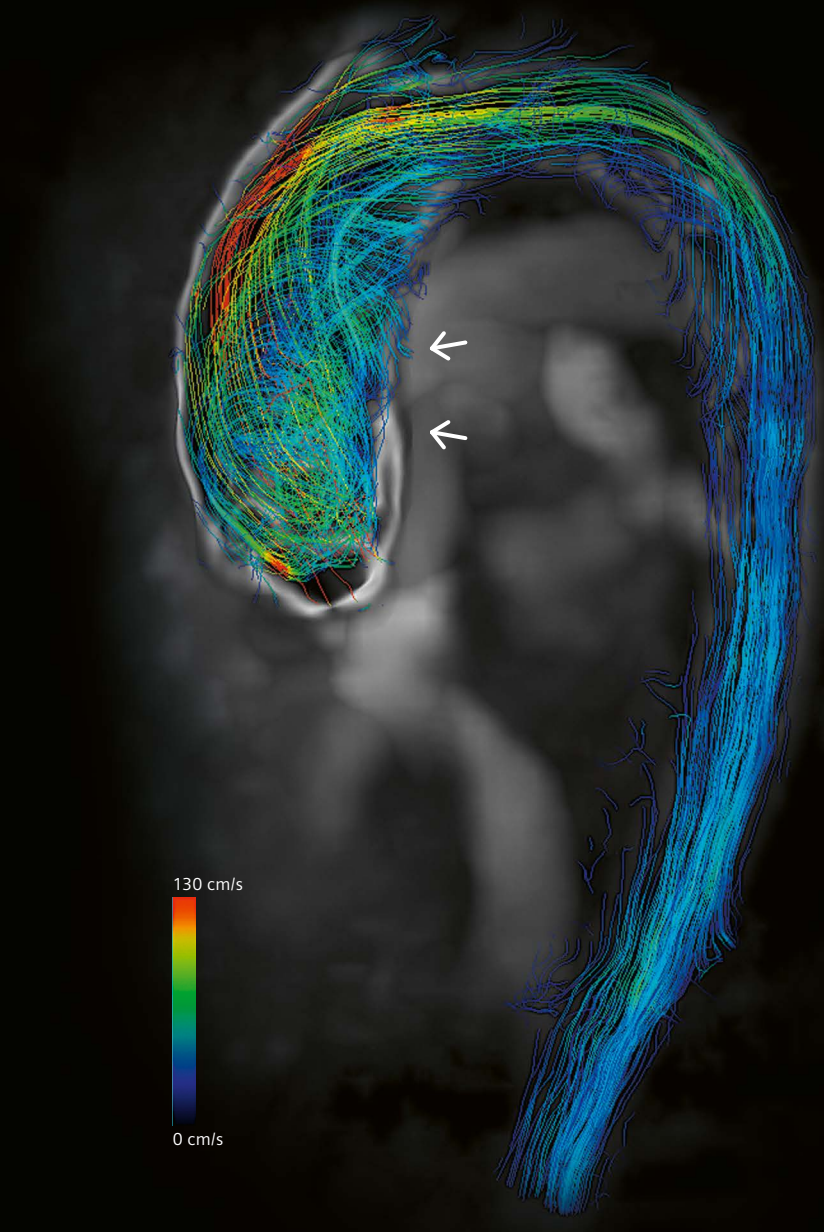

SIEMENS Healthineers

Contents

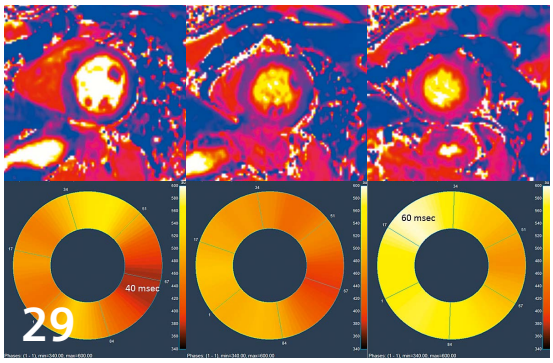

Reference normal values for myocardial T1 and T2 maps

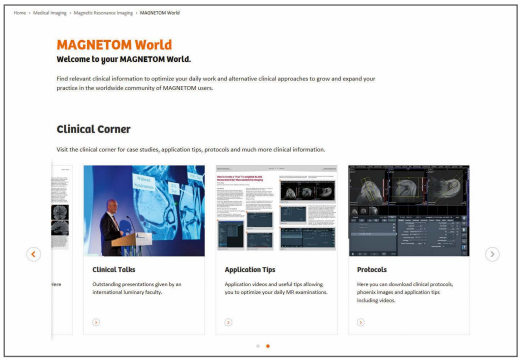

Learn from the experience of other MAGNETOM users

The MAGNETOM World is the community of Siemens Healthineers MR users worldwide, providing you with relevant clinical information. Here you will find application tips and protocols to optimize your daily work. Lectures and presentations from experts in the field will allow you to be exposed to new ideas and alternative clinical approaches.

Put the advantages of the MAGNETOM World to work for you!

siemens.com/magnetom-world

Editorial Comment

4 *James C. Carr, Northwestern University, Feinberg School of Medicine, Chicago, IL, USA*

Cardiovascular Imaging

8 **Adding Value to CMRI with MAGNETOM Sola's BioMatrix Technology**
Johan Dehem, VZW Jan Yperman, Ypres, Belgium

14 **Impact of Compressed Sensing Cardiac Cine in a Busy Clinical Practice**
Jérome Garot, Gilles Auvray, Institut Cardiovasculaire Paris Sud, Massy, France

18 **Motion-corrected Whole-heart Simultaneous Cardiac MR/PET Imaging: Initial Clinical Experience**
Camila Munoz, et al., King's College London, United Kingdom

29 **Reference Normal Values for Myocardial T1 and T2 Maps with the MAGNETOM Vida 3T System and Case Examples from Clinical Practice**
Guillem Pons-Lladó, Clínica Corachán, Barcelona, Spain

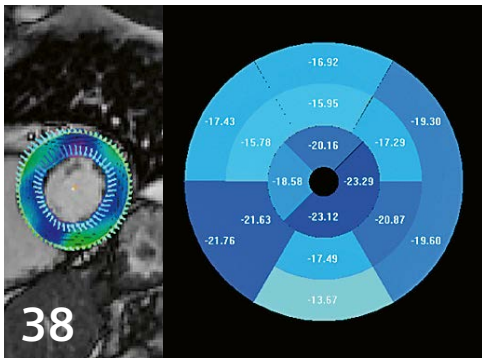

Cardiotoxicity in cancer therapy

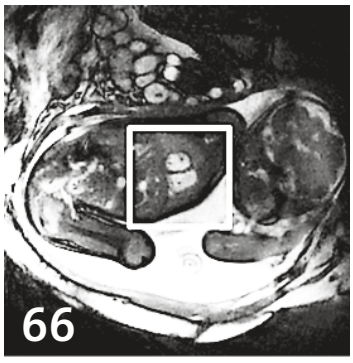

Fetal cardiac MRI[1]

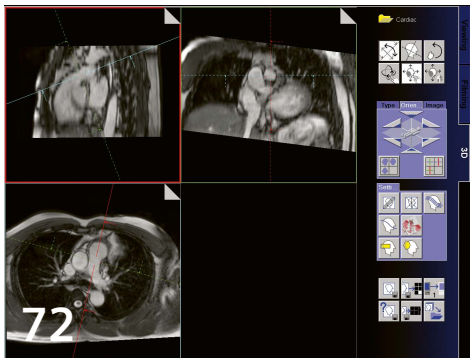

3D Localization for cardiac views

34 **MINOCA. Myocardial Infarction with Non-Obstructive Coronary Arteries**
Edyta Blaszczyk, Jeanette Schulz-Menger, University Medicine Berlin, Charité Campus Buch, HELIOS Clinics Berlin Buch, Germany

38 **Cardiovascular Magnetic Resonance – Cardiotoxicity in Cancer Therapy**
Bernd J. Wintersperger, et al., University Health Network, Toronto, Canada

43 **CMR and Cardiotoxicity. A Case-based Overview**
Fabian Muehlberg, Jeanette Schulz-Menger, University Medicine Berlin, Charité Campus Buch, HELIOS Clinics Berlin Buch, Germany

45 **Unusual Atrial Myxoma with Neovascularization Associated with Fistula to Right Atrium**
Pairoj Charanukulchai, Kanokvalee Ponkanist, Chulalongkorn University, Bangkok, Thailand

48 **Clinical Usefulness of 4D Flow[2] in Adult Cardiovascular MRI**
Stephanie Funk, Jeanette Schulz-Menger, University Medicine Berlin, Charité Campus Buch, HELIOS Clinics Berlin Buch, Germany

Pediatric Imaging

52 **4-Dimensional Phase Contrast Imaging[2] in Congenital Heart Disease: How we do it[1]**
Timothy C. Slesnick, et al., Emory University School of Medicine, Atlanta, GA, USA

66 **Small Structures, Big Challenges: Fetal Cardiac Magnetic Resonance Imaging[1]**
Matthias Stuber, et al., University of Lausanne, Lausanne, Switzerland

How-I-do-it

72 **3D Localization for Cardiac Views: Saving Time While Increasing Accuracy**
Julian Gan, Siemens Healthineers, Singapore

78 **The Various Definitions of TR**
Gary R. McNeal, Siemens Healthineers, Chicago, IL, USA

Meet Siemens Healthineers

87 **Introducing Michaela Schmidt and Carmel Hayes**, Development of cardiovascular applications, Siemens Healthineers, Erlangen, Germany

[1]Siemens Healthineers disclaimer does not represent the opinion of the authors: MR scanning has not been established as safe for imaging fetuses and infants less than two years of age. The responsible physician must evaluate the benefits of the MR examination compared to those of other imaging procedures.
[2]WIP, the product is currently under development and is not for sale in the US and in other countries. Its future availability cannot be ensured.

James C. Carr

James C. Carr, M.D., is Chair of the department of Radiology and Professor of Radiology, Medicine and Biomedical Engineering at Northwestern University Feinberg School of Medicine and McCormick School of Engineering in Chicago, Illinois, USA.

Dr. Carr is an investigator on multiple federal and industry health grants. His research focuses on the development and clinical evaluation of techniques for cardiac and vascular magnetic resonance imaging (MRI).

He also directs fellowship programs in cardiovascular imaging and in clinical/research MRI, for which he has mentored over 70 clinical and research fellows at Northwestern University.

Dear readers and colleagues,

It has now been nearly two decades since cardiovascular MRI (CMR) emerged onto the clinical scene as a ground breaking tool for imaging the cardiovascular system and, since then, has become a mainstay clinical modality for assessing cardiovascular disease, particularly for common indications such as ischemic heart disease and heart failure. CMR is considered the gold standard for measurement of left ventricular function and is the only modality that can reliably detect myocardial scar, which is a proven marker of existent disease and future adverse events. More recently, with the advent of clinically useful mapping techniques, such as T1, T2 mapping and extracellular volume calculation, CMR can detect fibrosis at the microscopic interstitial level which is particularly useful in heart failure and can be diagnostic in infiltrative disorders such as amyloidosis. There still remains significant obstacles to widespread adoption of CMR as a routine diagnostic tool however, with the recent maturation of newer technologies, many of these barriers may soon be circumvented.

A major hurdle to widespread adoption of CMR as a routine diagnostic test is that it is still a complex diagnostic study that is time consuming and therefore not considered 'routine'. The standard protocol typically consists of multiplanar cine imaging of the heart followed by post contrast delayed enhanced imaging of the left ventricle for detection of myocardial scar. Using current techniques, each image is acquired as a breath-hold such that CMR is most suitable for cooperative patients who are in regular sinus rhythm. The entire protocol itself is long, typically taking 45–60 minutes and knowledge of cardiac anatomy and pulse sequence detail is essential in order to achieve a successful diagnostic study. As a result of this complexity, CMR is still mostly performed in larger academic institutions and has not penetrated community practices to any significant degree. This may all be about to change with the advent of recently introduced new technologies. Firstly, compressed sensing acceleration is now becoming available clinically and has the potential to speed up the routine CMR exam at all stages of the protocol. Compressed sensing CMR may allow the entire heart to be imaged in a single-breath hold or alternatively may allow real time free breathing cine MRI at image quality comparable to routine segmented cine MRI. Secondly, self gating approaches to respiratory and cardiac gating[1], whereby motion is recorded in-line during the MRI acquisition, may facilitate 'leadless' cardiac imaging during free breathing, thereby obviating the need for ECG lead placement and markedly simplifying and shortening the entire CMR protocol. Thirdly, automated computer algorithms have recently been made available at the user interface level, where cardiac imaging planes are set up automatically, thereby simplifying the exam for the technologist. With some of these new advances, leadless rapid 3D cine and 3D delayed enhanced imaging with automated slice reconstruction all in less than 15 minutes may soon become available. The article by Bianchi et al in the current edition of MAGNETOM Flash illustrates how these techniques can be pushed to the limit and employed together to visualize a particularly challenging anatomic structure, the fetal heart.

[1] *WIP, the product is currently under development and is not for sale in the US and in other countries. Its future availability cannot be ensured.*

Dr. Carr has served on national, international and institutional committees related to research and education, including those of the American Heart Association, the American College of Radiology, the Society of Cardiovascular MR, and the International Society for Magnetic Resonance in Medicine. He is a past president of the Society for Magnetic Resonance Angiography and has delivered over 200 invited presentations on cardiovascular MRI in the U.S. and around the world.

Another challenge with CMR is the need for accurate and reproducible quantification of image data yielding measurement parameters such as ejection fraction and ventricular volumes, which are essential for predicting patient outcomes. Such quantification is laborious and time consuming for the imaging physician, resulting in prolonged report turnaround times and poor workflow. Some centers have created dedicated 3D labs for post-processing of CMR images by 'super' techs, thereby relieving imaging physicians from time consuming post-processing tasks. More recently, in-line post-processing algorithms have been developed that allow automated post-processing of images, once they are acquired. While early implementations of these tools have not been widely adopted, the technology has matured such that results are significantly more accurate and promise to greatly simplify the CMR workflow.

The overall availability of MRI equipment and expertise continues to hamper utilization of CMR. MRI scanners are expensive and therefore widespread proliferation of these devices is limited. Furthermore, since access to MRI is limited, CMR usually has to compete with other more common indications for MRI such as neuroimaging or body imaging studies. Dedicated CMR scanners are now becoming available, which are less expensive and easier to install compared to standard scanners, making it more attractive for hospitals to dedicate specific pieces of equipment to specialized studies such as cardiac imaging. Additionally, traditional rigid coils may soon be replaced by flexible 'blanket' style coils which cover a greater anatomic region and are easier for the patient to wear. The availability of CMR expertise at physician and technologist level is also a significant factor preventing utilization of CMR, particularly in community practices. Societies have been effective in developing training courses and exams to increase expertise of existing users and train new people however, the availability of new personnel, particularly technologists, continues to be a challenge. An interesting recent development that may overcome this problem has been the creation software and hardware that allows remote operation of MRI scanners. This may allow supervision of inexperienced technologists by an experienced operator that is located at a separate central site or complete remote operation of a scan if a CMR technologist is not available. In some instances, virtual operating centers have been created whereby scanners in remote poorly populated regions are controlled by technologists from a central geographically separate location.

With these advances, we are on the cusp of attaining the simple, rapid CMR protocol where leadless free breathing cine and delayed enhanced imaging with automated plane selection, image reconstruction and in line automatic processing of CMR-derived quantitative data may soon become a reality.

With these advances mentioned above, we are on the cusp of attaining the simple, rapid CMR protocol where leadless free breathing cine and delayed

enhanced imaging with automated plane selection, image reconstruction and in-line automatic processing of CMR-derived quantitative data may soon become a reality. So, what does the future hold for CMR?

It is hard to discuss the future of medicine without first addressing artificial intelligence (AI) and deep learning, which promises to make a significant impact on imaging and diagnostic medicine in general. AI algorithms have already been developed to automatically analyze plain radiographs of the chest with high degrees of accuracy. While tools to automatically read CMR studies seem unlikely to become available in the near term, AI will likely make its initial impact on CMR in the area of automated processing of image data. Algorithms which trace the endocardial and epicardial borders of the left ventricle with high degrees of accuracy have already been developed and will likely be extended to areas such as scar quantification, mapping, flow and regional function. This development is welcome and will greatly simplify the CMR protocol, increasing its utilization by the wider medical community and making it more available to patients that need it. A less visible benefit lies with pulse sequence development and quality control of CMR. AI algorithms can learn to automatically alter parameters to improve pulse sequence performance according to a predetermined set of rules or may be used to automatically detect poor quality non-diagnostic images such that they can be re-acquired with optimized settings, preventing the patient returning for a repeat study. AI can also be used to analyze radiomic features in images, such as texture and intensity, which are not visible to the naked eye and combine this with functional information or genetic profiles to better characterize the abnormality or predict outcomes. This has been done effectively in oncology, particularly for breast cancer and glioblastoma multiforme, helping predict different grades of tumor.

Hybrid systems, such as MR-PET, will facilitate the combination of structure-function imaging with MRI and molecular imaging with PET, opening the gates to true diagnostic precision medicine.

Several newer techniques, such as 4D Flow[1] MRI and tissue mapping, may help us better characterize cardiovascular disease and develop several new clinical applications. Current 4D Flow MRI techniques are long and complex (therefore not practical clinically) however newer implementations incorporating compressed sensing[1] have reduced acquisition times to 1 minute or less in certain instances. This makes it possible to integrate 4D Flow into the routine CMR protocol without significantly lengthening the overall protocol. This technique has proven to be useful clinically in regions and pathologies where the cardiovascular anatomy is complex, such as congenital heart disease or thoracic aortic aneurysms. Novel imaging biomarkers, such as wall shear stress and energy loss, can be derived from 4D Flow MRI data and may help us better understand mechanisms of certain diseases such as aneurysm formation associated with bicuspid aortic valve disease. The article by Funk et al. in this current edition of MAGNETOM Flash outlines current clinical usefulness of 4D Flow MRI. With recently developed mapping techniques, T1 and T2 can be measured quantitatively in different tissues and can be used to more accurately characterize pathology and normal tissue structures. In particular, T1 and extracellular volume fraction (ECV) are quantitative values derived from CMR images, which tell us whether interstitial fibrosis is present and help better characterize the phenotypic make up of the myocardium. This has been particularly useful in conditions such as amyloidosis and hypertrophic cardiomyopathy.

As a result of the introduction of novel techniques and acceleration strategies, newer applications have been introduced to CMR. T2 mapping, which is useful in inflammatory conditions causing edema, can be used to detect acute rejection in the transplant heart without the need for invasive biopsy, which is potentially dangerous and expensive. T1 mapping and ECV has been employed in cardio-oncology to detect which patients are more likely to develop cardiotoxicity following doxorubicin or other chemotherapy administration. Similarly, wall shear stress derived from 4D Flow data can detect which portions of the thoracic aorta are likely to become aneurysmal in patients with bicuspid aortic valve disease.

Molecular imaging of the heart allows detection of abnormalities at the ultrastructural cellular level using targeted tracers (e.g. radio-isotopes) or contrast agents. Newer hybrid systems, such as MR-PET, will facilitate the combination of structure-function imaging with MRI and molecular imaging with PET, opening the gates to true diagnostic precision medicine. In this edition of MAGNETOM Flash the article by Munoz et al.

[1] *WIP, the product is currently under development and is not for sale in the US and in other countries. Its future availability cannot be ensured.*

explores a novel motion corrected MR-PET acquisition for simultaneous visualization of coronary artery anatomy and myocardial scar. MR-PET is already become more routine for evaluating cardiac sarcoidosis and newer tracers that target the sympathetic and parasympathetic nervous systems may help map out neural tissue in the heart and predict which patients will develop arrhythmia.

In summary, the future of CMR looks very promising and will increasingly play an integral role in the evaluation of patients with cardiovascular disease. Recently developed techniques based on compressed sensing will markedly shorten and simplify the CMR protocol increasing its utilization and making it more broadly available to the widely community. AI strategies will not only improve workflow and make high quality imaging routine but will also help us extract previously invisible radiomic features that will better characterize cardiovascular disease.

James C. Carr

References

1 Evaluation of myocardial viability by MRI. Kim RJ, Hillenbrand HB, Judd RM. Herz 2000. Jun;25(4):417-30.
2 4D flow MRI. Markl M, Frydrychowicz A, Kozerke S, Hope M, Wieben O., J Magn Reson Imaging. 2012 Nov;36(5):1015-36.
3 Automatic quantification of the LV function and mass: A deep learning approach for cardiovascular MRI. Curiale AH, Colavecchia FD, Mato G. Comput Methods Programs Biomed. 2019 Feb;169:37-50.

We appreciate your comments.
Please contact us at magnetomworld.team@siemens-healthineers.com

Editorial Board

Review Board

Adding Value to CMRI with MAGNETOM Sola's BioMatrix Technology

Johan Dehem, M.D.

VZW Jan Yperman, Ypres, Belgium

Grasping the anatomy and physiology of moving organs to visualize dynamic contrast enhancement during free breathing is an excellent example of the added value of compressed sensing. Another great illustration of how compressed sensing brings new value can be found in cardiac imaging.

The value of this technology can also be found in terms of patient comfort. Scanning the left ventricle short axis with standard segmented TrueFISP Cine entails the patient holding their breath ten times. Using Compressed Sensing Cardiac Cine TrueFISP in high resolution, the same short axis scan only takes two breath-holds. Furthermore, table time for a standard scan, for example for ischemic heart disease, drops from more than 30 to less than 20 minutes due to this drastic reduction in breath-holds, which also results in increased patient comfort. As it is possible to scan five slices in the same breath-hold, we scan significantly more long axis views than before giving my referring cardiologists all the cines they love so much. Adding value in diagnostic confidence!

It is possible to achieve consistent, good results even in patients who don't necessarily follow a healthy diet (Fig. 1). BioMatrix Technology and high-density coils ensure the signal, while Compressed Sensing enables short breath-holds or, even better, free breathing acquisition, which was previously not possible.

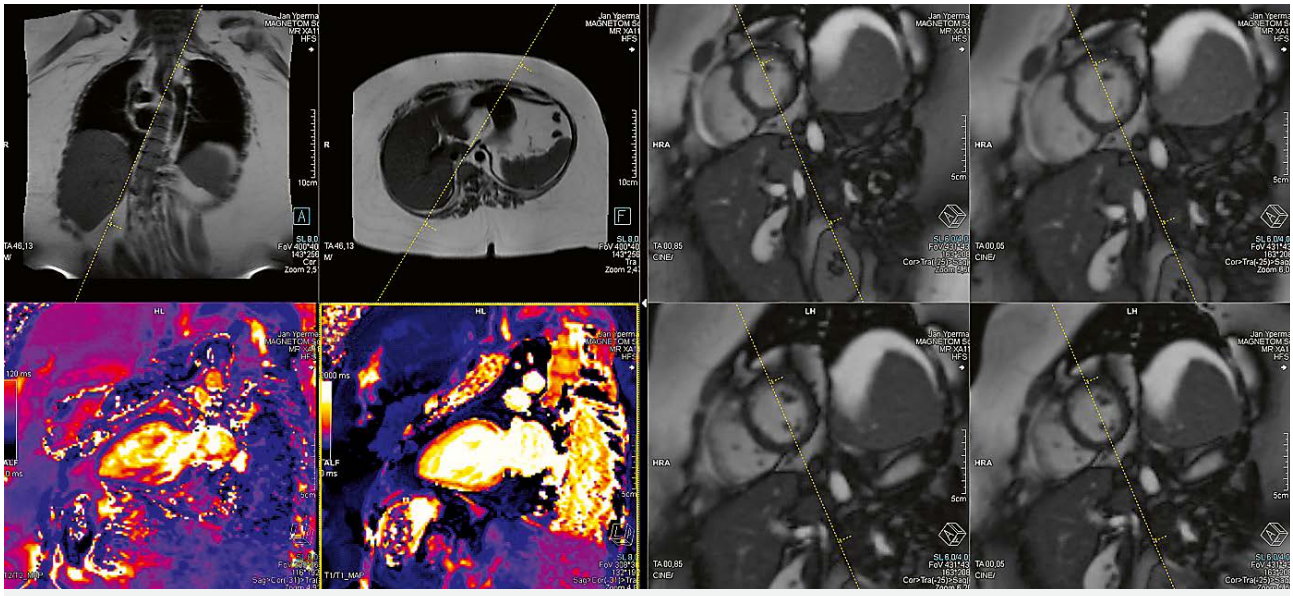

Figure 1:
This very obese patient has atypical retrosternal pain. Transthoracic ultrasound of the heart was considered "non-diagnostic" due to obesity. The large bore of 1.5T MAGNETOM Sola is indispensable to accommodating this patient, as you can see in the left part of the image. The right part of the image shows free-breathing real-time Compressed Sensing Cardiac Cine with adaptive triggering. Acquisition time per slice varies (depending on the adaptive triggering) between 0.05 and 0.85 seconds.

Even in patients who cannot hold their breath at all, and in patients with severe arrhythmia, this adaptive triggering variant effectively eliminates all motion artifacts. Real-time cardiac imaging has finally achieved long-sought after quality and robustness with high spatial and temporal resolution. Referring physicians have quickly learned that cardiac MRI in patients with severe dyspnea or very low ejection fraction, for example, is also feasible. Since many of these patients are bedridden, access to scans is fortunately facilitated by the BioMatrix Dockable Table with e-drive.

Compressed Sensing Cardiac Cine really is a no-brainer: Patients prefer it, referring cardiologists prefer it, and very ill patients have easy access to cardiac MRI – a clearcut winner! In addition, MAGNETOM Sola has other cardiac tricks up its sleeve: PSIR HeartFreeze, the latest advancement, delivers delayed enhancement images acquired in free breathing in crisp and clear high resolution. There was previously an option for high resolution delayed enhancement; it required, however, a breath-hold for every slice, which took too long for sick patients. The high-end motion correction algorithm of PSIR HeartFreeze eliminates this problem.

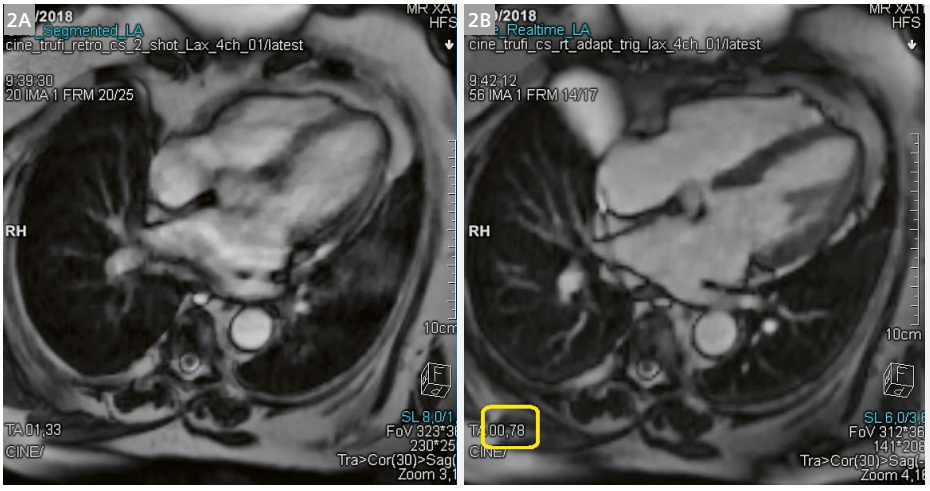

Figure 2:
This patient was simply too nervous to cooperate **(2A)** when running the standard retrogated Compressed Sensing Cardiac Cine TrueFISP. Changing gears to Compressed Sensing Cardiac Cine TrueFISP with adaptive triggering **(2B)** is a simple, yet effective tool to eliminate breathing and arrhythmia artifacts. Time of acquisition for the 4-chamber-view with adaptive triggering: 0.78 seconds (yellow box).

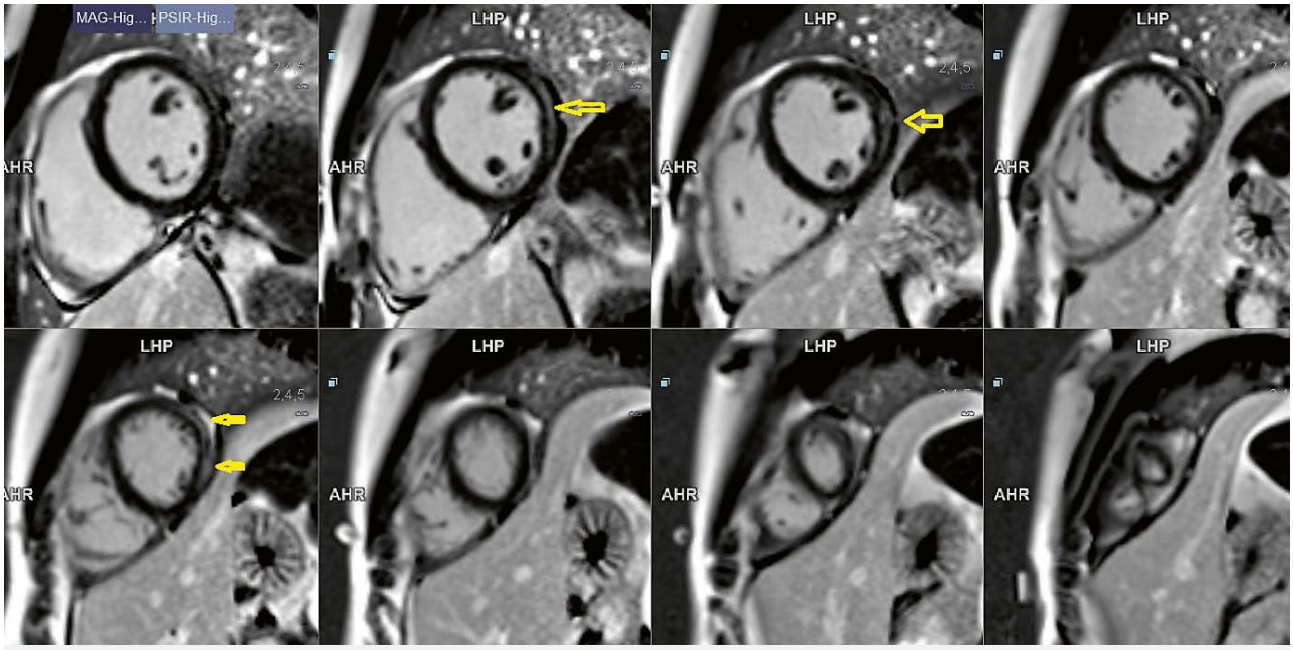

Figure 3:
Myocarditis. Typical epicardial delayed enhancement. Although early on admission, high quality PSIR HeartFreeze reveals the diseased myocardium during free breathing. The high quality also makes it easy to delineate and, therefore, quantify the scar burden as seen in Figure 4.

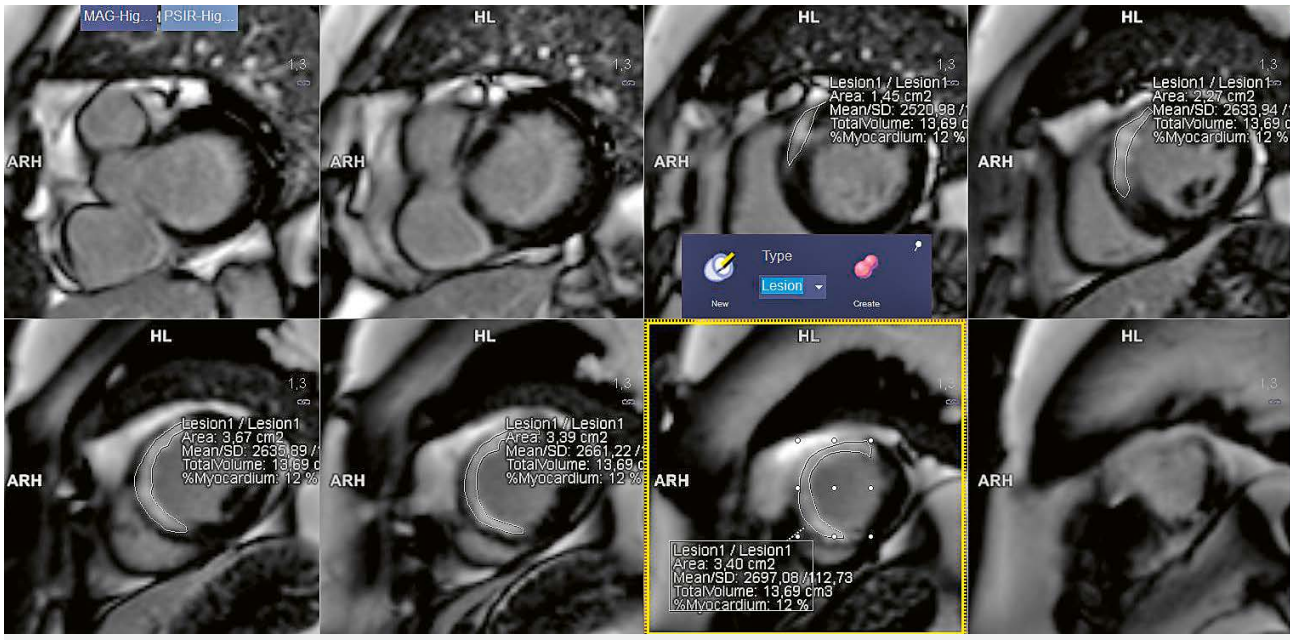

Figure 4:
Delayed enhancement using PSIR HeartFreeze. Finally, it is easy to delineate and quantify the extension of the LAD infarction. Here we calculate a volume of 14 cm³ corresponding to 12% myocardial infarction.

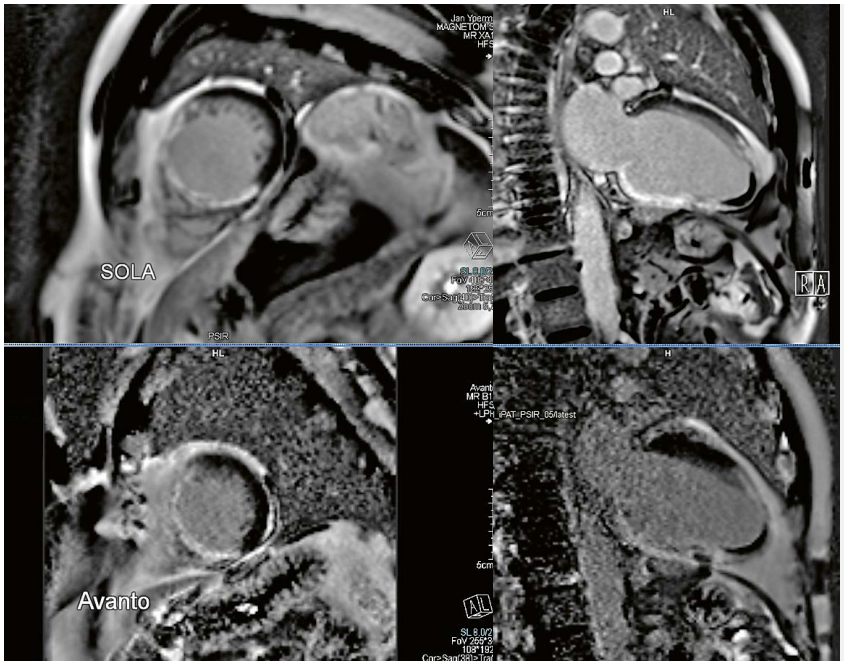

Figure 5:
Non-cooperative patient, history of abuse, admitted after resuscitation and STEMI infarction. Acute phase: on MAGNETOM Avanto, breath-hold PSIR TrueFISP, sax and 2-chamber-view (lower row) with respiration artifacts.

Follow-up exam on MAGNETOM Sola (top row) with PSIR HeartFreeze accurately delineates large scar burden with no-reflow phenomenon.

Comparing classic delayed enhancement imaging with PSIR HeartFreeze says it all! Before PSIR HeartFreeze, multiple breath-holds were required in sick patients as shown in Figure 5.

While comparing recent exams with older exams it is striking to see how MAGNETOM Sola improves detection and reading of cardiac lesions. Just like in the case of this follow-up exam for myocarditis (Fig. 6).

Cardiac amyloidosis used to be a difficult diagnosis, especially since amyloidosis has such a dramatic impact on the heart function and, hence, on the condition and cooperation of your patient. The ability to scan during free breathing brought to scanning cardiac amyloidosis the convenience we had always hoped for.

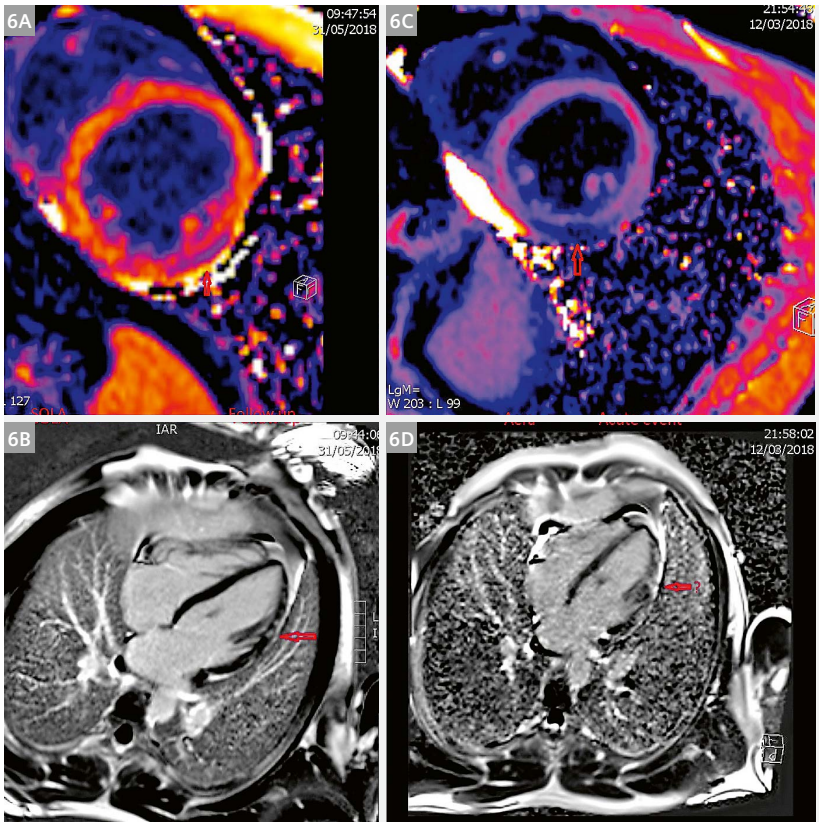

Figure 6:
Myocarditis acute phase T1 mapping with MyoMaps and delayed enhancement imaging on MAGNETOM Aera **(6C, D)** Myocarditis follow-up T1 mapping with MyoMaps and PSIR HeartFreeze acquired on MAGNETOM Sola **(6A, B)**. Conspicuity of the lesions on MAGNETOM Sola is dramatically improved despite pronounced regression of lesions (T1 map post-gadolinium, **6C**, red arrows).

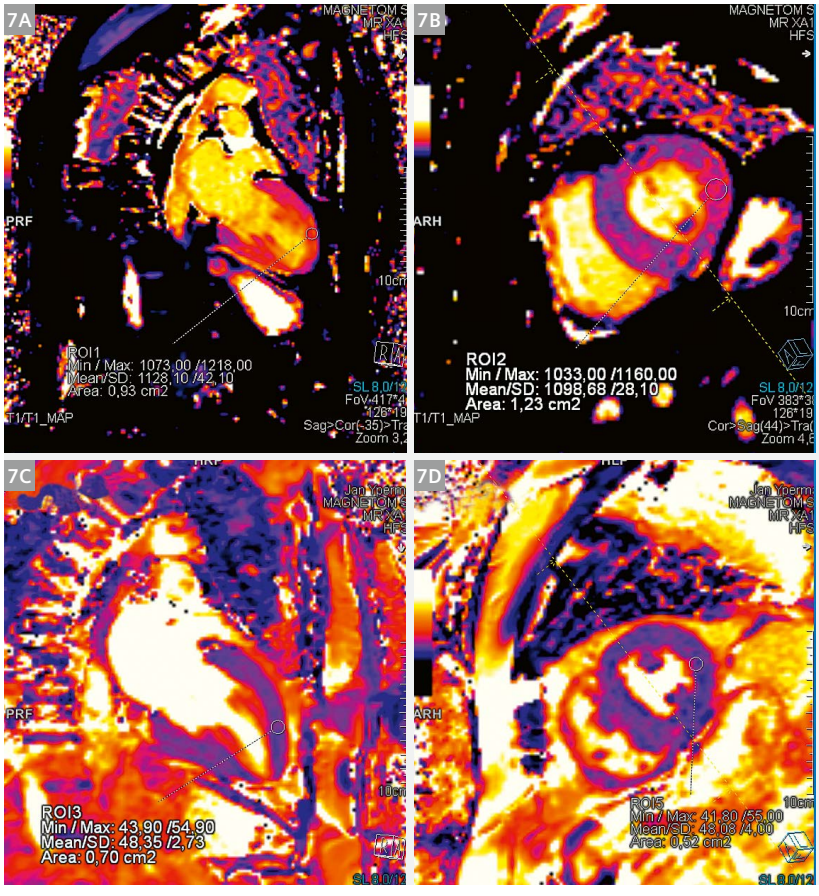

Figure 7:
82-year-old male with severe shortness of breath. T1 native (T1 mapping with MyoMaps) is increased up to 1128 **(7A)** while T2 value (T2 mapping with MyoMaps) is normal, not increased **(7C)**. Classic finding for cardiac amyloidosis.

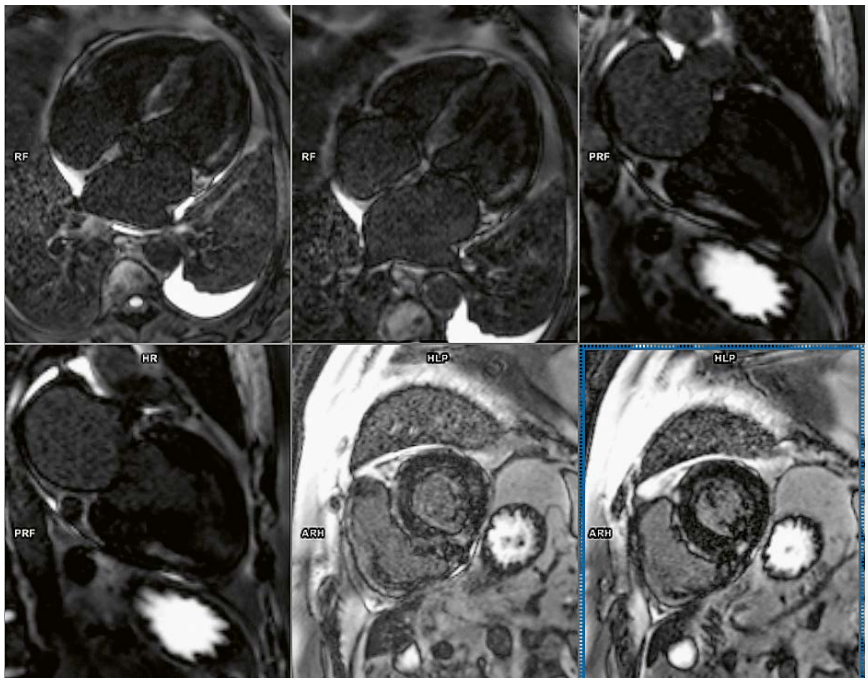

Figure 8:
Classic, long known finding in a case of cardiac amyloidosis: Diffuse infiltrated myocardium, hard to "null" on the delayed enhancement. PSIR HeartFreeze free breathing acquisition at least provides images without motion artifacts. Please note that this patient is in very poor health and has an ejection fraction of 16.78%!
See Figure 9.

Finally, all of this high-end cardiac imaging is neatly packaged in the Cardiac Dot Engine, which is easy to handle even for my junior technologist who just started last month. Although automatic planning of cardiac views may seem boring to some operators, seeing errors often dramatically reduced and interoperator results becoming way more consistent eliminates any potential doubt. Also, it allows the operator time to give their full attention to the patient.

	Absolute values	BSA normalized values
Ejection fraction	16%	
End diastolic volume	162.04 mL	74.41 mL/m²
End systolic volume	135.92 mL	62.41 mL/m²
Stroke volume	26.12 mL	11.99 mL/m²
Cardiac output	2.98 l/min	1.37 l/min/m²
Wall mass (mean)	234.52 g	107.69 g/m²

Table 1: Left ventricle functional parameters.

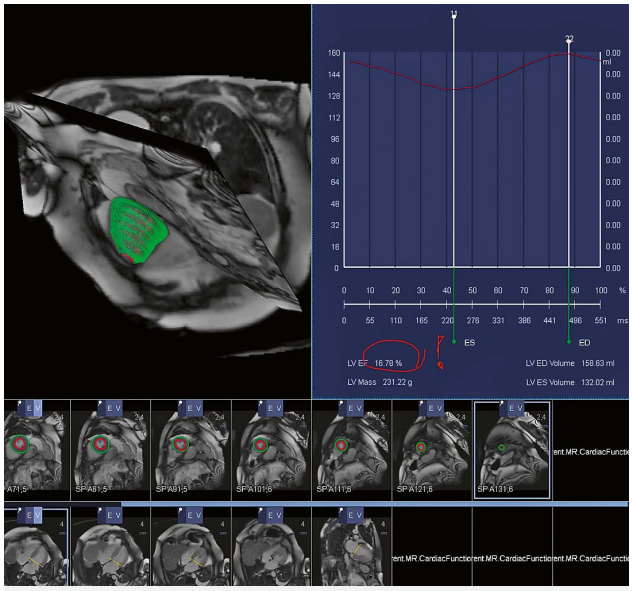

Figure 9:
Also classic indication of cardiac amyloidosis, the severe wall thickening and more than severe impact on heart function (Table 1).

Contact

Johan Dehem, M.D.
Jan Yperman Ziekenhuis
Briekestraat 12
8900 Ypres
Belgium
Phone: +32 57 35 74 00
johan.dehem@yperman.net

Your dedicated cardiovascular MRI scanner

Outcome relevant decisions – redefining patient pathways

MAGNETOM Sola Cardiovascular Edition

A dedicated MRI scanner designed to meet the demands of cardiovascular examinations

MAGNETOM Sola Cardiovascular Edition automatically adjusts to patient biovariability to overcome unwarranted variations in cardiac MRI examinations.

Gain speed, reliability and ease of use with BioMatrix Technology.

Expand toward precision medicine by improving diagnostic accuracy and facilitating individual treatment strategies.

Connect with new capabilities

Free breathing exams: Get high-quality consistent cardiac MRI scans with Compressed Sensing Cardiac Cine for functional imaging even for patients with arrhythmias or dyspnea.

Tissue characterization: MyoMaps with HeartFreeze to detect myocardial injury and get patients on the right treatment pathway fast.

Consistent results, fast: BioMatrix Sensors and the AI-powered Cardiac Dot Engine provide fast patient setup and step-by-step guidance for standardized diagnostic cardiac MRI exams.

siemens-healthineers.com/sola-cardiovascular

SIEMENS Healthineers

Impact of Compressed Sensing Cardiac Cine in a Busy Clinical Practice

Jérome Garot, M.D., Ph.D.; Gilles Auvray

Institut Cardiovasculaire Paris Sud, Massy, France

Introduction

Since its foundation in 2008, the dedicated cardiovascular MRI facility at the Institut Cardiovasculaire Paris Sud (ICPS – Cardiovascular Institute Paris-Sud), has seen around 45,000 patients. Of these, ca. 70–75% underwent a stress MR perfusion examination. In 2017 alone, over 5,400 patients were scanned, with the MR examination duration averaging 20 minutes. This tempo has been achieved thanks to thorough planning and staffing of the reception and preparation areas, scanning and reading environment as well as to careful optimization of the entire examination process, from patient reception, preparation and coaching, to accessory selection, protocol tuning and workflow management.

Cardiovascular MRI at ICPS

The stress CMR perfusion examination at ICPS consists of localization, followed by long-axis cines, stress perfusion, short-axis cines and late-enhancement. Image viewing, quality control and interpretation are done in parallel on a dedicated reading console running *syngo*.via located in the MR control room. Reporting is performed alongside reading using a software package[1] (Clinigrid software, Hemolia Inc., Paris, France) written especially for the CMR practice at ICPS which, as well as combining audio, image and text input, also serves as a database, capable of providing statistical information about patient cohort, throughput etc.

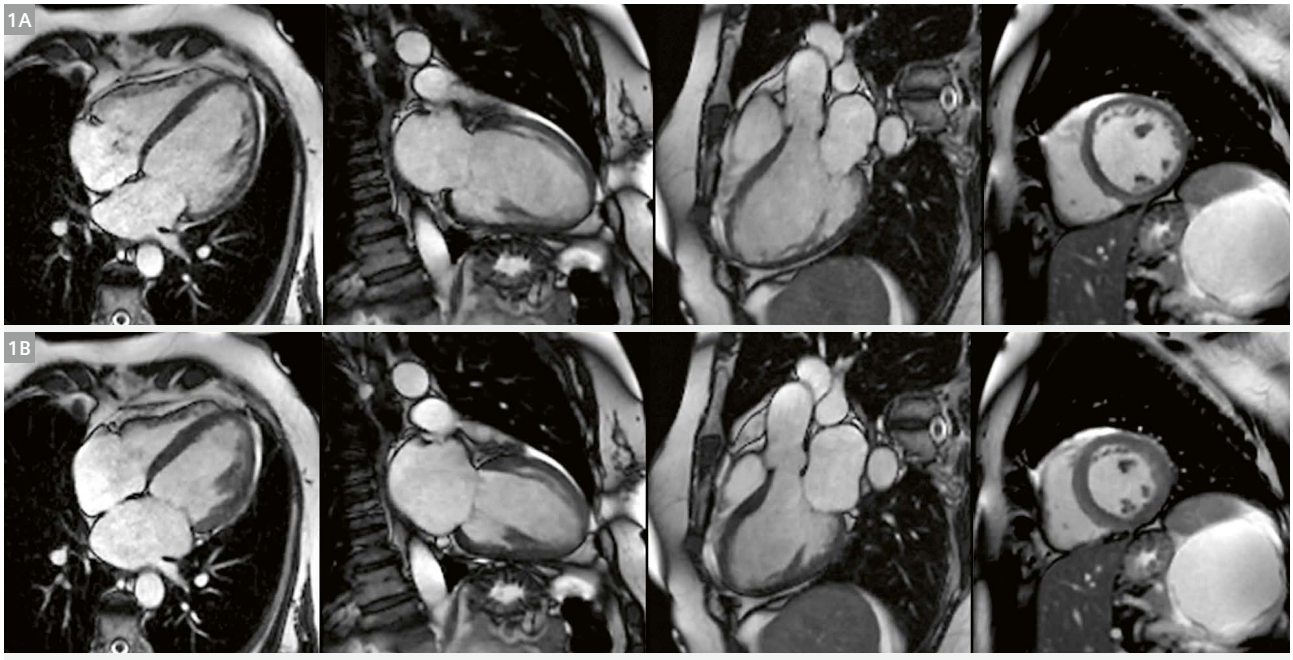

Figure 1:
Compressed Sensing Cine retrogated images obtained in diastole **(1A)** and systole **(1B)** using a two-shot imaging protocol in a patient with dilated cardiomyopathy.

[1] *The information shown herein refers to products of 3rd party manufacturers and thus are in their regulatory responsibility. Please contact the 3rd party manufacturer for further information.*

Ventricular function assessment

The assessment of left ventricular (LV) function is a core feature of every MR examination of the heart. Until September 2017, we typically performed LV function analysis using PAT-GRAPPA accelerated segmented retrogated cine TrueFISP with a PAT factor of 2. This approach is considered a gold standard in the MR imaging business, and in spite of lengthy and multiple breath-holds, it is generally well-accepted by patients and clinicians. In patients with breath-hold difficulties or arrhythmia, we resorted to prospectively triggered cine TrueFISP combined with TPAT imaging and a PAT factor of 3. The introduction of Compressed Sensing (CS) Cardiac Cine with *syngo* MR E11C-AP02 changed our examination workflow considerably. In particular, the prototype CS Cardiac Cine software[2], which allows for retrogated cine imaging across two heartbeats, has become our workhorse method for LV function assessment. Thus, following a brief investigative period including cross-comparisons with the current gold standard, we switched all our standard CMR imaging protocols to use CS Cine with retrogating. This has meant that we have been able to shorten the average stress perfusion CMR examination by 3 to 4 minutes, thereby increasing our patient throughput and improving patient comfort. As a direct consequence, we are now able to scan around 15 more patients per week.

Retrogated Compressed Sensing Cardiac Cine

The so-called "two-shot" CS Cine Retro method allows for a reduction in the total number of breath-holds required to assess left ventricular function both visually and quantitatively, as well as a shortening of the breath-hold duration itself. In general, we employ an imaging protocol with a total acceleration factor of ~6.5, an in-plane spatial resolution of 1.5 mm x 1.5 mm and a temporal resolution of the order of 40 ms; slice thickness is usually 8 mm. The acquisition duration is three heartbeats per slice, the first heartbeat being a non-imaging "dummy" heartbeat, with application of gradients and RF pulses to ensure that the magnetization has reached the steady state. Example images obtained in a patient with dilated cardiomyopathy are shown in Figure 1. Despite the high *k*-space under-sampling factor, endo- and epicardial boundaries are sharp, small trabecular structures and valves are clearly visible and, most importantly, the excellent temporal resolution ensures that wall-motion assessment and quantitative analysis are feasible. Figure 2 shows another representative example of a three-chamber cine obtained using CS Cine Retro.

In the case of patients with severe arrhythmia, or those who are unable to hold their breath, the real-time CS Cine sequence is now our alternative method of choice for the assessment of LV function. Albeit with a somewhat inferior spatial and temporal resolution compared with the two-shot CS Cine Retro method, real-time CS Cine nevertheless allows for a distinctly better image quality when evaluated against standard PAT-accelerated real-time imaging. With appropriate usage of adaptive triggering, or alternatively imaging across 1.5 cycles, it also allows for complete cycle cine imaging, necessary for accurate quantitative analysis. Figure 3 compares the two-shot CS Cine Retro method with real-time CS Cine obtained in a deaf patient in whom the conveyance of breath-hold commands was complicated. The images shown in Figure 4 illustrate the usage of the arrhythmia rejection option in CS Cine Retro to achieve clinically acceptable image quality.

The advantages of CS Cine Retro are not limited to scan time shortening alone. The method incorporates a means to trade scan time for extremely high temporal and/or spatial resolution in a single breath-hold. Thus, the so-called eight-shot protocol, which splits the acquisition over eight heartbeats, allows for the thus far inconceivable acquisition of single slice cine images with a temporal resolution of 10 ms and an in-plane spatial resolution of 1.2 mm x 1.2 mm in a total scan time of 9 heartbeats. An example of such an acquisition is shown in Figure 5.

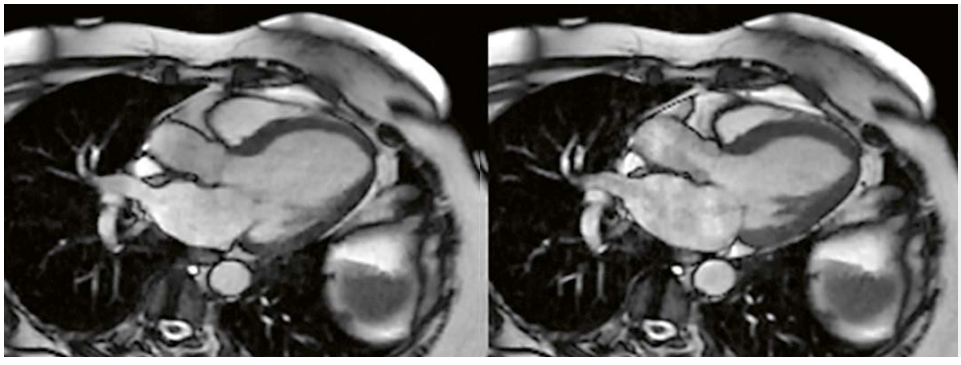

Figure 2:
Three-chamber CS Cine retrogated images obtained at end-diastole and end-systole.

[2] *WIP, the product is currently under development and is not for sale in the US and in other countries. Its future availability cannot be ensured.*

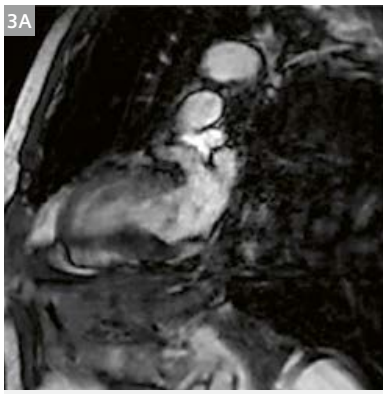

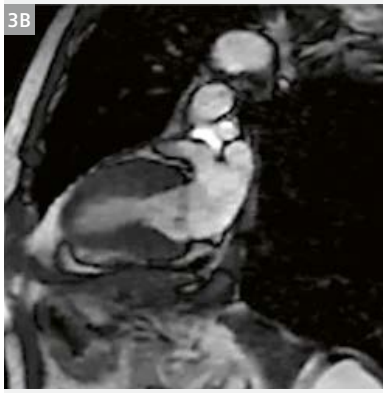

Figure 3:
Comparison of CS Cine Retro **(3A)** with CS Cine real-time **(3B)**, obtained in a deaf patient and without breath-holding.

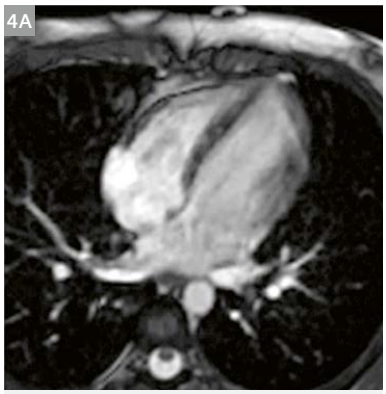

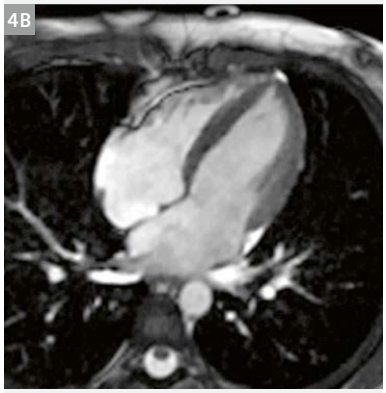

Figure 4:
CS Cine Retro images obtained without **(4A)** and with **(4B)** the arrhythmia rejection scanning option in a patient with heart rate irregularities.

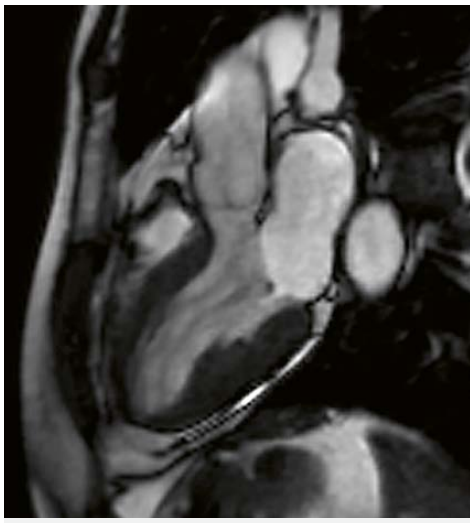

Figure 5:
Three-chamber cine obtained in a healthy volunteer using an eight-shot CS Cine Retro imaging protocol.

Conclusion

Compressed Sensing Cardiac Cine is proving to be a game-changer in the field of cardiovascular MRI. The prototype retrogated CS Cine package allows for significantly shorter scan times without loss of diagnostic information. This in turn is beneficial not only for patients, but also in further improving workflow and in expanding the usage of MRI in the assessment of cardiovascular diseases.

Acknowledgements

The authors would like to thank their colleagues at the Institut Cardiovasculaire Paris Sud, as well as their collaborators at Siemens Healthineers, in particular Carmel Hayes, Christoph Forman, Michaela Schmidt, Solenn Toupin and Matthieu Lepetit-Coiffé, for their valuable contributions to the development and testing of the prototype CS Cine Retro package in a busy clinical practice.

Contact

Professor Jérôme Garot
Head of Cardiovascular MR
Cardiovascular Institute Paris-Sud (ICPS)
6 Avenue du Noyer Lambert
91300 Massy
France
jgarot@angio-icps.com

Learn more about Compressed Sensing at
siemens.com/magnetom-world
> Hot Topics

Strength In Numbers

Like the strong magnetic fields used in an MRI scan, the Society of Cardiovascular Magnetic Resonance (SCMR) pulls together the field of CMR.

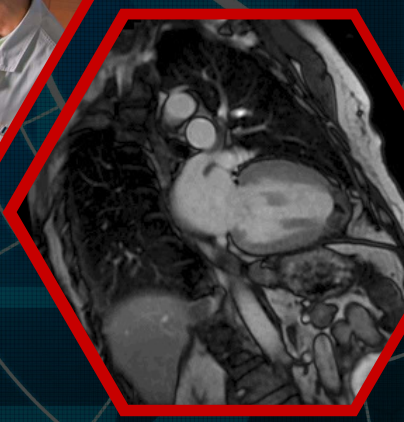

We are stronger together
Join Today

SCMR.org

Motion-corrected Whole-heart Simultaneous Cardiac MR/PET Imaging: Initial Clinical Experience

Camila Munoz[1]; Karl P. Kunze[2]; Radhouene Neji[1,2]; Stephan G. Nekolla[3]; René M. Botnar[1]; Claudia Prieto[1]

[1] School of Biomedical Engineering and Imaging Sciences, King's College London, London, United Kingdom
[2] MR Research Collaborations, Siemens Healthcare Limited, Frimley, United Kingdom
[3] Technische Universität München, Nuklearmedizinische Klinik und Poliklinik, Munich, Germany

Abstract

Image degradation due to respiratory motion remains a challenge for cardiac MR/PET imaging. Although novel approaches for MR/PET motion compensation have been recently introduced, most of these schemes usually only acquire motion information from MRI data during the PET acquisition, and diagnostic MR data afterwards. This significantly increases total examination time and may lead to misaligned images between modalities. We have recently proposed a simultaneous coronary MR angiography (CMRA) and cardiac PET acquisition and reconstruction framework[1] that enables MR visualization of the coronary anatomy and motion-corrected myocardial PET in a single efficient examination. Non-rigid respiratory motion is estimated from MR images and used to correct both the CMRA data and the simultaneously acquired PET data, resulting in intrinsically aligned motion-corrected images from both modalities. Initial validation of this approach has been performed in healthy subjects and patients with known or suspected cardiovascular disease. Results show that the motion correction approach improves quality in CMRA images, allowing for good depiction of the proximal and mid coronary arteries, while also improving PET image quality, resulting in sharper myocardial edges and allowing the observation of small anatomical features and pathologies. Overall, the proposed approach produces high quality images in both modalities, demonstrating the potential for enabling a comprehensive, non-invasive assessment of heart disease in a single and time-efficient MR/PET examination.

[1] *WIP, the product is currently under development and is not for sale in the US and in other countries. Its future availability cannot be ensured.*

Introduction

Cardiovascular disease (CVD) is the leading cause of death worldwide, accounting for 31.5% of the total number of deaths in 2015 [1]. Amongst all cardiovascular diseases, coronary artery disease (CAD) has the highest mortality rate and overall is the most common cause of death globally. The recent development of hybrid MR/PET systems has opened new possibilities for a comprehensive non-invasive assessment of cardiovascular disease, by enabling the simultaneous acquisition of complementary anatomical and functional information in a single scan session [2–4]. In particular for CAD, MR-PET systems offer great potential for simultaneous assessment of myocardial integrity (perfusion or viability) and coronary plaque activity by PET [5], and coronary lumen integrity by CMRA in a single examination. However, respiratory motion is a major source of image quality degradation in both PET and MR cardiac imaging.

Respiratory motion can result in image blurring and ghosting artifacts in MRI, and in image blurring and artifacts due to mismatches between attenuation maps and emission maps in PET. Conventionally, the effect of respiratory motion in both PET and CMRA imaging has been mitigated by using techniques that sort the acquired data into near motion-free frames representing different positions within the respiratory cycle. These techniques, widely known as gating techniques, can be used to acquire data (or accept data for image reconstruction) only when the respiratory signal is within a predefined phase of the breathing cycle, typically end-expiration, rejecting all other data being acquired. The main drawback of gating approaches is that they lead to long acquisition times to acquire enough data, i.e. with high enough signal-to-noise ratio (SNR) for PET

and enough samples for a desired spatial resolution and coverage for MRI. Furthermore, as respiratory patterns vary greatly among subjects, gating usually results in unpredictable scan times, negatively impacting patient throughput.

Alternatively, the problem of respiratory motion can be addressed by obtaining information about the motion from the acquired data itself and then using it to produce motion-compensated images with improved image quality in a shorter acquisition time. Although several motion compensation approaches have been developed over the last decades separately for both PET and MR imaging, the introduction of hybrid MR/PET scanners has allowed the development of novel techniques to alleviate the problem of motion simultaneously for both modalities.

In cardiac MR/PET imaging, most of the research efforts about motion compensation have focused on improving PET image quality by acquiring MR images with high spatial resolution and superior soft-tissue contrast simultaneously with PET, so that motion information obtained from such MR images can be used to correct the PET data [6, 7]. Although this approach has been shown to positively impact PET image quality and quantification, in general the simultaneously acquired MR data is being used only for motion estimation, limiting their use for diagnosis purposes.

Therefore, whereas clinical application of simultaneous cardiac MR/PET imaging for the diagnosis of CAD and other cardiovascular conditions would benefit from the complementarity between the functional and

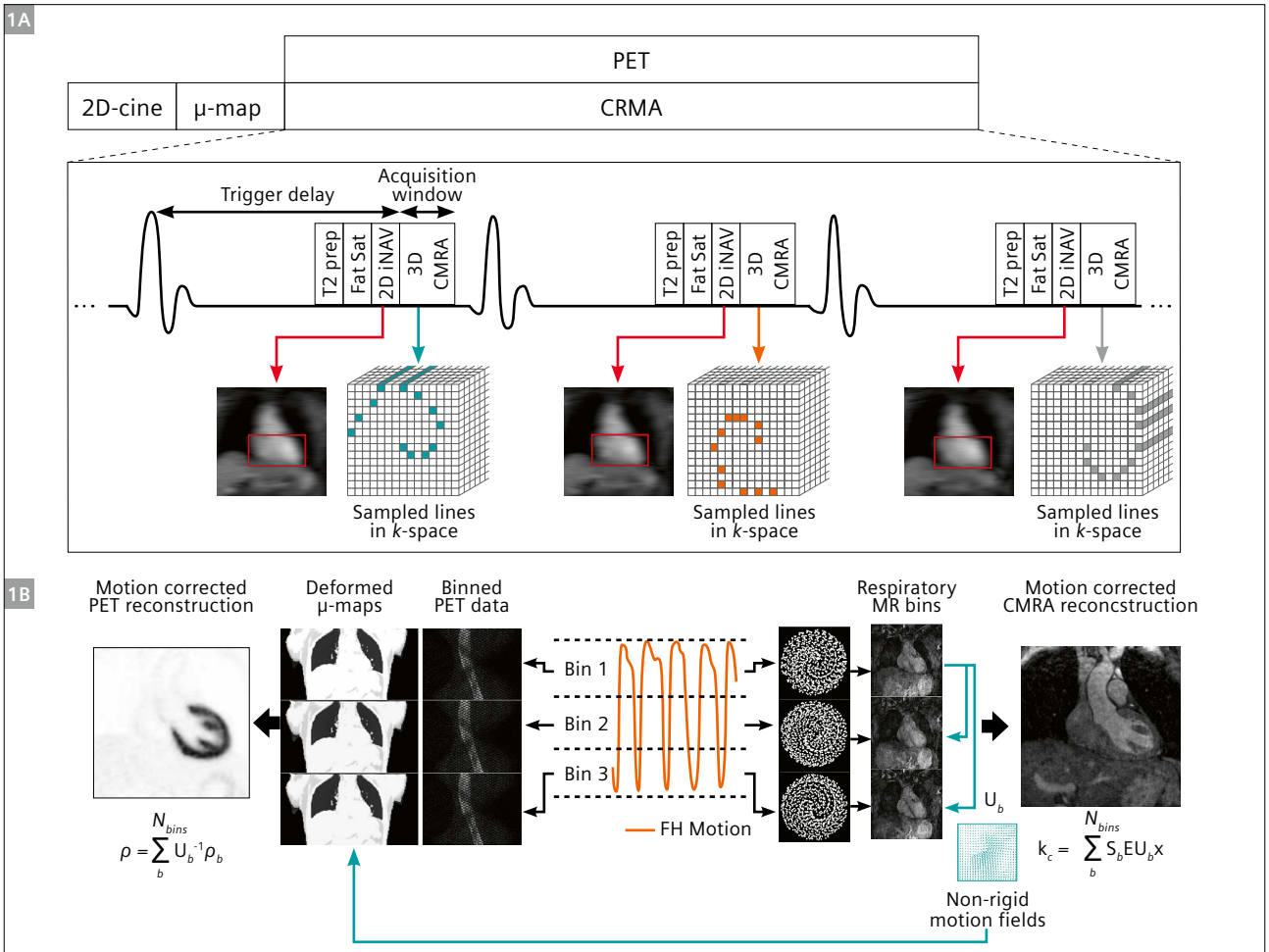

Figure 1:
PET-CMRA acquisition and reconstruction method. **(1A)** PET-CMRA acquisition protocol, an image-navigator (2D iNAV) is acquired at each heartbeat before the CMRA acquisition for estimating respiratory motion. T2 preparation (T2 prep) and fat saturation (fatsat) pulses are used in order to improve contrast between blood and surrounding tissue. Before the PET-CMRA acquisition, a 2D cine image is acquired to define the trigger delay and acquisition window within the cardiac cycle for 3D CMRA, and a µ-map is acquired for attenuation correction of the PET data. **(1B)** Foot-head (FH) motion estimated from the 2D iNAVs is used to bin the PET and CMRA data in a number of respiratory bins. Non-rigid deformation fields (in teal) are estimated from MR images reconstructed at each respiratory position and used to transform the attenuation maps to each respiratory position, and in the proposed motion compensated PET and CMRA image reconstruction. *Figure adapted from [8].*

morphological diagnostic information provided by both modalities, in practice, state-of-the-art approaches acquire diagnostic information from each modality sequentially, leading to long acquisition times and misaligned diagnostic PET and MR images.

We have recently proposed a novel framework[1] for simultaneous non-rigid respiratory motion compensated cardiac MR/PET imaging, allowing for visualization of the coronary arteries by CMRA and assessment of myocardial integrity by PET from a single examination [8]. This framework enables respiratory motion tracking by including a 2D image navigator (iNAV) in the MR acquisition sequence, which allows for estimating the position of the heart within the respiratory cycle at each heartbeat. Then, by combining a beat-to-beat 2D translational motion correction with a bin-to-bin 3D non-rigid motion correction approach for CMRA, the MR-derived non-rigid motion information can be used to correct for both the CMRA and the simultaneously acquired PET data to the same respiratory position.

This approach is highly efficient since nearly all acquired data is used for image reconstruction (100% scan efficiency), resulting in predictable and shorter scan time compared to conventional gated acquisitions. Additionally, the framework enables the acquisition of diagnostic MR and PET images simultaneously, significantly reducing the total exam time compared to techniques that perform diagnostic MR acquisitions after the PET acquisition, without sacrificing image quality.

Here we present a brief summary of our technique, including some results from our initial clinical experience in patients with known or suspected cardiovascular disease [9], which demonstrate the benefits of the proposed motion-correction scheme for simultaneous CMRA and myocardial characterization by PET in different clinical contexts.

Methods

The whole-heart PET-CMRA acquisition consists of a free-breathing ECG-triggered CMRA sequence simultaneously acquired with list-mode cardiac PET data, as shown in Figure 1A. CMRA data is acquired using a 3D spoiled gradient echo sequence following a fully sampled golden-step Cartesian trajectory with spiral profile ordering, so that one spiral interleaf is acquired at each heartbeat [10]. A 2D iNAV [11] is acquired at the beginning of each spiral interleaf by spatially encoding low flip angle *k*-space lines, and fat saturation and T2 preparation [12] pulses are performed immediately prior to CMRA data acquisition to improve the contrast between arterial blood and the surrounding myocardium and epicardial fat.

As part of the cardiac PET-CMRA acquisition protocol, a standard Dixon-based attenuation map (μ-map hereafter) is acquired in breath-hold at end-expiration for MR-based attenuation correction of the PET data, with missing tissue due to the limited field of view of the MR (as compared to PET) estimated using the MLAA (maximum likelihood reconstruction of attenuation and activity) approach [13]. In order to define the trigger delay and length of the acquisition window of the 3D CMRA, a conventional 2D cine image is acquired before the PET-CMRA acquisition.

Motion-compensated PET-CMRA image reconstruction is performed in four steps, which are summarized in Figure 1B. In the first step, foot-head (FH) and right-left (RL) translational respiratory motion is estimated from the 2D iNAVs by using rigid image registration of a template covering the apex of the heart (as shown in Figure 1A, in red rectangles). In the second step, FH motion is used to bin the acquired PET and CMRA data in a number of respiratory windows or bins, ranging from end-expiration to end-inspiration, each containing approximately the same amount of data. In a third step, 3D MR images are reconstructed at each respiratory position using iterative SENSE with a soft-binning approach [14], and bin-to-bin respiratory deformation fields are estimated by non-rigid image registration, using the end-expiration bin as reference. Finally, the non-rigid deformation fields are used in a generalized matrix description formulation for motion-compensated CMRA reconstruction [15]. Moreover, the non-rigid motion fields are used to move the attenuation maps to each respiratory position and perform a motion-compensated PET reconstruction. Therefore, at the end of the image reconstruction process, co-registered respiratory motion-corrected CMRA and cardiac PET images are obtained.

Study design

The PET-CMRA acquisition protocol was implemented as a prototype on a 3T MR/PET scanner (Biograph mMR, Siemens Healthcare, Erlangen, Germany), and two preliminary studies were performed. In the first study, ten healthy subjects (age 30.0 ± 3.7 years, 4 males) were recruited for an MR-only examination with the proposed method, with the aim of validating the motion-corrected CMRA approach. For this purpose, an additional reference scan with 1D diaphragmatic navigator gating and tracking was performed for each subject, so the proposed motion-corrected CMRA could be validated against the current MR clinical standard.

[1] *WIP, the product is currently under development and is not for sale in the US and in other countries. Its future availability cannot be ensured.*

Twenty patients referred to our institutions for a cardiac MR/PET examination were recruited for the second part of the study, whose aim was to evaluate the impact of the proposed motion-corrected PET-CMRA framework in a relevant patient population. 14 of the patients presented symptomatic CAD (angina or angina equivalent, excluding acute ST-elevation myocardial infarction patients) with chronic total occlusion (CTO) of a relevant coronary artery, and were referred for a hybrid ^{18}F-FDG MR/PET examination in order to improve risk stratification before elective percutaneous coronary intervention of the CTO. Four patients were referred for a hybrid ^{18}F-FDG MR/PET examination for differential diagnosis of cardiac sarcoidosis, and the remaining two were referred for a joint ^{13}N-Ammonia MR/PET myocardial perfusion examination. Relevant patient characteristics include: age 60.6 ± 12.4 years, 15 males. Written informed consent with respect to participation was obtained from all patients and healthy subjects, and the study was performed in concordance with the Declaration of Helsinki and approved by the institutional ethics committee.

For the CMRA acquisition, relevant imaging parameters included: coronal orientation, resolution = 1 × 1 × 2 mm^3 (interpolated to 1 mm^3 isotropic resolution during MR image reconstruction), field of view = 304 × 304 × 80–112 mm^3 covering the whole heart, TR/TE = 3.72/1.70 ms, flip angle = 15°. A subject-specific trigger delay was defined targeting mid-diastole, and an acquisition window of 89 to 119 ms (corresponding to 24 to 32 readouts per spiral interleaf)

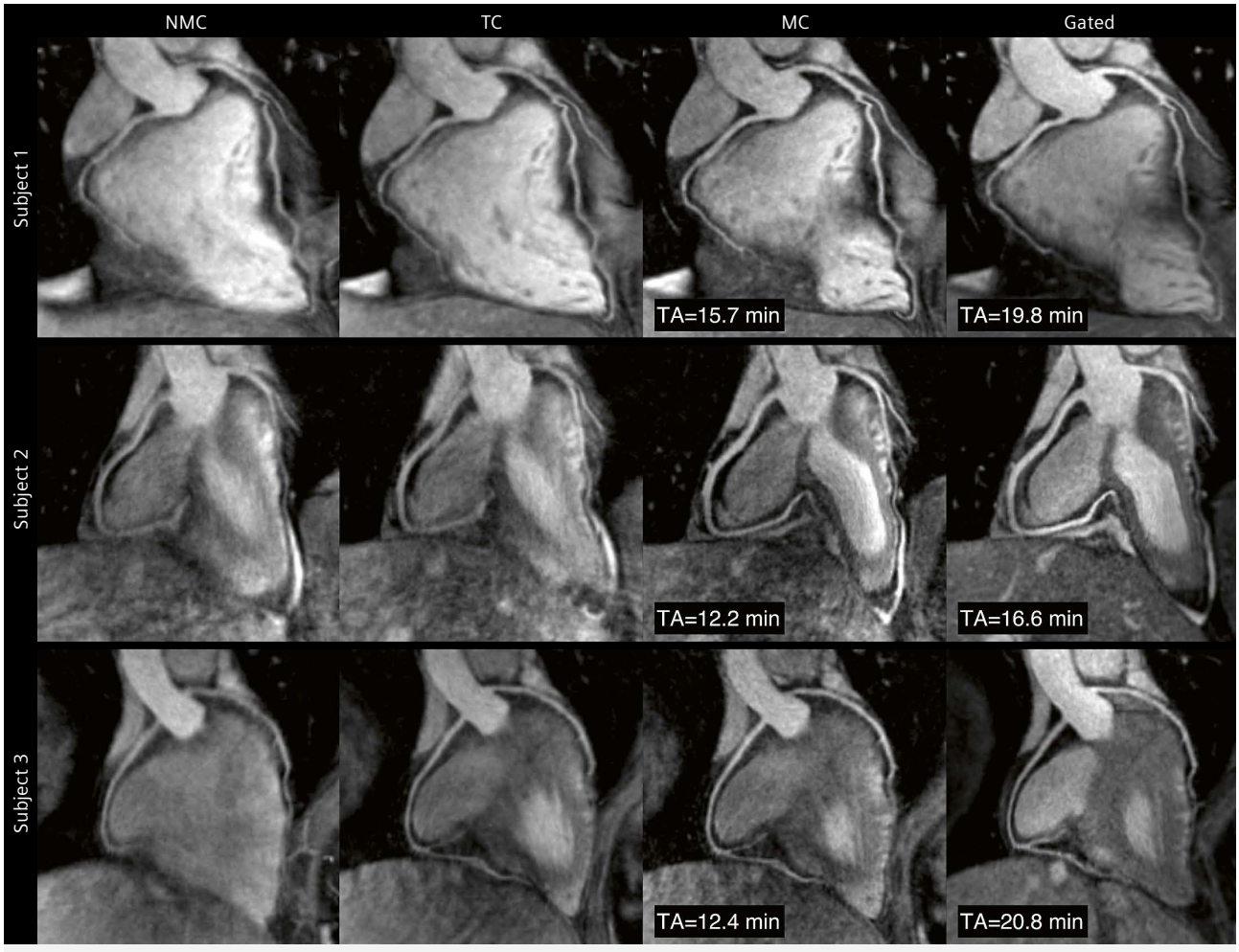

Figure 2:
Multi-planar reformatting of CMRA images for three representative healthy subjects (rows) showing non-motion-corrected (NMC), translational motion-corrected (TC), non-rigid motion-corrected (MC) and diaphragmatic gated-and-tracked (Gated) images. The scan time for the MC (same for NMC and TC) and Gated approaches is indicated for each subject. Improvements in the visualization of the distal part of the RCA and LAD can be observed when applying TC and MC in comparison to NMC. Furthermore, the MC approach produces images of quality comparable to the Gated images, but in a shorter and predictable scan time.

was selected depending on the length of the mid-diastolic quiescent period of the cardiac cycle. The 2D iNAVs were acquired using the following imaging parameters: same field of view as the 3D CMRA acquisition, flip-angle = 3°, 14 readouts acquired with a high-low Cartesian trajectory, corresponding to a 1 × 21.7 mm^2 acquired resolution interpolated to 1 mm^2 before respiratory motion tracking. For PET attenuation correction, μ-maps were acquired for each of the twenty patients during a 19 s breath-hold at end-expiration using the Siemens' provided 2-point Dixon protocol (with acquisition parameters: coronal orientation, resolution = 2.6 × 2.6 × 3.1 mm^3, field of view = 328 × 500 × 399 mm^3, TR/TE1/TE2 = 3.60/1.23/2.46 ms).

CMRA and PET datasets were reconstructed offline with the described motion correction scheme (MC) and without motion correction (NMC) for comparison purposes. MR image reconstruction was performed in MATLAB (Mathworks, Natick, Massachusetts, USA) using custom developed software. PET image reconstruction was performed offline using RTA motion correction [16]. For this, the μ-map acquired at end-expiration was registered to each respiratory position in MATLAB using the deformation fields estimated from MR images. Each respiratory bin was independently reconstructed offline with Siemens Healthineers e7 Tools using the OSEM algorithm [17], with 3 iterations and 21 subsets, point spread function modelling, voxel size = 2.03 × 2.08 × 2.08 mm^3, matrix size = 127 × 344 × 344. Finally, images reconstructed at each respiratory position were combined in MATLAB to produce a motion-corrected PET image.

Results

Scans were successfully completed in all subjects. The average acquisition time for the proposed PET-CMRA framework was 12.3 ± 1.7 minutes for the healthy subjects and 11.9 ± 2.8 minutes for patients. Multi-planar reformatting of the 3D CMRA images for simultaneous visualization of the right coronary artery (RCA) and left anterior descending artery (LAD) are shown in Figure 2 for three representative healthy subjects. Reference 1D diaphragmatic gating and tracking (Gated) images, obtained with comparable acquisition parameters but with 2-fold acceleration, are displayed next to the motion corrected (MC) images for comparison purposes. Improvements in the visualization of the distal part of the LAD and RCA can be observed for all subjects when applying translational motion correction only (TC) in comparison with the uncorrected images (NMC), and further improvements can be observed with MC for the visualization of the vessels. Similar image quality can be seen for MC and Gated images for the depiction of both the LAD and RCA; however, the acquisition time for the motion-corrected approach was significantly shorter.

Similar results in terms of improvements in image quality were obtained for cardiac patients, despite more irregular breathing patterns. Reformatted CMRA images showing non-stented RCA and LAD for four of the cardiac patients are shown in Figure 3. As can be observed, MC enables the depiction of the proximal segment of all the vessels, even in cases where severe respiratory motion prevented the visualization of both the left and right coronary arteries in the NMC image, as observed for Patient 1 (green arrows). Furthermore, improvements in the depiction of the distal segment of the vessels were observed (blue arrows). Figure 4 shows example coronal slices of the reconstructed cardiac PET images for four representative patients. MC increased the sharpness of large structures such as the liver or the left ventricle myocardium, and enhanced the depiction of smaller structures such as the papillary muscles (blue arrows).

For the patients with CAD, the clinical MR/PET protocol included a conventional multi-slice 2D phase-sensitive inversion recovery (PSIR) LGE acquisition for assessment of myocardial viability (1.4–2.2 mm in-plane resolution, 8 mm slice thickness), and patients underwent interventional X-ray angiography the day after the MR/PET examination for elective CTO revascularization. Therefore, for this subset of patients, NMC and MC PET images were reoriented in short axis to visually compare them with the LGE images acquired in the same scan session, while MC CMRA images were reformatted following the anatomy observed in the X-ray angiography.

A visual comparison between the reformatted MC CMRA and the corresponding invasive X-ray angiogram is shown in Figure 5 for two of the CAD patients. Adequate spatial resolution and contrast in CMRA images allowed for a depiction of the proximal arteries comparable to the X-ray angiogram for both cases. In Patient 6, a stenosis observed in the mid segment of the RCA in CMRA was confirmed in the angiogram (Fig. 5, red arrows), while in Patient 7 an aneurysm in the proximal RCA was seen in both modalities (Fig. 5, green arrows).

Figure 6 shows a short axis view of the ^{18}F-FDG PET images both for NMC and MC reconstructions and corresponding slice of the 2D LGE scan for two CAD patients. It can be observed that MC PET images have an improved correspondence to the anatomy as observed in the LGE images and reduced noise compared to NMC images. In particular, improvements in delineation of viability defects are apparent: for Patient 6, the transmural viability defect observed in the infero-lateral wall was better depicted after motion correction (Fig. 6, blue arrows), while in Patient 8, motion correction allowed for the

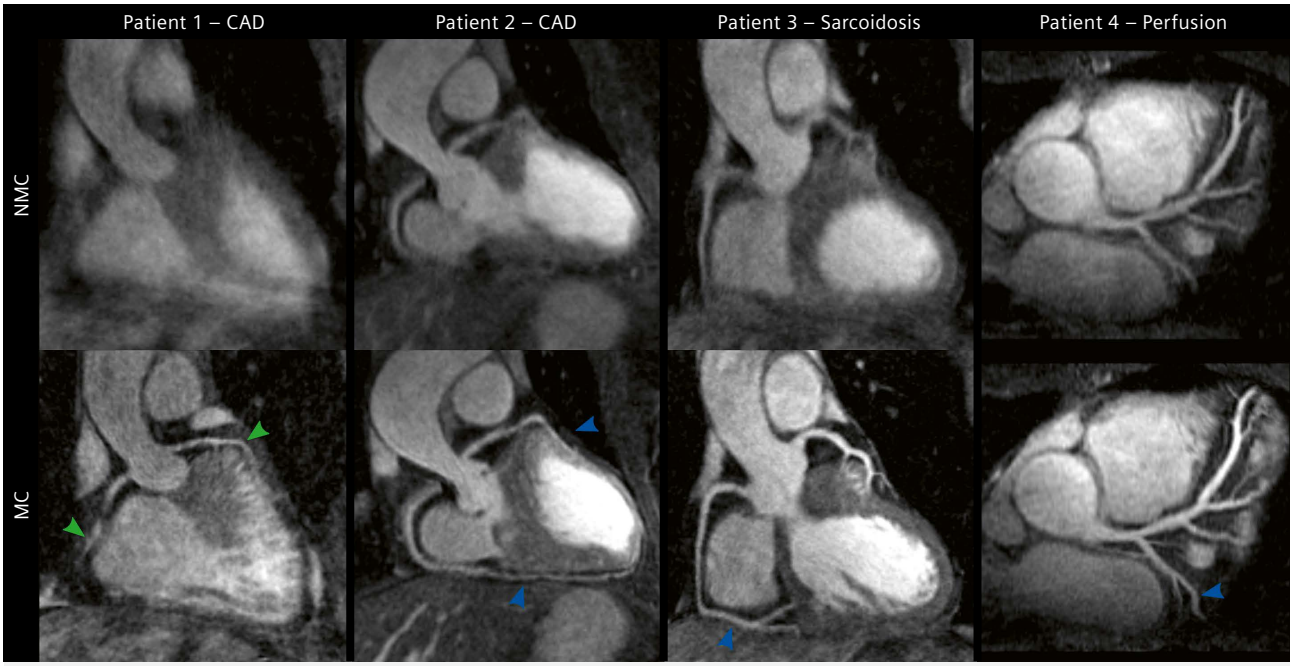

Figure 3:
Multi-planar reformatting of CMRA images for four representative patients referred for CAD, sarcoidosis and myocardial perfusion examinations (columns) showing uncorrected (NMC) and motion-corrected (MC) CMRA images. Improvements in the visualization of the vessels are observed when applying MC for all cases, both in the proximal (green arrows) and in the distal segments of the arteries (blue arrows).

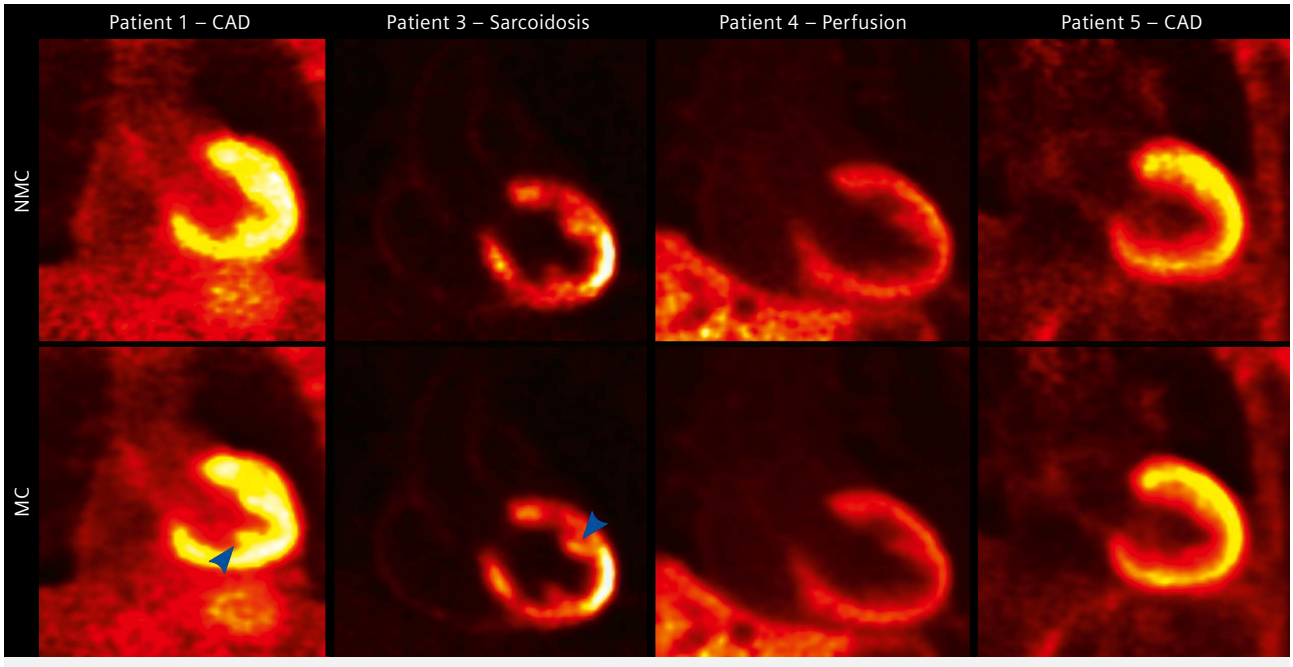

Figure 4:
Coronal slice for four representative patients (columns) referred for CAD, sarcoidosis and myocardial perfusion examinations showing uncorrected (NMC) and motion-corrected (MC) viability ^{18}F-FDG (Patients 1, 3, 5) and perfusion ^{13}N-ammonia (Patient 4) PET images. Improvements in image quality can be observed when applying MC compared to NMC, particularly for small structures (blue arrows).

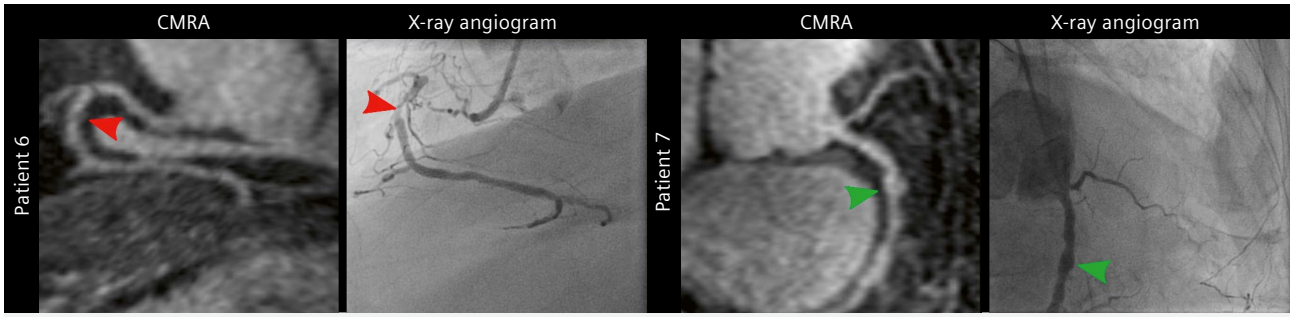

Figure 5:
Reformatted CMRA and corresponding X-ray angiogram images for two CAD patients. In Patient 6, a stenosis in the mid segment of the right coronary artery (RCA) can be observed in both modalities (red arrows), while for Patient 7 an aneurysm can be observed in the proximal segment of the RCA (green arrows).
Figure adapted from [9].

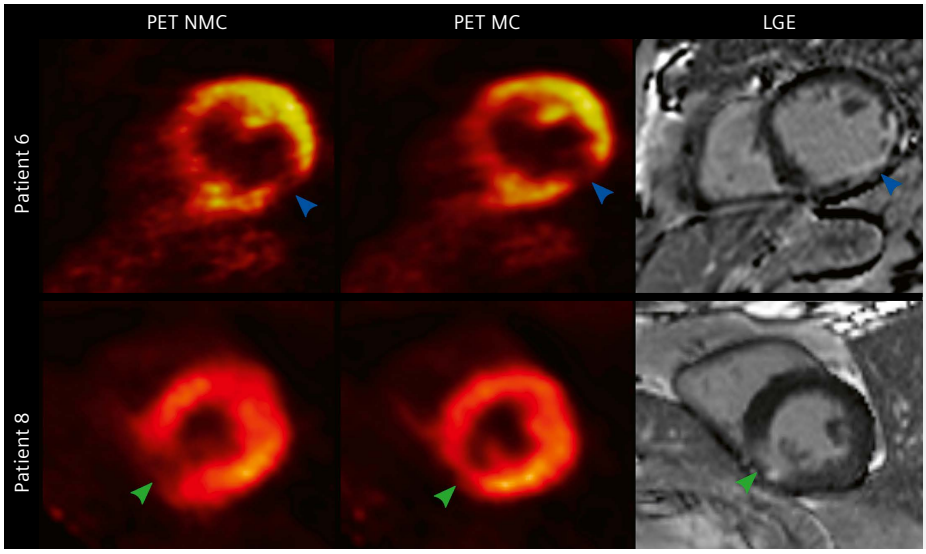

Figure 6:
Short axis view for two CAD patients (rows) showing un-corrected (NMC) and motion-corrected (MC) viability ^{18}F-FDG PET images as well as corrsponding 2D LGE images. MC improves the correspondence of the PET images to the anatomy as observed in the LGE images, particularly in the delineation of viability defects (green and blue arrows).
Figure adapted from [9].

identification of viable myocardium in a defect that appeared misleadingly as transmural in the NMC image (Fig. 6, green arrows).

Finally, Figure 7 shows an example fused PET-CMRA dataset before and after motion correction. The framework produces co-registered diagnostic PET and CMRA images, improving the correspondence between modalities compared to uncorrected images.

Summary

In this article we have described a novel approach for respiratory motion-corrected cardiac MR/PET for the simultaneous visualization of coronary anatomy by CMRA and myocardial integrity (viability or perfusion) by PET. In contrast to many other MR-based motion correction approaches for cardiac PET data, that utilize MR images mainly for improving PET image quality, this approach produces diagnostic images with both modalities, potentially reducing total examination time. Furthermore, the proposed PET-CMRA acquisition and reconstruction scheme has a short and predictable scan time of approximately 12 minutes, which makes it suitable for clinical practice.

We performed a first clinical validation of the proposed approach, testing the benefit of the motion-correction scheme in a cohort of 20 patients with known or suspected cardiovascular disease. The reported results show that motion correction consistently improves image quality compared to the uncorrected images for both imaging modalities. A good agreement between coronary anatomy depicted by motion-corrected CMRA and X-ray angiography was observed in patients with coronary heart disease. In addition, motion-corrected ^{18}F-FDG images were in good agreement with LGE-MRI, showing more accurate depiction of both transmural and non-transmural viability defects than uncorrected images.

Results obtained from the cohort of patients with coronary artery disease and from additional preliminary tests in patients with a variety of cardiac conditions have

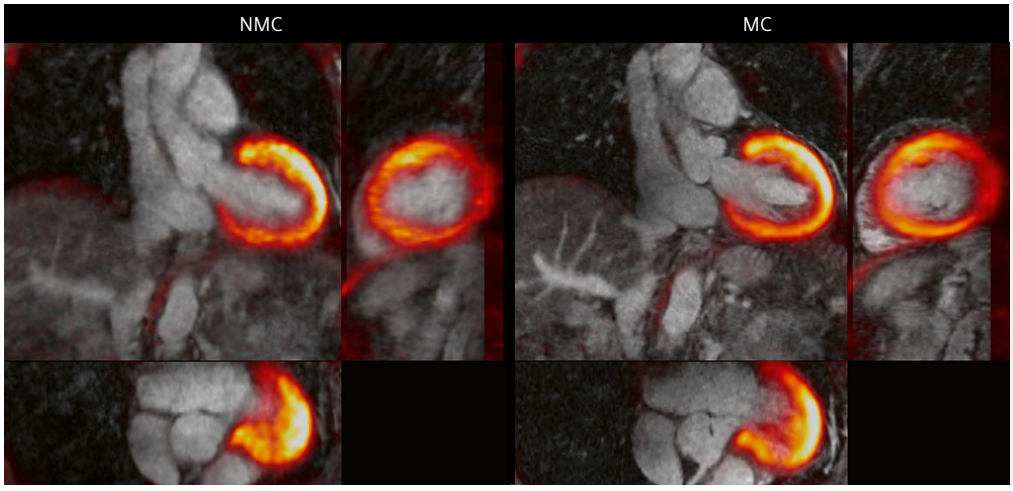

Figure 7:
Example of fused PET-CMRA images showing uncorrected (NMC) and motion-corrected (MC) images for a representative patient. The motion correction framework produces co-registered diagnostic PET and MR images for which an improved correspondence between both modalities can be observed. *Figure adapted from [9].*

shown that the PET-CMRA framework approach is robust and can be applied in combination with different PET radiotracers. Furthermore, the results suggest that the PET-CMRA framework allows the acquisition of diagnostic images with both modalities in a time-efficient and overall short examination, showing promise for its integration into clinical practice. Future work includes acceleration of the CMRA acquisition using variable density trajectories that allow undersampled acquisitions, such as the ones described in [18], in order to increase spatial resolution and volumetric coverage without increasing acquisition time.

References

1 Collaborators GBD (GBD) 2013 M and C of D. Global, regional, and national age–sex specific all-cause and cause-specific mortality for 240 causes of death, 1990–2013: a systematic analysis for the Global Burden of Disease Study 2013. Lancet 2014;385:117–71.
2 Nensa F, Bamberg F, Rischpler C, et al. Hybrid cardiac imaging using PET/MRI: a joint position statement by the European Society of Cardiovascular Radiology (ESCR) and the European Association of Nuclear Medicine (EANM). Eur Radiol 2018;2:14.
3 Robson PM, Dey D, Newby DE, et al. MR/PET Imaging of the Cardiovascular System. JACC Cardiovasc Imaging 2017;10:1165–1179.
4 Nazir MS, Ismail TF, Reyes E, Chiribiri A, Kaufmann PA, Plein S. Hybrid positron emission tomography–magnetic resonance of the heart: current state of the art and future applications. Eur Hear J – Cardiovasc Imaging 2018;19:962–974.
5 Robson PM, Dweck MR, Trivieri MG, et al. Coronary Artery PET/MR Imaging: Feasibility, Limitations, and Solutions. JACC Cardiovasc Imaging 2017;10:1103–1112.
6 Munoz C, Kolbitsch C, Reader AJ, Marsden P, Schaeffter T, Prieto C. MR-Based Cardiac and Respiratory Motion-Compensation Techniques for MR-PET Imaging. PET Clin 2016;11:179–191.
7 Catana C. Motion Correction Options in PET/MRI. Semin Nucl Med 2015;45:212–223.
8 Munoz C, Neji R, Cruz G, et al. Motion-corrected simultaneous cardiac positron emission tomography and coronary MR angiography with high acquisition efficiency. Magn Reson Med 2017;79:339–350.
9 Munoz C, Kunze KP, Neji R, et al. Motion-corrected whole-heart MR-PET for the simultaneous visualisation of coronary artery integrity and myocardial viability : an initial clinical validation. Eur J Nucl Med Mol Imaging 2018:1–12.
10 Prieto C, Doneva M, Usman M, et al. Highly efficient respiratory motion compensated free-breathing coronary MRA using golden-step Cartesian acquisition. J Magn Reson Imaging 2015;41:738–746.
11 Henningsson M, Koken P, Stehning C, Razavi R, Prieto C, Botnar RM. Whole-heart coronary MR angiography with 2D self-navigated image reconstruction. Magn Reson Med 2012;67:437–445.
12 Botnar RM, Stuber M, Danias PG, Kissinger K V., Manning WJ. Improved coronary artery definition with T2-weighted, free-breathing, three-dimensional coronary MRA. Circulation 1999;99:3139–3148.
13 Nuyts J, Bal G, Kehren F, Fenchel M, Michel C, Watson C. Completion of a truncated attenuation image from the attenuated PET emission data. IEEE Trans Med Imaging 2013;32:237–246.
14 Cruz G, Atkinson D, Henningsson M, Botnar RM, Prieto C. Highly efficient nonrigid motion-corrected 3D whole-heart coronary vessel wall imaging. Magn Reson Med 2017;77:1894–1908.
15 Batchelor PG, Atkinson D, Irarrazaval P, Hill DLG, Hajnal J, Larkman D. Matrix description of general motion correction applied to multishot images. Magn Reson Med 2005;54:1273–1280.
16 Picard Y, Thompson CJ. Motion correction of PET images using multiple acquisition frames. IEEE Trans Med Imaging 1997;16:137–44.
17 Hudson HM, Larkin RS. Accelerated image reconstruction using ordered subsets of projection data. IEEE Trans Med Imaging 1994;13:601–9.
18 Bustin A, Ginami G, Cruz G, et al. Five-minute whole-heart coronary MRA with sub-millimeter isotropic resolution, 100% respiratory scan efficiency, and 3D-PROST reconstruction. Magn Reson Med 2018 doi: 10.1002/mrm.27354.

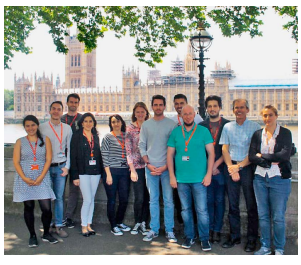

Contact

Camila Munoz
School of Biomedical Engineering and Imaging Sciences
4th Floor, Lambeth Wing
St Thomas' Hospital
London, SE1 7EH
United Kingdom
camila.munoz@kcl.ac.uk

HIGHLIGHTS OF PRESCRIBING INFORMATION

These highlights do not include all the information needed to use Fludeoxyglucose F 18 Injection safely and effectively. See full prescribing information for Fludeoxyglucose F 18 Injection. Fludeoxyglucose F 18 Injection, USP For intravenous use Initial U.S. Approval: 2005

RECENT MAJOR CHANGES

Warnings and Precautions (5.1, 5.2)	7/2010
Adverse Reactions (6)	7/2010

INDICATIONS AND USAGE

Fludeoxyglucose F18 Injection is indicated for positron emission tomography (PET) imaging in the following settings:

- Oncology: For assessment of abnormal glucose metabolism to assist in the evaluation of malignancy in patients with known or suspected abnormalities found by other testing modalities, or in patients with an existing diagnosis of cancer.
- Cardiology: For the identification of left ventricular myocardium with residual glucose metabolism and reversible loss of systolic function in patients with coronary artery disease and left ventricular dysfunction, when used together with myocardial perfusion imaging.
- Neurology: For the identification of regions of abnormal glucose metabolism associated with foci of epileptic seizures (1).

DOSAGE AND ADMINISTRATION

Fludeoxyglucose F 18 Injection emits radiation. Use procedures to minimize radiation exposure. Screen for blood glucose abnormalities.

- In the oncology and neurology settings, instruct patients to fast for 4 to 6 hours prior to the drug's injection. Consider medical therapy and laboratory testing to assure at least two days of normoglycemia prior to the drug's administration (5.2).
- In the cardiology setting, administration of glucose-containing food or liquids (e.g., 50 to 75 grams) prior to the drug's injection facilitates localization of cardiac ischemia (2.3).

Aseptically withdraw Fludeoxyglucose F 18 Injection from its container and administer by intravenous injection (2).

The recommended dose:

- for adults is 5 to 10 mCi (185 to 370 MBq), in all indicated clinical settings (2.1).
- for pediatric patients is 2.6 mCi in the neurology setting (2.2).

Initiate imaging within 40 minutes following drug injection; acquire static emission images 30 to 100 minutes from time of injection (2).

DOSAGE FORMS AND STRENGTHS

Multi-dose 30mL and 50mL glass vial containing 0.74 to 7.40 GBq/mL (20 to 200 mCi/mL) Fludeoxyglucose F 18 Injection and 4.5mg of sodium chloride with 0.1 to 0.5% w/w ethanol as a stabilizer (approximately 15 to 50 mL volume) for intravenous administration (3).

CONTRAINDICATIONS

None

WARNINGS AND PRECAUTIONS

- Radiation risks: use smallest dose necessary for imaging (5.1).
- Blood glucose adnormalities: may cause suboptimal imaging (5.2).

ADVERSE REACTIONS

Hypersensitivity reactions have occurred; have emergency resuscitation equipment and personnel immediately available (6).

To report SUSPECTED ADVERSE REACTIONS, contact PETNET Solutions, Inc. at 877-473-8638 or FDA at 1-800-FDA-1088 or www.fda.gov/medwatch.

USE IN SPECIFIC POPULATIONS

Pregnancy Category C: No human or animal data. Consider alternative diagnostics; use only if clearly needed (8.1).

- Nursing mothers: Use alternatives to breast feeding (e.g., stored breast milk or infant formula) for at least 10 half-lives of radioactive decay, if Fludeoxyglucose F 18 Injection is administered to a woman who is breast-feeding (8.3).
- Pediatric Use: Safety and effectiveness in pediatric patients have not been established in the oncology and cardiology settings (8.4).

See 17 for PATIENT COUNSELING INFORMATION

Revised: 1/2011

FULL PRESCRIBING INFORMATION: CONTENTS*

1 INDICATIONS AND USAGE
- 1.1 Oncology
- 1.2 Cardiology
- 1.3 Neurology

2 DOSAGE AND ADMINISTRATION
- 2.1 Recommended Dose for Adults
- 2.2 Recommended Dose for Pediatric Patients
- 2.3 Patient Preparation
- 2.4 Radiation Dosimetry
- 2.5 Radiation Safety – Drug Handling
- 2.6 Drug Preparation and Administration
- 2.7 Imaging Guidelines

3 DOSAGE FORMS AND STRENGTHS

4 CONTRAINDICATIONS

5 WARNINGS AND PRECAUTIONS
- 5.1 Radiation Risks
- 5.2 Blood Glucose Abnormalities

6 ADVERSE REACTIONS

7 DRUG INTERACTIONS

8 USE IN SPECIFIC POPULATIONS
- 8.1 Pregnancy
- 8.3 Nursing Mothers
- 8.4 Pediatric Use

11 DESCRIPTION
- 11.1 Chemical Characteristics
- 11.2 Physical Characteristics

12 CLINICAL PHARMACOLOGY
- 12.1 Mechanism of Action
- 12.2 Pharmacodynamics
- 12.3 Pharmacokinetics

13 NONCLINICAL TOXICOLOGY
- 13.1 Carcinogenesis, Muta-genesis, Impairment of Fertility

14 CLINICAL STUDIES
- 14.1 Oncology
- 14.2 Cardiology
- 14.3 Neurology

15 REFERENCES

16 HOW SUPPLIED/STORAGE AND DRUG HANDLING

17 PATIENT COUNSELING INFORMATION

* Sections or subsections omitted from the full prescribing information are not listed.

FULL PRESCRIBING INFORMATION

1 INDICATIONS AND USAGE

Fludeoxyglucose F 18 Injection is indicated for positron emission tomography (PET) imaging in the following settings:

1.1 Oncology

For assessment of abnormal glucose metabolism to assist in the evaluation of malignancy in patients with known or suspected abnormalities found by other testing modalities, or in patients with an existing diagnosis of cancer.

1.2 Cardiology

For the identification of left ventricular myocardium with residual glucose metabolism and reversible loss of systolic function in patients with coronary artery disease and left ventricular dysfunction, when used together with myocardial perfusion imaging.

1.3 Neurology

For the identification of regions of abnormal glucose metabolism associated with foci of epileptic seizures.

2 DOSAGE AND ADMINISTRATION

Fludeoxyglucose F 18 Injection emits radiation. Use procedures to minimize radiation exposure. Calculate the final dose from the end of synthesis (EOS) time using proper radioactive decay factors. Assay the final dose in a properly calibrated dose calibrator before administration to the patient [see Description (11.2)].

2.1 Recommended Dose for Adults

Within the oncology, cardiology and neurology settings, the recommended dose for adults is 5 to 10 mCi (185 to 370 MBq) as an intravenous injection.

2.2 Recommended Dose for Pediatric Patients

Within the neurology setting, the recommended dose for pediatric patients is 2.6 mCi, as an intravenous injection. The optimal dose adjustment on the basis of body size or weight has not been determined [see Use in Special Populations (8.4)].

2.3 Patient Preparation

- To minimize the radiation absorbed dose to the bladder, encourage adequate hydration. Encourage the patient to drink water or other fluids (as tolerated) in the 4 hours before their PET study.
- Encourage the patient to void as soon as the imaging study is completed and as often as possible thereafter for at least one hour.
- Screen patients for clinically significant blood glucose abnormalities by obtaining a history and/or laboratory tests [see Warnings and Precautions (5.2)]. Prior to Fludeoxyglucose F 18 PET imaging in the oncology and neurology settings, instruct patient to fast for 4 to 6 hours prior to the drug's injection.
- In the cardiology setting, administration of glucose-containing food or liquids (e.g., 50 to 75 grams) prior to Fludeoxyglucose F18 Injection facilitates localization of cardiac ischemia

2.4 Radiation Dosimetry

The estimated human absorbed radiation doses (rem/mCi) to a newborn (3.4 kg), 1-year-old (9.8 kg), 5-year-old (19 kg), 10-year-old (32 kg), 15-year-old (57 kg), and adult (70 kg) from intravenous administration of Fludeoxyglucose F 18 Injection are shown in Table 1. These estimates were calculated based on human[2] data and using the data published by the International Commission on Radiological Protection[4] for Fludeoxyglucose ^{18}F. The dosimetry data show that there are slight variations in absorbed radiation dose for various organs in each of the age groups. These dissimilarities in absorbed radiation dose are due to developmental age variations (e.g., organ size, location, and overall metabolic rate for each age group). The identified critical organs (in descending order) across all age groups evaluated are the urinary bladder, heart, pancreas, spleen, and lungs.

Table 1. Estimated Absorbed Radiation Doses (rem/mCi) After Intravenous Administration of Fludeoxyglucose F-18 Injection[a]

Organ	Newborn	1-year-old	5-year-old	10-year-old	15-year-old	Adult
	(3.4 kg)	(9.8 kg)	(19 kg)	(32 kg)	(57 kg)	(70 kg)
Bladder wallb	4.3	1.7	0.93	0.60	0.40	0.32
Heart wall	2.4	1.2	0.70	0.44	0.29	0.22
Pancreas	2.2	0.68	0.33	0.25	0.13	0.096
Spleen	2.2	0.84	0.46	0.29	0.19	0.14
Lungs	0.96	0.38	0.20	0.13	0.092	0.064
Kidneys	0.81	0.34	0.19	0.13	0.089	0.074
Ovaries	0.80	0.8	0.19	0.11	0.058	0.053
Uterus	0.79	0.35	0.19	0.12	0.076	0.062
LLI wall *	0.69	0.28	0.15	0.097	0.060	0.051
Liver	0.69	0.31	0.17	0.11	0.076	0.058
Gallbladder wall	0.69	0.26	0.14	0.093	0.059	0.049
Small intestine	0.68	0.29	0.15	0.096	0.060	0.047
ULI wall **	0.67	0.27	0.15	0.090	0.057	0.046
Stomach wall	0.65	0.27	0.14	0.089	0.057	0.047
Adrenals	0.65	0.28	0.15	0.095	0.061	0.048
Testes	0.64	0.27	0.14	0.085	0.052	0.041
Red marrow	0.62	0.26	0.14	0.089	0.057	0.047
Thymus	0.61	0.26	0.14	0.086	0.056	0.044
Thyroid	0.61	0.26	0.13	0.080	0.049	0.039
Muscle	0.58	0.25	0.13	0.078	0.049	0.039
Bone surface	0.57	0.24	0.12	0.079	0.052	0.041
Breast	0.54	0.22	0.11	0.068	0.043	0.034
Skin	0.49	0.20	0.10	0.060	0.037	0.030
Brain	0.29	0.13	0.09	0.078	0.072	0.070
Other tissues	0.59	0.25	0.13	0.083	0.052	0.042

[a] MIRDOSE 2 software was used to calculate the radiation absorbed dose. Assumptions on the biodistribution based on data from Gallagher et al.1 and Jones et al.2

[b] The dynamic bladder model with a uniform voiding frequency of 1.5 hours was used.

*LLI = lower large intestine; **ULI = upper large intestine

2.5 Radiation Safety – Drug Handling

- Use waterproof gloves, effective radiation shielding, and appropriate safety measures when handling Fludeoxyglucose F 18 Injection to avoid unnecessary radiation exposure to the patient, occupational workers, clinical personnel and other persons.
- Radiopharmaceuticals should be used by or under the control of physicians who are qualified by specific training and experience in the safe use and handling of radionuclides, and whose experience and training have been approved by the appropriate governmental agency authorized to license the use of radionuclides.
- Calculate the final dose from the end of synthesis (EOS) time using proper radioactive decay factors. Assay the final dose in a properly calibrated dose calibrator before administration to the patient [see Description (11.2)].
- The dose of Fludeoxyglucose F 18 used in a given patient should be minimized consistent with the objectives of the procedure, and the nature of the radiation detection devices employed.

2.6 Drug Preparation and Administration

Calculate the necessary volume to administer based on calibration time and dose.
Aseptically withdraw Fludeoxyglucose F 18 Injection from its container.
Inspect Fludeoxyglucose F 18 Injection visually for particulate matter and discoloration before administration, whenever solution and container permit.
Do not administer the drug if it contains particulate matter or discoloration; dispose of these unacceptable or unused preparations in a safe manner, in compliance with applicable regulations. Use Fludeoxyglucose F 18 Injection within 12 hours from the EOS.

2.7 Imaging Guidelines

Initiate imaging within 40 minutes following Fludeoxyglucose F 18 Injection administration.
Acquire static emission images 30 to 100 minutes from the time of injection.

3 DOSAGE FORMS AND STRENGTHS

Multiple-dose 30 mL and 50 mL glass vial containing 0.74 to 7.40 GBq/mL (20 to 200 mCi/mL) of Fludeoxyglucose F 18 Injection and 4.5 mg of sodium chloride with 0.1 to 0.5% w/w ethanol as a stabilizer (approximately 15 to 50 mL volume) for intravenous administration.

4 CONTRAINDICATIONS

None

5 WARNINGS AND PRECAUTIONS

5.1 Radiation Risks

Radiation-emitting products, including Fludeoxyglucose F 18 Injection, may increase the risk for cancer, especially in pediatric patients. Use the smallest dose necessary for imaging and ensure safe handling to protect the patient and health care worker [see Dosage and Administration (2.5)].

5.2 Blood Glucose Abnormalities

In the oncology and neurology setting, suboptimal imaging may occur in patients with inadequately regulated blood glucose levels. In these patients, consider medical therapy and laboratory testing to assure at least two days of normoglycemia prior to Fludeoxyglucose F 18 Injection administration.

6 ADVERSE REACTIONS

Hypersensitivity reactions with pruritus, edema and rash have been reported in the post-marketing setting. Have emergency resuscitation equipment and personnel immediately available.

7 DRUG INTERACTIONS

The possibility of interactions of Fludeoxyglucose F 18 Injection with other drugs taken by patients undergoing PET imaging has not been studied.

8 USE IN SPECIFIC POPULATIONS

8.1 Pregnancy

Pregnancy Category C
Animal reproduction studies have not been conducted with Fludeoxyglucose F 18 Injection. It is also not known whether Fludeoxyglucose F 18 Injection can cause fetal harm when administered to a pregnant woman or can affect reproduction capacity. Consider alternative diagnostic tests in a pregnant woman; administer Fludeoxyglucose F 18 Injection only if clearly needed.

8.3 Nursing Mothers

It is not known whether Fludeoxyglucose F 18 Injection is excreted in human milk. Consider alternative diagnostic tests in women who are breast-feeding. Use alternatives to breast feeding (e.g., stored breast milk or infant formula) for at least 10 half-lives of radioactive decay, if Fludeoxyglucose F 18 Injection is administered to a woman who is breast-feeding.

8.4 Pediatric Use

The safety and effectiveness of Fludeoxyglucose F 18 Injection in pediatric patients with epilepsy is established on the basis of studies in adult and pediatric patients. In pediatric patients with epilepsy, the recommended dose is 2.6 mCi. The optimal dose adjustment on the basis of body size or weight has not been determined. In the oncology or cardiology settings, the safety and effectiveness of Fludeoxyglucose F 18 Injection have not been established in pediatric patients.

11 DESCRIPTION

11.1 Chemical Characteristics

Fludeoxyglucose F 18 Injection is a positron emitting radiopharmaceutical that is used for diagnostic purposes in conjunction with positron emission tomography (PET) imaging. The active ingredient 2-deoxy-2-[^{18}F]fluoro-D-glucose has the molecular formula of $C_6H_{11}{}^{18}FO_5$ with a molecular weight of 181.26, and has the following chemical structure:

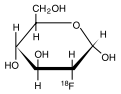

Fludeoxyglucose F 18 Injection is provided as a ready to use sterile, pyrogen free, clear, colorless solution. Each mL contains between 0.740 to 7.40GBq (20.0 to 200 mCi) of 2-deoxy-2-[18F]fluoro-D-glucose at the EOS, 4.5 mg of sodium chloride and 0.1 to 0.5% w/w ethanol as a stabilizer. The pH of the solution is between 4.5 and 7.5. The solution is packaged in a multiple-dose glass vial and does not contain any preservative.

11.2 Physical Characteristics

Fluorine F 18 decays by emitting positron to Oxygen O 16 (stable) and has a physical half-life of 109.7 minutes. The principal photons useful for imaging are the dual 511 keV gamma photons, that are produced and emitted simultaneously in opposite direction when the positron interacts with an electron (Table 2).

Table 2. Pricipal Radiation Emission Data for Fluorine F18

Radiation/Emission	% Per Disintegration	Mean Energy
Positron (b+)	96.73	249.8 keV
Gamma (±)*	193.46	511.0 keV

*Produced by positron annihilation
From: Kocher, D.C. Radioactive Decay Tables DOE/TIC-I 1026, 89 (1981)
The specific gamma ray constant (point source air kerma coefficient) for fluorine F 18 is 5.7 R/hr/mCi (1.35 x 10-6 Gy/hr/kBq) at 1 cm. The half-value layer (HVL) for the 511 keV photons is 4 mm lead (Pb). The range of attenuation coefficients for this radionuclide as a function of lead shield thickness is shown in Table 3. For example, the interposition of an 8 mm thickness of Pb, with a coefficient of attenuation of 0.25, will decrease the external radiation by 75%.

Table 3. Radiation Attenuation of 511 keV Photons by lead (Pb) shielding

Shield thickness (Pb) mm	Coefficient of attenuation
0	0.00
4	0.50
8	0.25
13	0.10
26	0.01
39	0.001
52	0.0001

For use in correcting for physical decay of this radionuclide, the fractions remaining at selected intervals after calibration are shown in Table 4.

Table 4. Physical Decay Chart for Fluorine F18

Minutes	Fraction Remaining
0*	1.000
15	0.909
30	0.826
60	0.683
110	0.500
220	0.250

*calibration time

12 CLINICAL PHARMACOLOGY

12.1 Mechanism of Action

Fludeoxyglucose F 18 is a glucose analog that concentrates in cells that rely upon glucose as an energy source, or in cells whose dependence on glucose increases under pathophysiological conditions. Fludeoxyglucose F 18 is transported through the cell membrane by facilitative glucose transporter proteins and is phosphorylated within the cell to [18F] FDG-6-phosphate by the enzyme hexokinase. Once phosphorylated it cannot exit until it is dephosphorylated by glucose-6-phosphatase. Therefore, within a given tissue or pathophysiological process, the retention and clearance of Fludeoxyglucose F 18 reflect a balance involving glucose transporter, hexokinase and glucose-6-phosphatase activities. When allowance is made for the kinetic differences between glucose and Fludeoxyglucose F 18 transport and phosphorylation (expressed as the ‚lumped constant" ratio), Fludeoxyglucose F 18 is used to assess glucose metabolism. In comparison to background activity of the specific organ or tissue type, regions of decreased or absent uptake of Fludeoxyglucose F 18 reflect the decrease or absence of glucose metabolism. Regions of increased uptake of Fludeoxyglucose F 18 reflect greater than normal rates of glucose metabolism.

12.2 Pharmacodynamics

Fludeoxyglucose F 18 Injection is rapidly distributed to all organs of the body after intravenous administration. After background clearance of Fludeoxyglucose F 18 Injection, optimal PET imaging is generally achieved between 30 to 40 minutes after administration. In cancer, the cells are generally characterized by enhanced glucose metabolism partially due to (1) an increase in activity of glucose transporters, (2) an increased rate of phosphorylation activity, (3) a reduction of phosphatase activity or, (4) a dynamic alteration in the balance among all these processes. However, glucose metabolism of cancer as reflected by Fludeoxyglucose F 18 accumulation shows considerable variability. Depending on tumor type, stage, and location, Fludeoxyglucose F 18 accumulation may be increased, normal, or decreased. Also, inflammatory cells can have the same variability of uptake of Fludeoxyglucose F 18. In the heart, under normal aerobic conditions, the myocardium meets the bulk of its energy requirements by oxidizing free fatty acids. Most of the exogenous glucose taken up by the myocyte is converted into glycogen. However, under ischemic conditions, the oxidation of free fatty acids decreases, exogenous glucose becomes the preferred myocardial sub strate, glycolysis is stimulated, and glucose taken up by the myocyte is metabolized immediately instead of being converted into glycogen. Under these conditions, phosphorylated Fludeoxyglucose F 18 accumulates in the myocyte and can be detected with PET imaging. In the brain, cells normally rely on aerobic metabolism. In epilepsy, the glucose metabolism varies. Generally, during a seizure, glucose metabolism increases. Interictally, the seizure focus tends to be hypometabolic.

12.3 Pharmacokinetics

Distribution: In four healthy male volunteers, receiving an intravenous administration of 30 seconds in duration, the arterial blood level profile for Fludeoxyglucose F 18 decayed triexponentially. The effective half-life ranges of the three phases were 0.2 to 0.3 minutes, 10 to 13 minutes with a mean and standard deviation (STD) of 11.6 (±) 1.1 min, and 80 to 95 minutes with a mean and STD of 88 (±) 4 min. Plasma protein binding of Fludeoxyglucose F 18 has not been studied.

Metabolism: Fludeoxyglucose F 18 is transported into cells and phosphorylated to [18F]-FDG-6-phosphate at a rate proportional to the rate of glucose utilization within that tissue. [F18]-FDG-6-phosphate presumably is metabolized to 2-deoxy-2-[F18]fluoro-6-phospho-D-mannose([F 18]FDM-6-phosphate).

Fludeoxyglucose F 18 Injection may contain several impurities (e.g., 2-deoxy-2-chloro-D-glucose (ClDG)). Biodistribution and metabolism of ClDG are presumed to be similar to Fludeoxyglucose F 18 and would be expected to result in intracellular formation of 2-deoxy-2-chloro-6-phospho-D-glucose (ClDG-6-phosphate) and 2-deoxy-2-chloro-6-phospho-D-mannose (ClDM-6-phosphate). The phosphorylated deoxyglucose compounds are dephosphorylated and the resulting compounds (FDG, FDM, ClDG, and ClDM) presumably leave cells by passive diffusion. Fludeoxyglucose F 18 and related compounds are cleared from non-cardiac tissues within 3 to 24 hours after administration. Clearance from the cardiac tissue may require more than 96 hours. Fludeoxyglucose F 18 that is not involved in glucose metabolism in any tissue is then excreted in the urine.

Elimination: Fludeoxyglucose F 18 is cleared from most tissues within 24 hours and can be eliminated from the body unchanged in the urine. Three elimination phases have been identified in the reviewed literature. Within 33 minutes, a mean of 3.9% of the administrated radioactive dose was measured in the urine. The amount of radiation exposure of the urinary bladder at two hours post-administration suggests that 20.6% (mean) of the radioactive dose was present in the bladder.

Special Populations: The pharmacokinetics of Fludeoxyglucose F 18 Injection have not been studied in renally-impaired, hepatically impaired or pediatric patients. Fludeoxyglucose F 18 is eliminated through the renal system. Avoid excessive radiation exposure to this organ system and adjacent tissues. The effects of fasting, varying blood sugar levels, conditions of glucose intolerance, and diabetes mellitus on Fludeoxyglucose F 18 distribution in humans have not been ascertained [see Warnings and Precautions (5.2)].

13 NONCLINICAL TOXICOLOGY

13.1 Carcinogenesis, Mutagenesis, Impairment of Fertility

Animal studies have not been performed to evaluate the Fludeoxyglucose F 18 Injection carcinogenic potential, mutagenic potential or effects on fertility.

14 CLINICAL STUDIES

14.1 Oncology

The efficacy of Fludeoxyglucose F 18 Injection in positron emission tomography cancer imaging was demonstrated in 16 independent studies. These studies prospectively evaluated the use of Fludeoxyglucose F 18 in patients with suspected or known malignancies, including non-small cell lung cancer, colo-rectal, pancreatic, breast, thyroid, melanoma, Hodgkin's and non-Hodgkin's lymphoma, and various types of metastatic cancers to lung, liver, bone, and axillary nodes. All these studies had at least 50 patients and used pathology as a standard of truth. The Fludeoxyglucose F 18 Injection doses in the studies ranged from 200 MBq to 740 MBq with a median and mean dose of 370 MBq. In the studies, the diagnostic performance of Fludeoxyglucose F 18 Injection varied with the type of cancer, size of cancer, and other clinical conditions. False negative and false positive scans were observed. Negative Fludeoxyglucose F 18 Injection PET scans do not exclude the diagnosis of cancer. Positive Fludeoxyglucose F 18 Injection PET scans can not replace pathology to establish a diagnosis of cancer. Non-malignant conditions such as fungal infections, inflammatory processes and benign tumors have patterns of increased glucose metabolism that may give rise to false-positive scans. The efficacy of Fludeoxyglucose F 18 Injection PET imaging in cancer screening was not studied.

14.2 Cardiology

The efficacy of Fludeoxyglucose F 18 Injection for cardiac use was demonstrated in ten independent, prospective studies of patients with coronary artery disease and chronic left ventricular systolic dysfunction who were scheduled to undergo coronary revascularization. Before revascularization, patients underwent PET imaging with Fludeoxyglucose F 18 Injection (74 to 370 MBq, 2 to 10 mCi) and perfusion imaging with other diagnostic radiopharmaceuticals. Doses of Fludeoxyglucose F 18 Injection ranged from 74 to 370 MBq (2 to 10 mCi). Segmental, left ventricular, wall-motion assessments of asynergic areas made before revascularization were compared in a blinded manner to assessments made after successful revascularization to identify myocardial segments with functional recovery. Left ventricular myocardial segments were predicted to have reversible loss of systolic function if they showed Fludeoxyglucose F 18 accumulation and reduced perfusion (i.e., flow-metabolism mismatch). Conversely, myocardial segments were predicted to have irreversible loss of systolic function if they showed reductions in both Fludeoxyglucose F 18 accumulation and perfusion (i.e., matched defects). Findings of flow-metabolism mismatch in a myocardial segment may suggest that successful revascularization will restore myocardial function in that segment. However, false-positive tests occur regularly, and the decision to have a patient undergo revascularization should not be based on PET findings alone. Similarly, findings of a matched defect in a myocardial segment may suggest that myocardial function will not recover in that segment, even if it is successfully revascularized. However, false-negative tests occur regularly, and the decision to recommend against coronary revascularization, or to recommend a cardiac transplant, should not be based on PET findings alone. The reversibility of segmental dysfunction as predicted with Fludeoxyglucose F 18 PET imaging depends on successful coronary revascularization. Therefore, in patients with a low likelihood of successful revascularization, the diagnostic usefulness of PET imaging with Fludeoxyglucose F 18 Injection is more limited.

14.3 Neurology

In a prospective, open label trial, Fludeoxyglucose F 18 Injection was evaluated in 86 patients with epilepsy. Each patient received a dose of Fludeoxyglucose F 18 Injection in the range of 185 to 370 MBq (5 to 10 mCi). The mean age was 16.4 years (range: 4 months to 58 years; of these, 42 patients were less than 12 years and 16 patients were less than 2 years old). Patients had a known diagnosis of complex partial epilepsy and were under evaluation for surgical treatment of their seizure disorder. Seizure foci had been previously identified on ictal EEGs and sphenoidal EEGs. Fludeoxyglucose F 18 Injection PET imaging confirmed previous diagnostic findings in 16% (14/87) of the patients; in 34% (30/87) of the patients, Fludeoxyglucose F 18 Injection PET images provided new findings. In 32% (27/87), imaging with Fludeoxyglucose F 18 Injection was inconclusive. The impact of these imaging findings on clinical outcomes is not known. Several other studies comparing imaging with Fludeoxyglucose F 18 Injection results to subsphenoidal EEG, MRI and/or surgical findings supported the concept that the degree of hypometabolism corresponds to areas of confirmed epileptogenic foci. The safety and effectiveness of Fludeoxyglucose F 18 Injection to distinguish idiopathic epileptogenic foci from tumors or other brain lesions that may cause seizures have not been established.

15 REFERENCES

1. Gallagher B.M., Ansari A., Atkins H., Casella V., Christman D.R., Fowler J.S., Ido T., MacGregor R.R., Som P., Wan C.N., Wolf A.P., Kuhl D.E., and Reivich M. "Radiopharmaceuticals XXVII. 18F-labeled 2-deoxy-2-fluoro-d-glucose as a radiopharmaceutical for measuring regional myocardial glucose metabolism in vivo: tissue distribution and imaging studies in animals," J Nucl Med, 1977; 18, 990-6.
2. Jones S.C., Alavi, A., Christman D., Montanez, I., Wolf, A.P., and Reivich M. "The radiation dosimetry of 2 [F-18] fluoro-2-deoxy-D-glucose in man," J Nucl Med, 1982; 23, 613-617. 3. Kocher, D.C. "Radioactive Decay Tables: A handbook of decay data for application to radiation dosimetry and radiological assessments," 1981, DOE/TIC-I 1026, 89.
4. ICRP Publication 53, Volume 18, No. l-4,1987, pages 75-76.

16 HOW SUPPLIED/STORAGE AND DRUG HANDLING

Fludeoxyglucose F 18 Injection is supplied in a multi-dose, capped 30 mL and 50 mL glass vial containing between 0.740 to 7.40 GBq/mL (20 to 200 mCi/mL), of no carrier added 2-deoxy-2-[F 18] fluoro-D-glucose, at end of synthesis, in approximately 15 to 50 mL. The contents of each vial are sterile, pyrogen-free and preservative-free.

NDC 40028-511-30; 40028-511-50

Receipt, transfer, handling, possession, or use of this product is subject to the radioactive material regulations and licensing requirements of the U.S. Nuclear Regulatory Commission, Agreement States or Licensing States as appropriate.

Store the Fludeoxyglucose F 18 Injection vial upright in a lead shielded container at 25°C (77°F); excursions permitted to 15-30°C (59-86°F).

Store and dispose of Fludeoxyglucose F 18 Injection in accordance with the regulations and a general license, or its equivalent, of an Agreement State or a Licensing State.

The expiration date and time are provided on the container label. Use Fludeoxyglucose F 18 Injection within 12 hours from the EOS time.

17 PATIENT COUNSELING INFORMATION

Instruct patients in procedures that increase renal clearance of radioactivity.

Encourage patients to:

- drink water or other fluids (as tolerated) in the 4 hours before their PET study.
- void as soon as the imaging study is completed and as often as possible thereafter for at least one hour.

Manufactured by: PETNET Solutions Inc.
810 Innovation Drive
Knoxville, TN 37932

Distributed by: PETNET Solutions Inc.
810 Innovation Drive
Knoxville, TN 37932

PETNET Solutions

PN0002262 Rev. A

March 1, 2011

Fludeoxyglucose F^{18} 5-10mCi as an IV injection Indications and Usage

Fludeoxyglucose F^{18} Injection is indicated for positron emission tomography (PET) imaging in the following settings:

Oncology: For assessment of abnormal glucose metabolism to assist in the evaluation of malignancy in patients with known or suspected abnormalities found by other testing modalities, or in patients with an existing diagnosis of cancer.

Cardiology: For the identification of left ventricular myocardium with residual glucose metabolism and reversible loss of systolic function in patients with coronary artery disease and left ventricular dysfunction, when used together with myocardial perfusion imaging.

Neurology: For the identification of regions of abnormal glucose metabolism associated with foci of epileptic seizures.

Important Safety Information

Radiation Risks: Radiationemitting products, including Fludeoxyglucose F^{18} Injection, may increase the risk for cancer, especially in pediatric patients. Use the smallest dose necessary for imaging and ensure safe handling to protect the patient and healthcare worker.

Blood Glucose Abnormalities: In the oncology and neurology setting, suboptimal imaging may occur in patients with inadequately regulated blood glucose levels. In these patients, consider medical therapy and laboratory testing to assure at least two days of normoglycemia prior to Fludeoxyglucose F^{18} Injection administration.

Adverse Reactions: Hypersensitivity reactions with pruritus, edema and rash have been reported; have emergency resuscitation equipment and personnel immediately available.

Dosage Forms and Strengths: Multiple-dose 30 mL and 50 mL glass vial containing 0.74 to 7.40 GBq/mL (20 to 200 mCi/mL) of Fludeoxyglucose F^{18} injection and 4.5 mg of sodium chloride with 0.1 to 0.5% w/w ethanolas a stabilizer (approximately 15 to 50 mL volume) for intravenous administration. Fludeoxyglucose F^{18} injection is manufactured by Siemens' PETNET Solutions, 810 Innovation Drive, Knoxville, TN 39732, USA.

Reference Normal Values for Myocardial T1 and T2 Maps with the MAGNETOM Vida 3T System and Case Examples from Clinical Practice

Guillem Pons-Lladó, M.D., Ph.D.

Cardiac Imaging Unit, Department of Diagnostic Imaging, Clínica Corachán, Barcelona, Spain

Abstract

T1 and T2 mapping techniques have become an important component of the study of myocardial tissue characterization in cardiac MR examinations. Easy to acquire, highly reliable, and quantifiable, thanks to their pixel-based conception, T1 and T2 maps provide radiologists and cardiologists with accurate information on the presence (or absence) and degree of myocardial tissue fibrosis, edema, or infiltrative processes. Their usefulness for the diagnosis and prognosis of patients with a variety of myocardial diseases has been extensively proven. Implicit in the nature of these techniques, however, is that the range of normal values is dependent on the field strength of the system and the software used for the acquisition. For this reason, it is recommended that every local MR facility investigates the range of reference values prior to their clinical application.

This paper presents preliminary data on myocardial T1 and T2 values from mapping performed on a series of healthy individuals at our institution using a MAGNETOM Vida 3T system. Also, as an illustration of the practical usefulness of this information, two clinical cases are presented in detail, with a particular focus on the relevance of T1 and T2 values for the diagnosis and management of patients.

Basis and rationale of T1 and T2 mapping techniques in cardiac diagnosis

By introducing techniques capable of providing information on the intrinsic magnetic properties of tissues, Cardiovascular Magnetic Resonance (CMR) has increased its potential to act as a comprehensive diagnostic tool. Over the last decade, T1 and T2 mapping sequences have made reliable pixel-based measurements of myocardial longitudinal and transverse relaxation times possible [1, 2]. Based, respectively, on a single breath-hold acquisition of a series of inversion recovery images with varying inversion time (TI), or a series of multiecho datasets with varying echo time (TE), T1 and T2 maps have become essential components of the body of information on tissue characterization that is available from a CMR study.

Extensive histologic validation has proven that there is a correlation between T1 mapping values and the presence and degree of diffuse interstitial myocardial fibrosis [3]. Due to deposition of proteins or other substances with magnetic properties (lipids or iron, for instance), T1 values are also sensitive to other pathological processes, either intra- or extracellular, such as myocardial

	T1 native (ms) n = 24	T1 post contrast (ms) n = 12	ECV fraction (%) n = 12	T2 (ms) n = 24
Mean ± SD	1230 ± 38.5	508 ± 50	25 ± 2.5	39 ± 2.2
Maximal normal value	1307	608	30	43
Minimal normal value	1153	408	20	34

Table 1: Results.

edema or infiltration [4]. One method that helps us to distinguish between them is a T1-derived calculation, the extracellular volume (ECV) fraction, which can be obtained from native and postcontrast T1 myocardial and blood pool maps, and also requires the hematocrit value [4]. T2 myocardial values, on the other hand, have proven to be extremely accurate in identifying tissue edema [5], such as that which is present in cases of acute coronary syndrome or in myocarditis.

The availability of mapping techniques is thus a key resource in current CMR studies, particularly since large multicenter studies have demonstrated the prognostic value of T1 and ECV in patients with dilated cardiomyopathy, of either idiopathic or ischemic origin [6, 7].

Reference normal values on a MAGNETOM Vida 3T system

While several authoritative documents on reference normal values have been published [8–10], we must bear in mind that T1 and T2 myocardial values depend not only on the tissue composition but also on the MR field strength and software used [4]. In light of this, the aim of the present paper is to present the preliminary information on normal values derived from our initial experience of using a MAGNETOM Vida 3T system, given that, to the best of our knowledge, no data have been published on this issue to date.

Population studied

T1 and T2 mapping sequences were performed on a series of 24 individuals (18 men), with a mean age of 50.8 ± 14.3 (range: 19–86) who, based on a CMR study, were deemed to be free of myocardial disease or any type of disorder capable of inducing an impairment of the left ventricular (LV) muscle. Reasons for the referral for CMR had been: a technically inadequate echocardiographic study during a routine checkup (10 cases); suspected (and not confirmed) LV hypertrophy (8 cases); suspected (confirmed or not) aortic dilatation (3 cases); and MR angiography of the pulmonary veins before an ablation procedure for paroxysmal atrial fibrillation (3 cases).

CMR acquisition parameters and analysis

Studies were performed on a MAGNETOM Vida 3T system with the XA10A software version, equipped with a 60-channel body coil.

T1 mapping was obtained by a single shot TrueFISP inversion recovery sequence prepared with multiple inversions combined with sampling and recovery periods. An ECG-gated, motion-corrected, short axis slice was prescribed at the mid ventricular level with the following parameters: slice thickness: 8 mm; TE: 1.06 ms; minimum TI 100 ms with 80 ms increments according to a 5(3)3 scheme; matrix size: 256 (phase res.: 66%); FOV (rectangular): 360 mm (phase FOV: 85.2%); bandwidth: 1085 Hz/px; flip angle: 35°. In the patients requiring a contrast study, and for whom a recent hematocrit value was available (n = 12), the sequence was repeated 15 minutes after a 0.2 mmol/kg dose of contrast (gadoteric acid) had been given.

T2 mapping was based on a GRE single shot FLASH readout with multiple T2 preparations and recovery periods. An ECG-gated, motion-corrected, short axis slice was prescribed at the mid ventricular level with the following parameters: slice thickness: 8 mm; TE: 1.28 ms; No. of T2 preps: 3 (0, 35, 55 ms); matrix size: 192 (phase res.: 75%); FOV (rectangular): 360 mm (phase FOV: 80.2%); bandwidth: 1184 Hz/px; flip angle: 12°. This sequence was obtained only before contrast was given.

T1 and T2 values were read using Siemens Healthineers *syngo*.via software on regions of interest (ROIs) with an area of 0.5–1 cm^2 manually placed at the level of the mid ventricular septum on the parametric map images obtained from the sequences detailed above. In the 12 patients with a contrast study and a hematocrit value available, ROIs were also drawn on the LV blood pool of the T1 map images and both tissue and blood pool measurements were repeated on the postcontrast images. In these cases, the ECV fraction was calculated using the equation [4]:

$$ECV = \frac{1/T1\ myoc\ post\ Gad - 1/T1\ myoc\ native}{1/T1\ blood\ post\ Gad - 1/T1\ blood\ native} \bullet 100\text{-hematocrit}$$

Results

The results of these calculations are presented in Table 1. Upper and lower normal values are determined as the mean value plus and minus 2 SD, respectively, as recommended [4].

Case examples

The availability of a range of normal values obtained locally provides a robust basis for these techniques to be applied in clinical practice. Two case examples from our experience are described below.

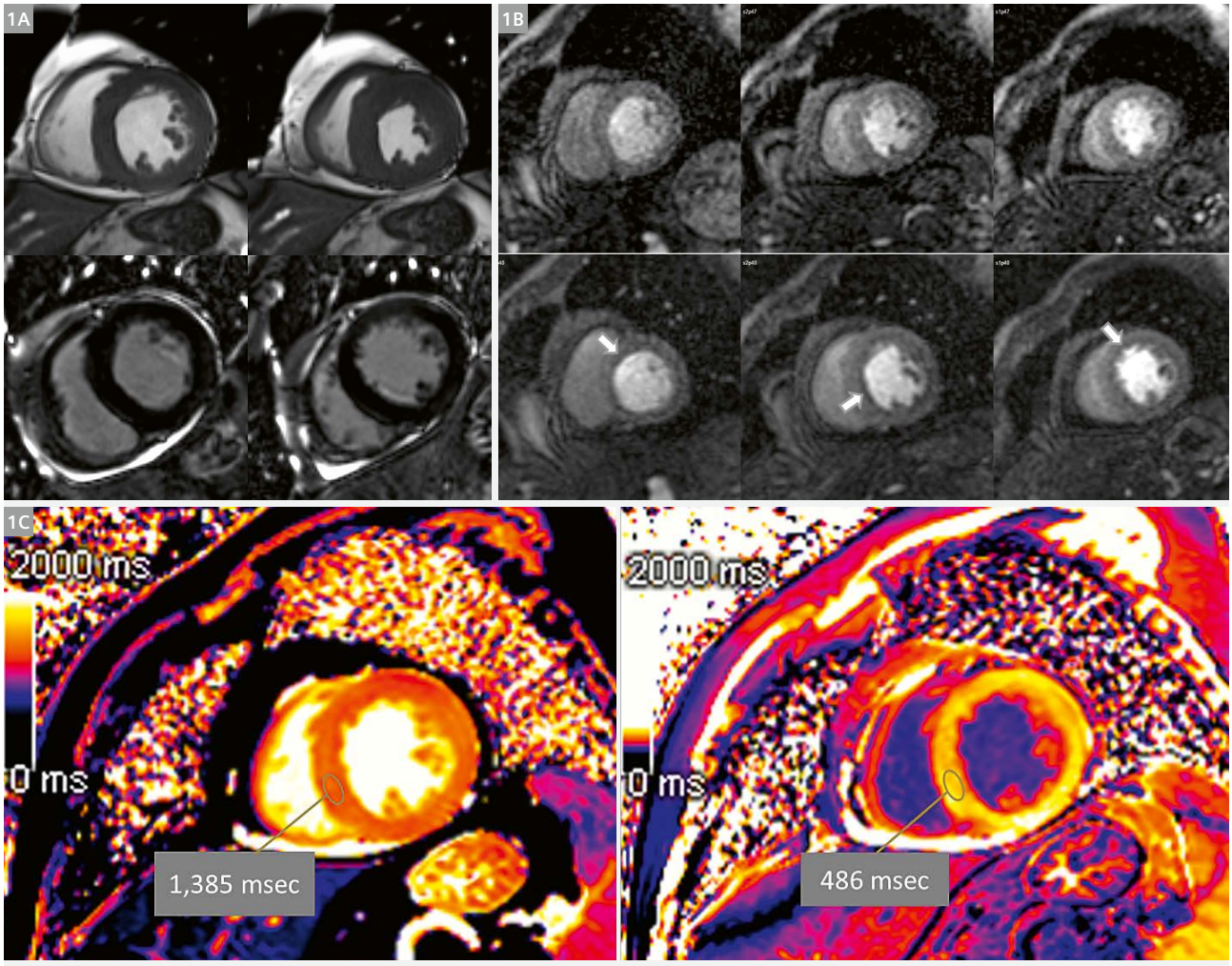

Figure 1:
(1A) End-diastolic (top left) and end-systolic (top right) frames from cine sequences obtained on a short axis mid ventricular plane, and delayed enhancement images (bottom row) obtained from the same patient 10 minutes after contrast injection.

(1B) Contrast first-pass perfusion studies performed at rest (top row) and at 4 minutes of an adenosine infusion (adenosine triphosphate at 160 mcg/kg/min) (bottom row). Arrows point to a diffuse, annular, subendocardial stress induced perfusion defect.

(1C) Native (left) and postcontrast (right) parametric T1 map images with ROIs showing the corresponding calculated myocardial T1 values.

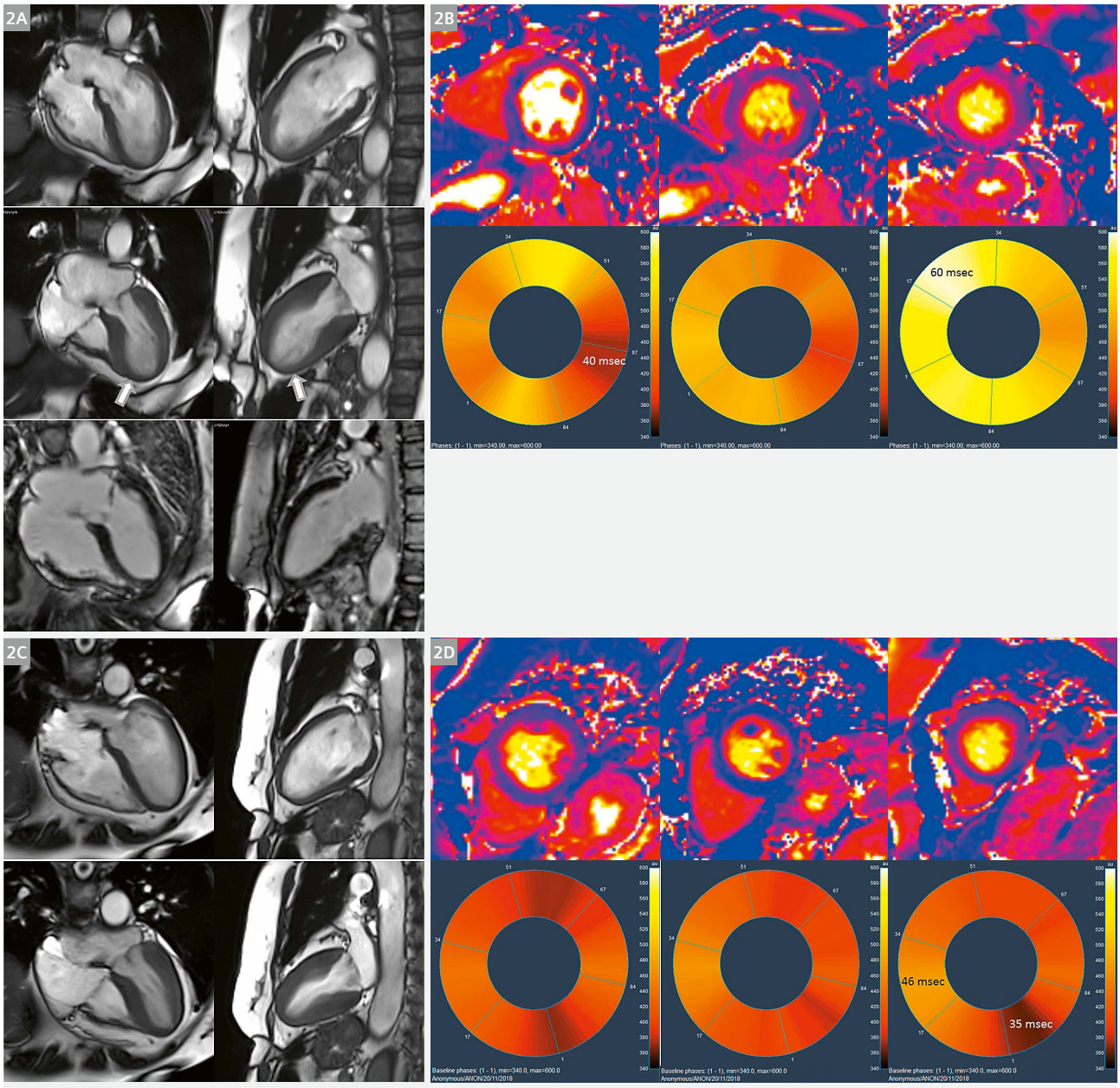

Figure 2:
(2A) End-diastolic (top row) and end-systolic (middle row) frames from cine sequences obtained in 4-chamber (left panels) and 2-chamber views (right panels): A marked dyskinesia of the LV apical region is seen (arrows). No apparent myocardial enhancement is observed on the same planes in IR sequences obtained 10 minutes after contrast injection (bottom row).

(2B) Parametric images from T2 map sequences obtained at basal, middle, and apical short axis LV planes (top row), and maps of the corresponding T2 values (bottom row, analyzed using Medis 7.1 QMass software[1]). Values within normal limits (< 43 msec) are observed only at the basal lateral region, while the septal anterior apical wall shows the highest readings.

(2C) Follow-up CMR study performed on the same patient. End-diastolic (top row) and end-systolic (bottom row) frames from cine sequences obtained in 4-chamber (left panels) and 2-chamber views (right panels) show recovery of the apical dyskinesia observed in the previous study (Fig. 2A).

(2D) Follow-up parametric images from T2 map sequences obtained at basal, middle, and apical short axis LV planes (top row), and maps of the corresponding T2 values (bottom row), both with the same orientation and analysis method as in the study shown in Figure 2B. Nearly complete normalization of values is determined compared with the previous examination.

[1] *The information shown refers to products of third-party manufacturers and are thus their regulatory responsibility. Please contact the third-party manufacturer for further information.*

The first patient, illustrated in Figure 1 (A–C), was a 74-year-old man with long-standing hypertension who presented with chest pain and signs and symptoms of heart failure. An earlier echo scan had shown LV dysfunction and angiography had shown non-obstructive coronary artery disease (CAD). CMR showed definite concentric LV hypertrophy with moderately reduced ejection fraction (estimated at 36%) and absence of any identifiable focal intramyocardial fibrosis in the delayed contrast enhancement study (Fig. 1A). A stress-induced myocardial perfusion defect was seen (Fig. 1B), with features consistent with diffuse coronary microvascular dysfunction. Finally, T1 mapping sequences (Fig. 1C) showed a relatively high native value (1385 ms) and, after a postcontrast study, also an abnormally high calculated ECV fraction (32%). The CMR study in this patient constitutes a full picture of an advanced case of hypertensive heart disease, with LV remodeling and dysfunction, microvascular CAD, and significant diffuse intramyocardial fibrosis and interstitial expansion. Interestingly, this patient did not present with focal fibrosis at the standard delayed enhancement study, a feature which could have erroneously led his cardiologists to make a less adverse prognosis.

The second patient (Figs. 2A–D) was a 72-year-old woman who was admitted with clinical and ECG data suggesting an acute coronary syndrome. After an angiographic study showed apparently normal coronary arteries and a region of gross apical dyskinesia, a CMR exam was requested to confirm the diagnosis of Takotsubo syndrome. The study of function and delayed enhancement (Fig. 2A) showed findings typical of apical dyskinesia in the absence of myocardial necrosis, while a T2 map study of the LV myocardium with extensive coverage (Fig. 2B) showed a global increase in values, particularly at the anterior apical region, indicating diffuse, but predominantly anterior, apical distribution of myocardial edema. A follow-up CMR study performed four weeks after the acute episode showed nearly complete resolution of the wall motion abnormality (Fig. 2C) and also of the myocardial edema (Fig. 2D), as we would expect to occur in Takotsubo cardiomyopathy patients with a favorable outcome.

Contact

Guillem Pons-Lladó, M.D., Ph.D.
Av. Sant Antoni M. Claret 158A, 4/3
08025 Barcelona
Spain
Tel.: +34 607 26 38 48
gponsllado@gmail.com

Acknowledgement

The author wishes to recognize the contribution that Mr. Alvaro Serrano, MRI Applications Technologist, Siemens Healthineers Spain made to the description of the technical aspects of the sequences.

References:

1 Messroghli DR, et al. Modified Look-Locker Inversion Recovery (MOLLI) for high-resolution T1 mapping of the heart. Magn Reson Med 2004; 52: 141–146.
2 Huang TY, et al. T2 measurement of the human myocardium using a T2-prepared transient-state TrueFISP sequence. Magn Reson Med 2007; 57: 960–966.
3 Diao K-Y, et al. Histologic validation of myocardial fibrosis measured by T1 mapping: a systematic review and meta-analysis. J Cardiovasc Magn Reson 2016; 18: 92.
4 Messroghli DR, et al. Clinical recommendations for cardiovascular magnetic resonance mapping of T1, T2, T2* and extracellular volume: A consensus statement by the Society for Cardiovascular Magnetic Resonance (SCMR) endorsed by the European Association for Cardiovascular Imaging (EACVI). J Cardiovasc Magn Reson 2017; 19: 75.
5 Giri S, et al. T2 quantification for improved detection of myocardial edema. J Cardiovasc Magn Reson 2009; 11: 56.
6 Puntmann VO, et al. T1-Mapping and Outcome in Nonischemic Cardiomyopathy. All-Cause Mortality and Heart Failure. J Am Coll Cardiol Img 2016; 9: 40–50.
7 Puntmann VO, et al. Native T1 and ECV of Noninfarcted Myocardium and Outcome in Patients with Coronary Artery Disease. J Am Coll Cardiol 2018; 71: 766–78.
8 Piechnik SK, et al. Normal variation of magnetic resonance T1 relaxation times in the human population at 1.5 T using ShMOLLI. J Cardiovasc Magn Reson 2013; 15: 13.
9 Dabir D, et al. Reference values for healthy human myocardium using a T1 mapping methodology: results from the International T1 Multicenter cardiovascular magnetic resonance study. J Cardiovasc Magn Reson 2014; 16: 69.
10 Roy C, et al. Age and sex corrected normal reference values of T1, T2 T2* and ECV in healthy subjects at 3T CMR. J Cardiovasc Magn Reson 2017; 19: 72.

MINOCA. Myocardial Infarction with Non-Obstructive Coronary Arteries

Edyta Blaszczyk, M.D.; Jeanette Schulz-Menger, M.D.

Working Group Cardiac MRI, Experimental and Clinical Research Center, a cooperation between the Charité Medical Faculty, the Max-Delbrück Center for Molecular Medicine, and the Department of Cardiology and Nephrology, HELIOS Clinic Berlin Buch, Germany

All cases are illustrating patients with a clinical suspicion for an acute myocardial infarction but normal coronary artery disease.

Case 1

A 27-year-old man was referred to our MR unit from the intensive care unit with a non-ST-elevation myocardial infarction.

The patient was admitted to the hospital because of acute chest pain. Blood tests showed increased troponin values. Coronary angiography did not show any coronary artery stenosis. Subsequently, the patient history revealed that there had been drug abuse over the previous weekend. CMR was performed within the routine workflow at our site to clarify conflicting results. The CMR images are given in Figure 1.

LV showed a normal systolic function without wall motion abnormalities (see Figures 1A and B, as well as the 2CV cine online data supplement). Inferior focal edema could be detected on T2-weighted images (see Fig. 1C and D). Focal necrosis could be shown by applying late gadolinium enhancement to the inferior wall (Fig. 1F–H).

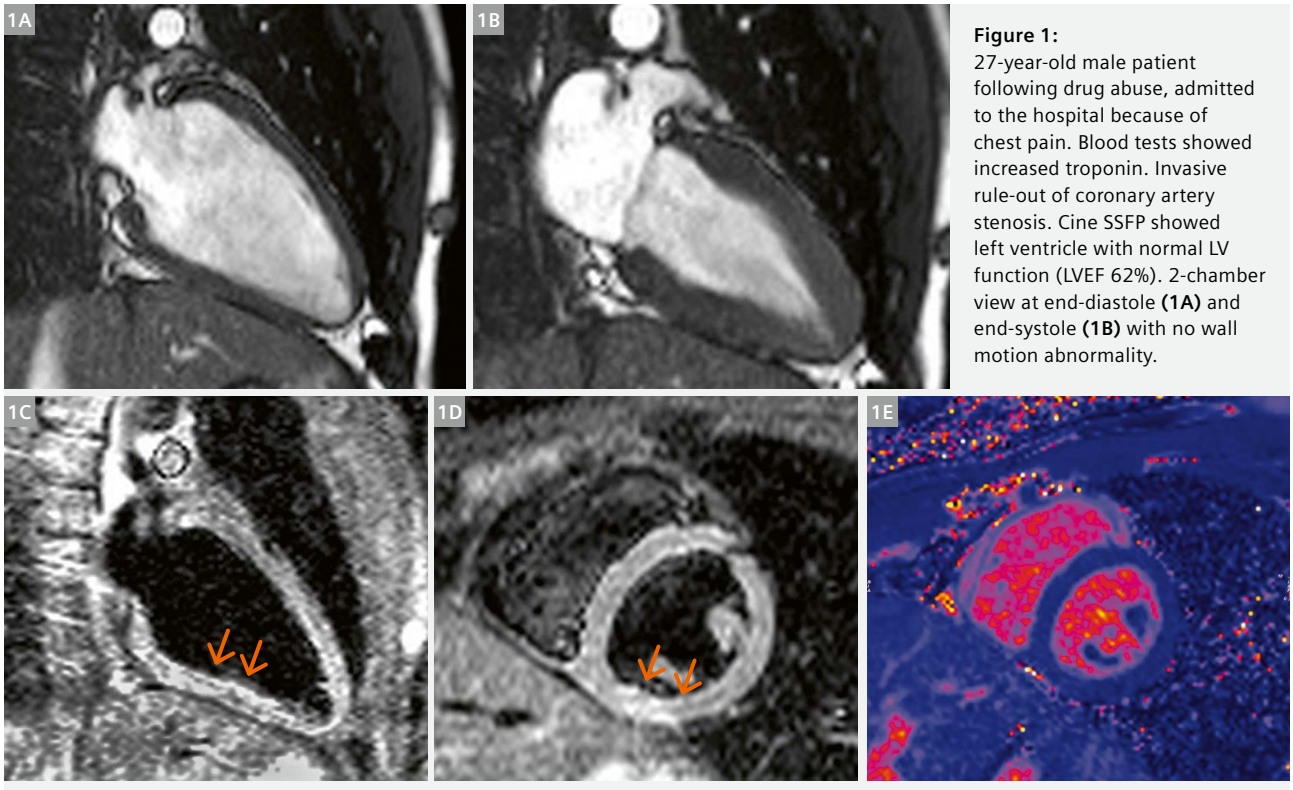

Figure 1:
27-year-old male patient following drug abuse, admitted to the hospital because of chest pain. Blood tests showed increased troponin. Invasive rule-out of coronary artery stenosis. Cine SSFP showed left ventricle with normal LV function (LVEF 62%). 2-chamber view at end-diastole **(1A)** and end-systole **(1B)** with no wall motion abnormality.

Tissue differentiation
T2-weighted images showed focal signal increase in the inferior midventricular indicating myocardial edema **(1C, D)** (arrows). T2 mapping with normal times (48 ms) **(1E)**.

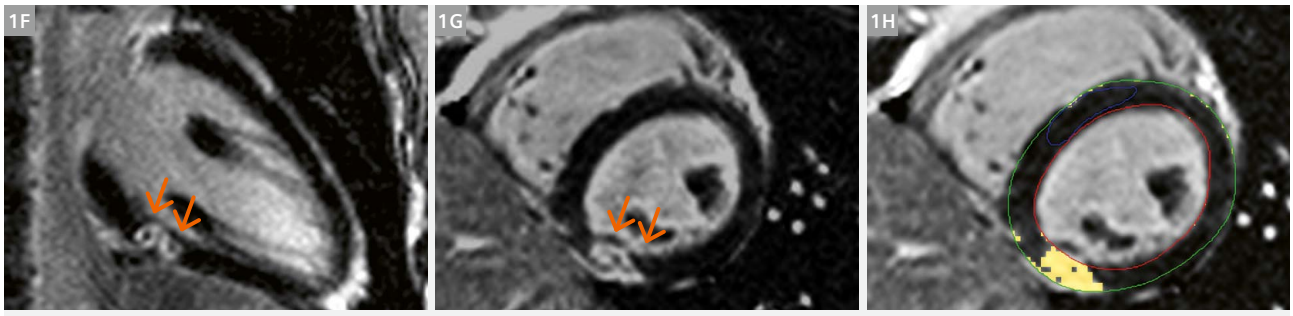

Figure 1: Tissue differentiation
Late gadolinium enhancement (LGE) transmural necrosis inferior **(1F–H)**.

Case 2

Myocarditis mimicking STEMI/NSTEMI is often characterized by young age and history of infection.
A different localization of fibrosis, subepicardial, intramyocardial is often seen in myocarditis (Fig. 2E–G).

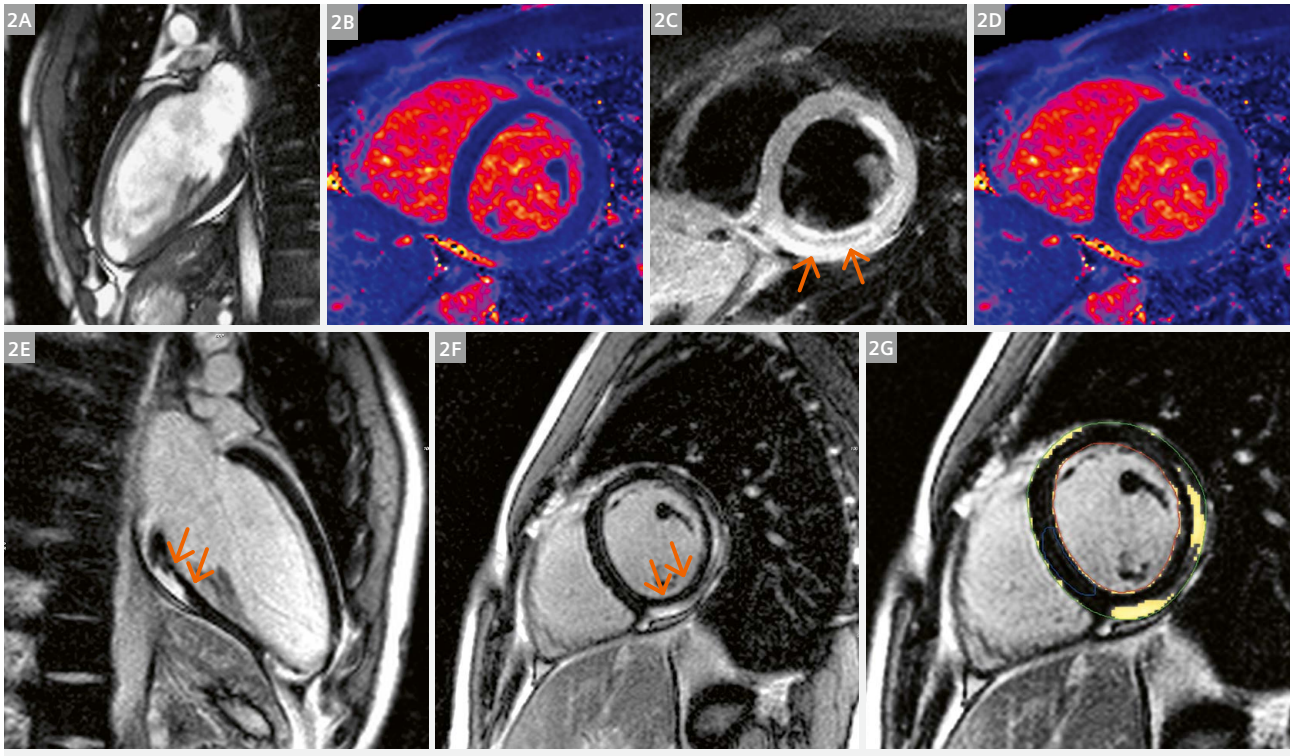

Figure 2:
22-year-old male patient with myocarditis. Cine SSFP showed left ventricle with normal LV function (LVEF 62%). 2-chamber view at end-diastole **(2A)** and end-systole **(2B)** with no wall motion abnormality.

Tissue differentiation:
T2-weighted images showed focal signal increase in the basal inferior pronounced in the subepicardial layer **(2C)** (arrows). T2 mapping showed increased times (64 ms) **(2D)**.

In the late gadolinium enhancement (LGE) in 2-chamber view **(2E)** and short axis **(2F, G)** with subepicardial necrosis inferior and inferolateral.

Case 3

A 57-year-old female patient was referred to our MR Unit from intensive care unit due to non-ST elevation myocardial infarction.

The patient was admitted to the hospital after three days of chest pain and dyspnea. Troponin and CK values were elevated, coronary angiography ruled out coronary artery stenosis. Positive family history of myocardial infarctions (death of father and uncle at young ages). Hyperlipidemia. No acute infections recently.

CMR was performed within the routine workflow at our site to clarify conflicting results.

There is growing awareness among clinicians of myocardial infarction in the absence of obstructive coronary arteries. This is evident in chronic (CMI) as well as acute myocardial infarction (AMI).

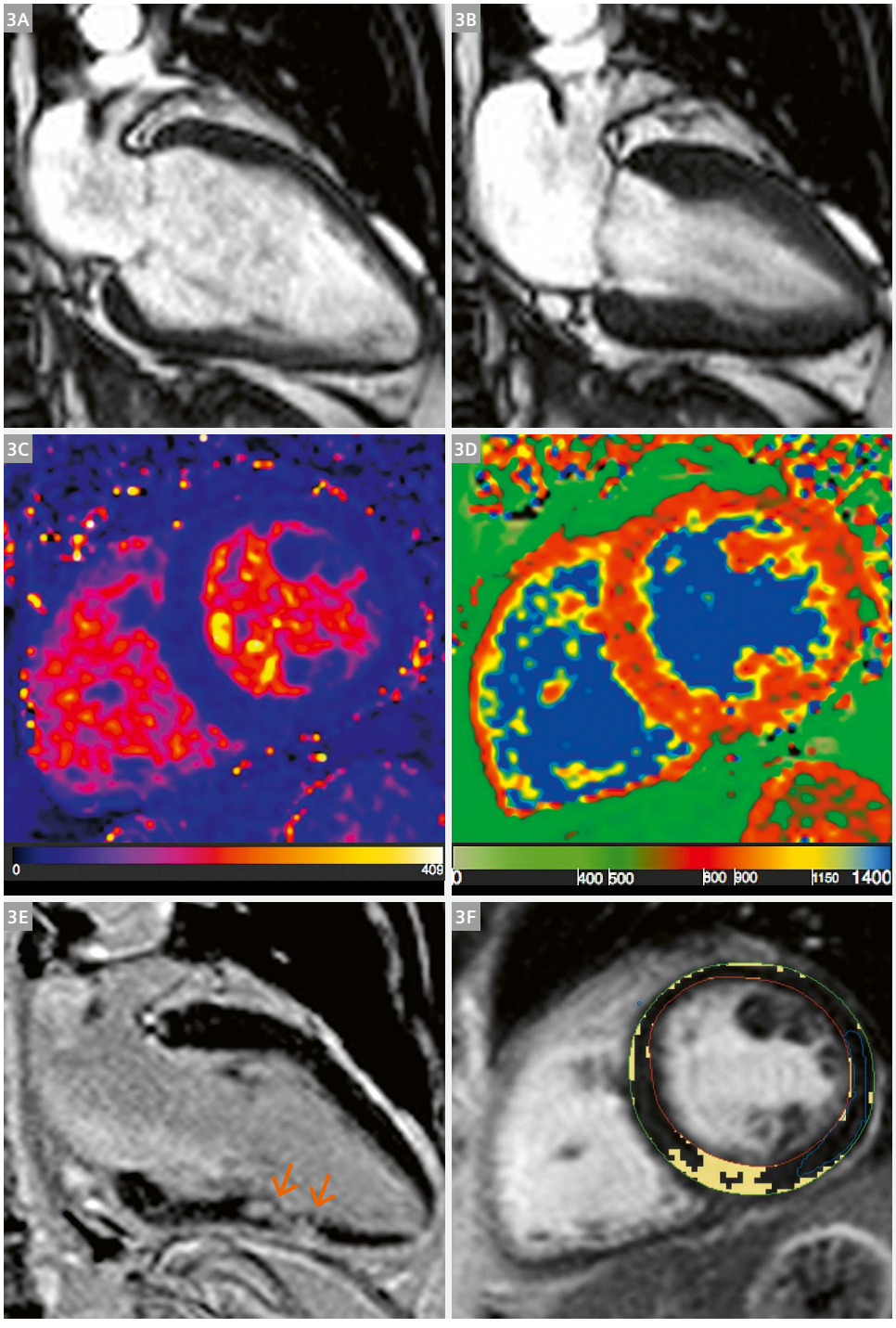

Figure 3:
Cine SSFP of the left ventricle with normal LV function (LVEF 68%). 2-chamber view in end-diastole **(3A)** and end-systole **(3B)** with hypokinesia of the inferior wall midventricular.

Tissue differentiation at 1.5T:
T2 mapping with normal values (max. 55 ms) **(3C)** and T1 mapping with normal native T1 times (max. 1005 ms) **(3D)**. ECV syn max. 23% – within the normal range.

Late gadolinium-enhancement (LGE) transmural scar in the inferior wall midventricular **(3E, F)**.

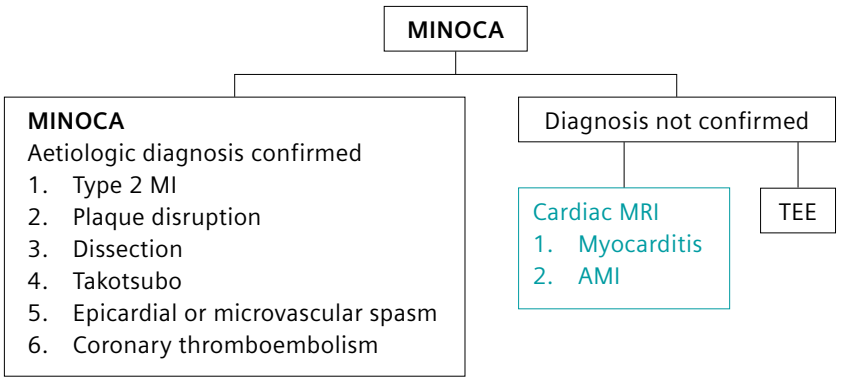

Recommended diagnostic and therapeutic algorithm for myocardial infarction with nonobstructive coronary arteries.
Adapted from reference 2: Agewall S,et al. ESC working group position paper on myocardial infarction with non-obstructive coronary arteries. European Heart Journal. 2017; 38:143-53.

Myocardial infarction with no obstructive coronary atherosclerosis (MINOCA) is a syndrome with different causes characterized by clinical evidence of AMI with normal or near normal coronary arteries in angiography. Previous studies have shown a prevalence of MINOCA of between 10% and 25% among women and between 6% and 10% among men who present with non-ST elevation MI (NSTEMI).

The diagnostic criteria for MINOCA were defined in the 2017 ESC Guidelines for the management of acute myocardial infarction in patients presenting with ST segment elevation [1].
They include:

1. presence of universal AMI criteria,
2. nonobstructive coronary arteries on angiography defined as no coronary artery stenosis ≥ 50%,
3. no clinically overt specific cause for the acute presentation.

Due to the multiple potential causes, the optimal therapy in MINOCA patients has still not been specified and neither has the long-term prognosis in these patients. However, it is well known that small focal fibrosis as shown by CMR has an impact on prognosis [5].

CMR has the unique ability to differentiate myocardial tissue characterization including the detection and localization of edema, focal and diffuse scar/fibrosis. This is already possible in patients with no wall motion abnormalities, but identification in cases of wall motion abnormalities is also possible. For clinical decision-making, knowledge about whether the disease is at an active or non-active stage, as well as the identification of reversible injury, is essential.

The current guidelines [2, 4] indicate that CMR is best performed within 1–2 weeks after the onset of symptoms to increase the diagnostic accuracy of the test in identifying the etiological cause of MINOCA and this should lead to specific treatment strategies.

Contact

Professor Jeanette Schulz-Menger, M.D.
University Medicine Berlin
Charité Campus Buch, ECRC
HELIOS Clinics Berlin Buch,
Department for Cardiology and Nephrology
Schwanebecker Chaussee 50
13125 Berlin
Germany
Tel.: +49 30 040153536
jeanette.schulz-menger@charite.de


Jeanette Schulz-Menger


Edyta Blaszczyk

References

1 Ibanez B, et al. 2017 ESC Guidelines for the management of acute myocardial infarction in patients presenting with ST-segment elevation: The Task Force for the management of acute myocardial infarction in patients presenting with ST-segment elevation of the European Society of Cardiology (ESC). European Heart Journal. 2017.
2 Agewall S, et al. ESC working group position paper on myocardial infarction with non-obstructive coronary arteries. European Heart Journal. 2017; 38:143-53.
3 Aljaroudi WA, et al. Role of CMR imaging in risk stratification for sudden cardiac death. JACC Cardiovascular Imaging. 2013; 6:392-406.
4 Pasupathy S, Tavella R, and Beltrame JF. Myocardial Infarction With Nonobstructive Coronary Arteries (MINOCA): The Past, Present, and Future Management. Circulation. 2017; 135:1490-3.
5 Avanesov M, Munch J, Weinrich J, et al. Prediction of the estimated 5-year risk of sudden cardiac death and syncope or non-sustained ventricular tachycardia in patients with hypertrophic cardiomyopathy using late gadolinium enhancement and extracellular volume CMR. European radiology. 2017;27(12):5136-5145.

Cardiotoxicity in Cancer Therapy – the Role of Cardiovascular Magnetic Resonance

Christian P. Houbois[1,2]; Paaladinesh Thavendiranathan, MD SM[1,3,4]; Bernd J. Wintersperger, MD EBCR FAHA[1,2]

[1] Department of Medical Imaging, Peter Munk Cardiac Centre, University Health Network, Toronto, Canada
[2] Department of Medical Imaging, University of Toronto, Toronto, Canada
[3] Division of Cardiology, Peter Munk Cardiac Centre, University Health Network, Toronto, Canada
[4] Department of Medicine, University of Toronto, Toronto, Canada

Introduction

Cardiovascular magnetic resonance (CMR) imaging has become a mainstay in the assessment of various cardiac pathologies including ischemic and non-ischemic cardiomyopathies. Beyond the sole aspect of functional deterioration, CMR has convincingly demonstrated to provide further information on the underlying cause contributing sufficient information to narrow the differential diagnosis. Furthermore, insight into the myocardial composition may shed light into the risk prediction of certain diseases and may also allow monitoring of therapeutic interventions and their effects on the heart.

In recent years, the link between tumor therapies and cardiac disease has gained substantial attention and is currently focus of multiple ongoing large-scale studies. With the continuous improvement of survival rates of patients with various malignancies, potential detrimental effects on cardiac function and outcome including increased morbidity and mortality has become the center of such investigations. Outside study settings, major centers with large oncology and cardiac programs have started to establish Cardio-Oncology clinics, in order to help guide oncologists in their treatment planning in patients with pre-existing cardiac disease as well as taking care of patients with potential tumor therapy regimen related cardiovascular effects and potential development of heart failure (HF).

Tumor therapy and heart failure

Todays' therapy regimens in patients with malignant neoplasms may be based on surgical approaches, local or extended radiation therapy (RT) as well as systemic tumor therapies or a combination thereof. While surgical approaches and RT generally affect structures within the application field, systemic therapies may not only result in anti-tumor effects but may also affect otherwise normal body tissue, including the heart. Such negative effects of tumor-related therapy on the heart are generically referred to as cardiotoxicity. The known impact of anthracycline (AC) related tumor therapy possibly resulting in HF may often also be referred to as anthracycline induced heart failure (AIHF).

While modern personalized medicine approaches result in the continuous development of new anti-tumor drugs amongst different drug classes, AC still remain a mainstay of modern tumor therapy regimens. They are commonly used in treatment of breast malignancies, sarcomas and also hematologic malignancies. It is estimated that up to 60% of childhood cancer survivors have been exposed to AC therapy regimens and/or chest radiation [1; 2].

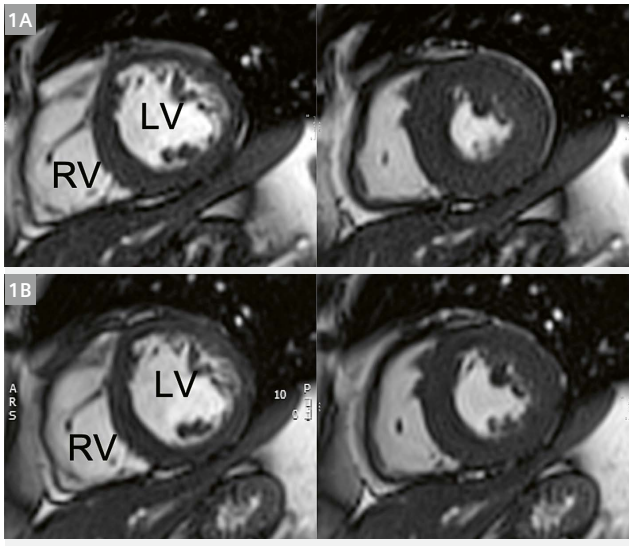

Figure 1:
Standard cine imaging in a patient with breast cancer **(1A)** prior to chemotherapy and **(1B)** one year after the end of anthracycline/trastuzumab combination therapy. Images demonstrate almost identical slice positioning (Cardiac Dot Engine) in diastole (left), but already visually a clear reduction in global ejection fraction is seen in systolie (right). The ejection fraction had dropped by ≥ 10% to < 50%.

LV = left ventricle; RV = right ventricle

Up to ~20% of patients undergoing AC based tumor therapy (with or without combination therapy) may experience AC related cardiotoxicity with the development of HF. The incidence generally increases with increasing cumulative AC dosing. Specifically designed studies employing short interval imaging (echocardiography) based monitoring of the ventricular function, the vast majority (up to 98%) of cardiotoxicity related HF developed either during the systemic cancer therapy or within one year after the end of therapy [3] (Fig. 1). Among patients experiencing such detrimental effects, the vast majority of patients will not entirely recover their cardiac function despite initiation of HF therapy [3]. The risk of cardiac events in this population is significantly increased and in case of confirmed AIHF, mortality may exceed 50% within two years.

Anthracyclines (e.g. doxorubicin, epirubicin) have been known from early use to potentially cause HF and still remain the drug class most commonly related to HF. However, also other drug classes may result in negative cardiovascular effects or may increase the risk of HF in combination with AC based therapy schemes. These classes include monoclonal anti-bodies (MAB) such as trastuzumab, tyrosine kinase inhibitors (TKI) as well as immune checkpoint inhibitors (ICI).

Meanwhile, guidelines have been developed helping to identify patient populations who are specifically at risk for cardiotoxicity related HF [4]. In general, the risk is specifically depending on the dosage of AC therapy, but also the amount of potentially applied additional radiation, potential cardiovascular risk factors as well as the combination of certain drug classes (e.g. anthracycline-trastuzumab combination therapy) [4].

Of specific interest is also the class of aforementioned ICI's, a group of agents that has generally demonstrated lower rates of cardiotoxicity, but that may specifically cause autoimmune myocarditis in rare instances resulting in high complication rates [5].

Cardiovascular magnetic resonance and cardiotoxicity

The breadth of techniques available in CMR for assessment of cardiac function, myocardial deformation and myocardial tissue characterization makes it a potentially ideal tool for assessment and monitoring of patients with increased risk of developing cancer therapy related cardiotoxicity.

Functional cardiac imaging

Today's definitions of cardiotoxicity are almost exclusively based on the assessment of the left ventricular (LV) ejection fraction (EF). As such, the known high accuracy and precision of CMR in the assessment of cardiac volume and function is perfectly suited to guide clinicians according to current definitions of cardiotoxicity [6]. With little variation, published criteria of cardiotoxicity follow a change in LVEF with main cut-offs at a drop of ≥ 10% to under 50% or 55%/53% respectively (Fig. 1) [7–9]. More subtle changes in LVEF (≥ 5%) should be considered as possibly related to cardiotoxicity in patients with symptoms of heart failure (HF) [8]. However, it is important to keep in mind that such thresholds are generally based on echocardiography or multigated acquisition (MUGA) radionuclide ventriculography, modalities that generally suffer from a higher inter-scan and inter-observer variability. Although there is no separate cut-off criterion based on CMR, recent study data suggests that MUGA results may potentially result in misclassification of patients [10].

In any of the above LVEF based definitions of cardiotoxicity, proper baseline assessment and follow scans are required; single time assessment of the cardiac function would not allow adequate judgement. In addition to standard imaging approaches, CMR may play an increasingly important role in the monitoring of such patients. Various clinical experiences report cases where echocardiography based functional assessment would have missed a significant drop in LVEF.

However, from decades of imaging experience it is known that LVEF changes may only occur as a delayed relation to local changes. Therefore, assessment of myocardial deformation may provide a more sensitive and earlier insight into myocardial changes. In the field of echocardiography, the application of speckle tracking echocardiography (STE) has pushed the use of strain imaging towards clinical use including assessment of cardiotoxicity. CMR offers various techniques for myocardial deformation imaging including myocardial tagging, sensitivity encoding (SENC) and displacement encoding with stimulated echoes (DENSE). However, such techniques have never been established on a larger scale in clinical routine CMR.

Most recently, developments of techniques that allow assessment of myocardial strain in routinely acquired cine balanced steady state free precession (bSSFP) data sets have opened a whole new avenue of myocardial deformation assessment. The different available techniques rely either on feature tracking algorithms or employ motion correction techniques for calculation of deformation in cine bSSFP [11–15]. Especially, prototype deformation map-based techniques such as TrufiStrain[1] (Siemens Medical Imaging Technologies, Princeton, US) demonstrated promising and highly

[1] *WIP, the product is currently under development and is not for sale in the US and in other countries. Its future availability cannot be ensured.*

reproducible results compared to accepted standard of reference such as myocardial tagging (Figures 2–4) [12; 14]. In the application of cardiotoxicity evaluation, CMR based strain has also demonstrated great promise aiming at early detection of changes.

Tissue characterization

Qualitative tissue characterization techniques such as T2-weighted imaging or Late Gadolinium Enhancement (LGE) imaging have long played a role in the assessment of various cardiomyopathies and inflammatory changes such as myocarditis [16, 17]. However, the use of LGE imaging in assessment of cardiotoxicity appears limited. As an exception, LGE may play a role in assessment of possible autoimmune myocarditis/pericarditis which may occur during ICI therapy and is considered a bad prognostic marker (Fig. 5).

As a potential new marker of cardiotoxicity related tissue level changes, cardiac relaxometry techniques such as T1 mapping, T2 mapping as well as derived markers such as extracellular volume fraction (ECV) have been proposed and evaluated in various experimental and clinical studies predominately focused on the effects of anthracycline therapy.

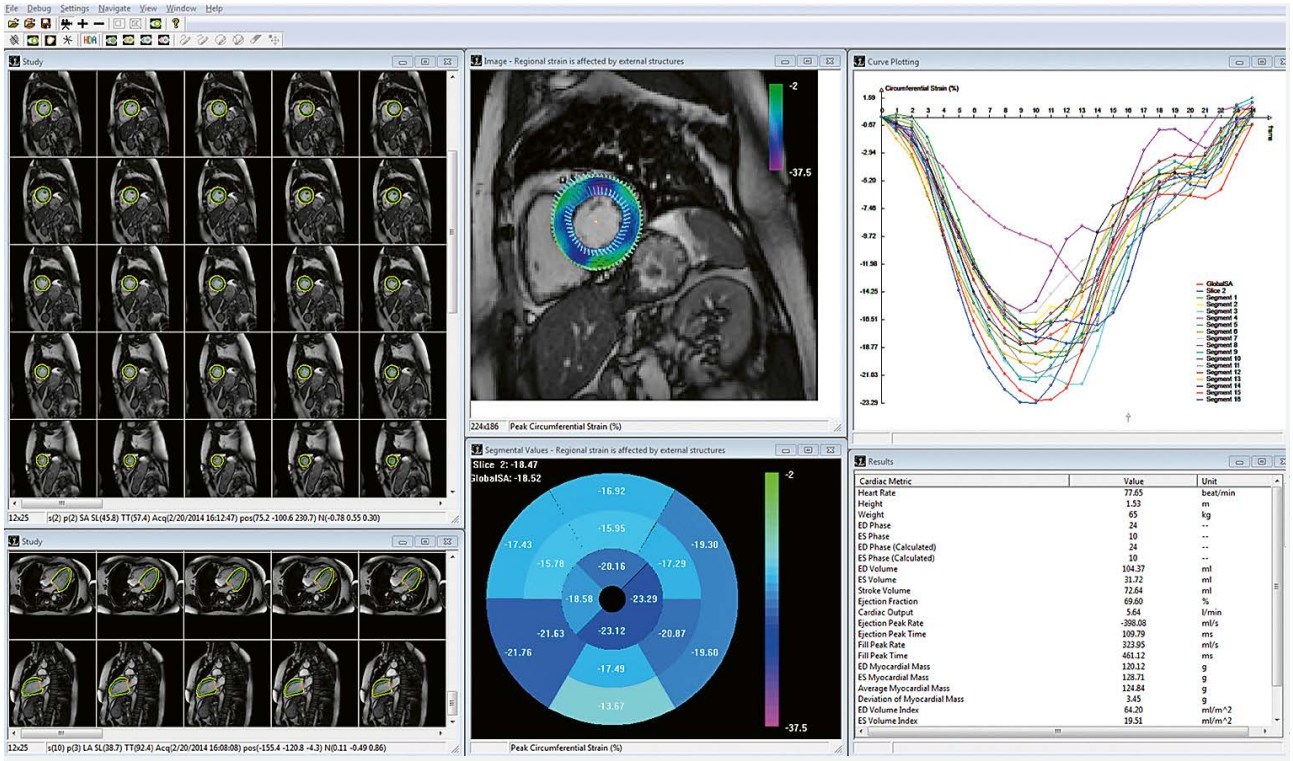

Figure 2:
Standard screen overview of TrufiStrain[1], a prototype software for cine derived strain analysis. The left part of the layout demonstrates the fully automated (short axis) and semiautomated (long axis) segmentation of the endo- and epicardial contours. The center part highlights a visual overlay of strain data onto cine data as well as a bullseye plot of AHA segment strain results. On the right, a visual display of the strain curves (circumferential in this case) for all 16 AHA segments as well as the entire slice with additional results of automated functional analysis at the bottom.

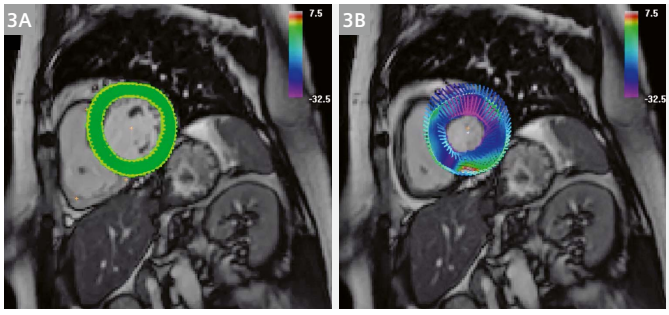

Figure 3:
Single short axis slice in a healthy volunteer in **(3A)** diastole and **(3B)** systole with time point related strain result overlay; the colored lines on the systolic display visualize the direction and magnitude of endo- as well as epicardial motion from diastole to systole.

In animal studies, the repeated application of anthracycline doses lead to a continuous increase in native T1 values over the course of 12–14 weeks while other studies have demonstrated that T2 values are increased in the early phase (~4–6 weeks) suggesting myocardial edema [18, 19]. However, the later study also demonstrated that despite elevated T2 values in early stages, ECV was not elevated until later stages. A possible explanation of elevated T2 and normal ECV might be the occurrence of intracellular edema.

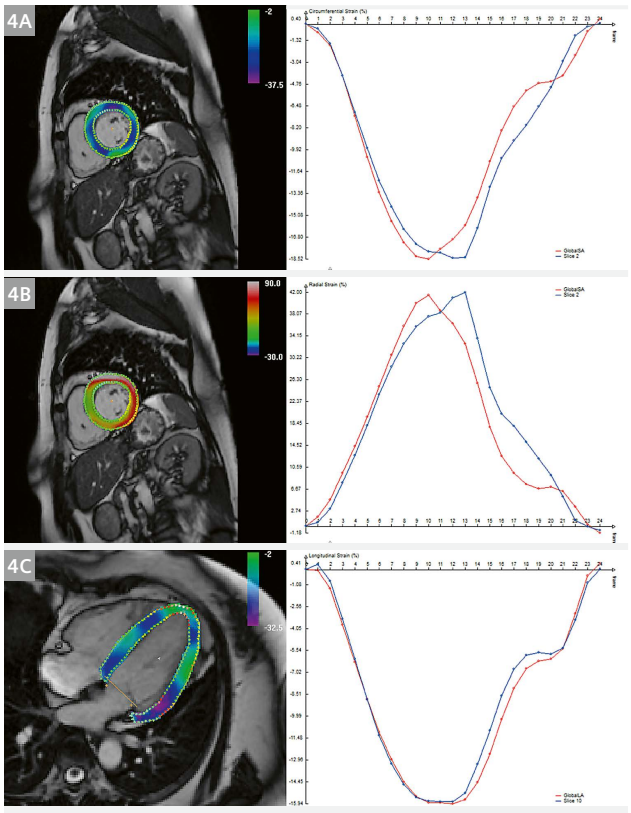

Figure 4:
Demonstration of three major directions/orientations of myocardial strains typically evaluated; **(4A)** circumferential strain, **(4B)** radial strain and **(4C)** longitudinal strain. As strain is a measure of length changes in relation to an applied force, the typical shortening in evaluation on circumferential and longitudinal strain result in negative strain values while the thickening during systole results in positive values for radial strain.

Changes in myocardial T1 as well as ECV values have also been demonstrated in patient studies. As in many other cardiomyopathies, pre-contrast T1 values as well as ECV increase after chemotherapy, likely related to development of interstitial fibrosis [20]. However, hyperacute reactions within the myocardium may result in an initial T1 value decrease possible indicating worse outcome [21]. Currently, there is still limited data from prospective longitudinal studies available to clearly describe potential differences in quantitative cardiac relaxometry in patients with and without development of functional deterioration after chemotherapy. Similar to functional analysis, likely sequential longitudinal imaging, including pre-therapy assessment of T1 and T2 data, is required to identify and differentiate true tissue changes from imaging related variability. A possibly even more promising use of cardiac relaxometry techniques may again relate to patients under ICI therapy with possible autoimmune myocarditis changes (Fig. 5). Similar to recent recommendations regarding the diagnosis of myocarditis in general, changes in quantitative tissue markers may help earlier and more accurate diagnosis [22].

Conclusion

While the playing field of potentially cardiotoxic tumor therapy generally hasn't substantially changed, decades of study results have helped to better understand risk factors and relationships between tumor therapy and cardiac failure. Furthermore, there is a much-increased awareness of the potential interaction between tumor

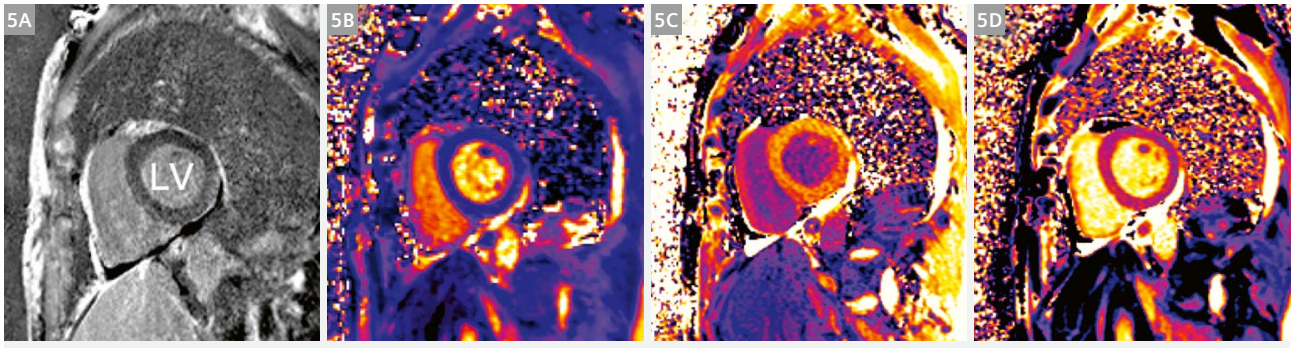

Figure 5:
Patient undergoing immune checkpoint inhibitor (ICI) cancer therapy with troponin elevation and suspicion of immune myocarditis. While **(5A)** LGE imaging possible demonstrates very faint diffuse enhancement, cardiac relaxometry with T1 and T2-mapping (1.5T) provides further information. **(5B)** T2 mapping reveals a T2 time of 55 ms while **(5C)** pre-contrast T1 values were 1184 ms and **(5D)** post-contrast T1 values 519 ms (0.15 mmol/kg Gadobutrol). Based on the patient's hematocrit the ECV is calculated to 38%.

therapy and heart failure resulting in the new subspecialty of 'Cardio-Oncology'. While imaging has long played a role in cancer patients undergoing chemotherapy, CMR is rapidly entering the field and is more frequently being employed. The accuracy and precision of CMR functional assessment proves beneficial in early identification of functional deterioration. Added information might be gathered from cine CMR based strain analysis and quantitative myocardial tissue markers (T1/T2/ECV mapping). However, the timing and specific application of CMR during the course of cancer therapy, especially in patients at risk, has yet to be determined. For a better understanding of that role, additional data on the general test-retest variability of such quantitative markers is still required. Furthermore, society guidelines and definitions of cardiotoxicity would need to further extend beyond the sole criteria of cardiac function.

References:

1 Smith LA, Cornelius VR, Plummer CJ et al. (2010) Cardiotoxicity of anthracycline agents for the treatment of cancer: systematic review and meta-analysis of randomised controlled trials. BMC Cancer 10:337.
2 Armenian SH, Hudson MM, Mulder RL et al. (2015) Recommendations for cardiomyopathy surveillance for survivors of childhood cancer: a report from the International Late Effects of Childhood Cancer Guideline Harmonization Group. Lancet Oncol 16:e123-136.
3 Cardinale D, Colombo A, Bacchiani G et al. (2015) Early detection of anthracycline cardiotoxicity and improvement with heart failure therapy. Circulation 131:1981-1988
4 Armenian SH, Lacchetti C, Barac A et al (2017) Prevention and Monitoring of Cardiac Dysfunction in Survivors of Adult Cancers: American Society of Clinical Oncology Clinical Practice Guideline. J Clin Oncol 35:893-911.
5 Escudier M, Cautela J, Malissen N et al. (2017) Clinical Features, Management, and Outcomes of Immune Checkpoint Inhibitor-Related Cardiotoxicity. Circulation 136:2085-2087.
6 Grothues F, Smith GC, Moon JC et al. (2002) Comparison of interstudy reproducibility of cardiovascular magnetic resonance with two-dimensional echocardiography in normal subjects and in patients with heart failure or left ventricular hypertrophy. Am J Cardiol 90:29-34.
7 Schwartz RG, McKenzie WB, Alexander J et al. (1987) Congestive heart failure and left ventricular dysfunction complicating doxorubicin therapy. Seven-year experience using serial radionuclide angiocardiography. Am J Med 82:1109-1118.
8 Seidman A, Hudis C, Pierri MK et al. (2002) Cardiac dysfunction in the trastuzumab clinical trials experience. J Clin Oncol 20:1215-1221.
9 Plana JC, Galderisi M, Barac A et al. (2014) Expert consensus for multimodality imaging evaluation of adult patients during and after cancer therapy: a report from the American Society of Echocardiography and the European Association of Cardiovascular Imaging. J Am Soc Echocardiogr 27:911-939.
10 Huang H, Nijjar PS, Misialek JR et al. (2017) Accuracy of left ventricular ejection fraction by contemporary multiple gated acquisition scanning in patients with cancer: comparison with cardiovascular magnetic resonance. J Cardiovasc Magn Reson 19:34.
11 Lamacie MM, Thavendiranathan P, Hanneman K et al. (2017) Quantification of global myocardial function by cine MRI deformable registration-based analysis: Comparison with MR feature tracking and speckle-tracking echocardiography. Eur Radiol 27:1404-1415.
12 Lamacie MM, Houbois CP, Greiser A, Jolly MP, Thavendiranathan P, Wintersperger BJ (2019) Quantification of myocardial deformation by deformable registration-based analysis of cine MRI: Validation with tagged CMR. Eur Radiol. DOI: 10.1007/s00330-019-06019-9.
13 Keller EJ, Fang S, Lin K et al (2017) The consistency of myocardial strain derived from heart deformation analysis. Int J Cardiovasc Imaging 33:1169-1177
14 Jolly MP, Jordan JH, Melendez GC, McNeal GR, D'Agostino RB, Jr., Hundley WG (2017) Automated assessments of circumferential strain from cine CMR correlate with LVEF declines in cancer patients early after receipt of cardio-toxic chemotherapy. J Cardiovasc Magn Reson 19:59.
15 Barreiro-Perez M, Curione D, Symons R, Claus P, Voigt JU, Bogaert J (2018) Left ventricular global myocardial strain assessment comparing the reproducibility of four commercially available CMR-feature tracking algorithms. Eur Radiol. 10.1007/s00330-018-5538-4.
16 Cummings KW, Bhalla S, Javidan-Nejad C, Bierhals AJ, Gutierrez FR, Woodard PK (2009) A pattern-based approach to assessment of delayed enhancement in nonischemic cardiomyopathy at MR imaging. Radiographics 29:89-103.
17 Friedrich MG, Sechtem U, Schulz-Menger J et al. (2009) Cardiovascular magnetic resonance in myocarditis: A JACC White Paper. J Am Coll Cardiol 53:1475-1487.
18 Hong YJ, Park HS, Park JK et al. (2017) Early Detection and Serial Monitoring of Anthracycline-Induced Cardiotoxicity Using T1-mapping Cardiac Magnetic Resonance Imaging: An Animal Study. Sci Rep 7:2663.
19 Farhad H, Staziaki PV, Addison D et al. (2016) Characterization of the Changes in Cardiac Structure and Function in Mice Treated With Anthracyclines Using Serial Cardiac Magnetic Resonance Imaging. Circulation Cardiovascular imaging 9:e003584.
20 Jordan JH, Vasu S, Morgan TM et al. (2016) Anthracycline-Associated T1 Mapping Characteristics Are Elevated Independent of the Presence of Cardiovascular Comorbidities in Cancer Survivors. Circulation Cardiovascular imaging 9
21 Muehlberg F, Funk S, Zange L et al. (2018) Native myocardial T1 time can predict development of subsequent anthracycline-induced cardiomyopathy. ESC Heart Fail. 10.1002/ehf2.12277.
22 Ferreira VM, Schulz-Menger J, Holmvang G et al. (2018) Cardiovascular Magnetic Resonance in Nonischemic Myocardial Inflammation: Expert Recommendations. J Am Coll Cardiol 72:3158-3176.

Contact

Bernd J. Wintersperger, MD EBCR FAHA
Department of Medical Imaging
Toronto General Hospital, 1 PMB-273
585 University Avenue
Toronto, Ontario, M5G 2N2
Canada
Tel.: 416-340-4800 ex. 8593
Bernd.Wintersperger@uhn.ca


Bernd Wintersperger


Christian Houbois


P. Thavendiranathan

CMR and Cardiotoxicity. A Case-based Overview

Fabian Muehlberg, M.D.; Jeanette Schulz-Menger, M.D.

Working Group Cardiac MRI, Experimental and Clinical Research Center, a cooperation between the Charité Medical Faculty, the Max-Delbrück Center for Molecular Medicine, and the Department of Cardiology and Nephrology, HELIOS Clinic Berlin Buch, Germany

A 55-year-old woman and a 51-year-old man were diagnosed with non-metastatic soft tissue sarcoma of the lower limb, underwent surgical resection, and received an adjuvant course of anthracycline-based chemotherapy. Both patients have a long-standing diagnosis of well-controlled hypertension, but have no other cardiovascular comorbidity. The baseline left ventricular ejection fraction (LVEF) in both individuals was well above 55% before chemotherapy. After following the exact same treatment protocol comprising 450 mg/m^2 doxorubicin over a period of five months both patients are considered cancer free and can hope for a normal life expectancy. However, after completing chemotherapy, the 55-year-old female reported clinical signs of heart failure and showed a drop of LVEF to 45%, while the 51-year-old male maintained a normal LVEF and showed no heart failure symptoms. Representative SSFP cine images at end-systole and end-diastole are shown in Figure 1.

These two patients illustrate a growing issue in cardiology and oncology, namely therapy-associated cardiotoxicity. As the outcomes of most cancer patients have significantly improved over recent decades, the number of cancer survivors has dramatically increased, which has led to the long-term side effects of therapy growing in importance [1]. There are a number of chemotherapeutic agents with known cardiotoxic side effects. The most important of these in terms of patient numbers are anthracyclines and trastuzumab [2].

Anthracyclines are the mainstay of treatment for many malignancies. Approximately one third of all breast cancer patients [3], two thirds of lymphoma patients, and almost all soft tissue sarcoma patients receive anthracyclines during the course of their treatment [4].

Heart failure due to anthracyclines has serious prognostic implications as it can lead to mortality rates that are worse than with many malignancies [5].

Multimodality imaging plays an important role in risk assessment for early detection of chemotherapy-related cardiotoxicity, with CMR playing an increasingly important role. In 2016, the European Society of Cardiology (ESC) published a position paper highlighting the importance of CMR in the diagnostic approach to cardiotoxicity [6]. While echocardiography has maintained its role in screening and basic diagnostics, CMR has two unique features with regard to the assessment of early cardiotoxic side effects that increase its importance. First, SSFP cine imaging remains the gold standard for the evaluation of small changes in LVEF and has been shown to be superior to echocardiography in terms of accuracy and reproducibility [7]. Since the early detection of heart failure under anthracycline or trastuzumab therapy is a key factor in successful treatment and reversibility rates, CMR has an advantage over alternative techniques in this regard. Second, as well as a purely functional assessment, CMR also has tissue differentiation capabilities, which help to determine the cause and stage of the underlying cardiac damage.

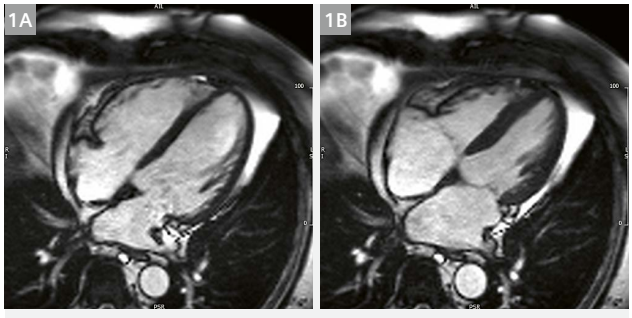

55-year-old woman after chemotherapy (LVEF 45%)

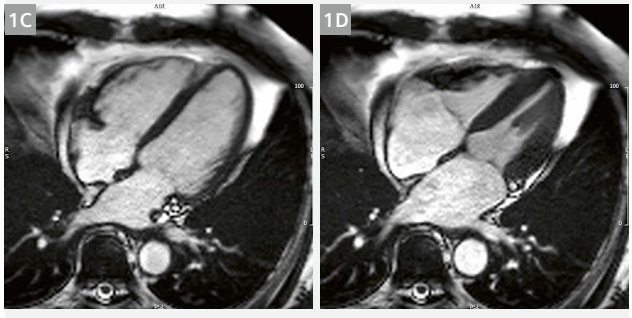

51-year-old man after chemotherapy (LVEF 65%)

Figure 1:
Representative SSFP cine images of end-diastole and end-systole for two sample patients with and without anthracycline-induced systolic heart failure.

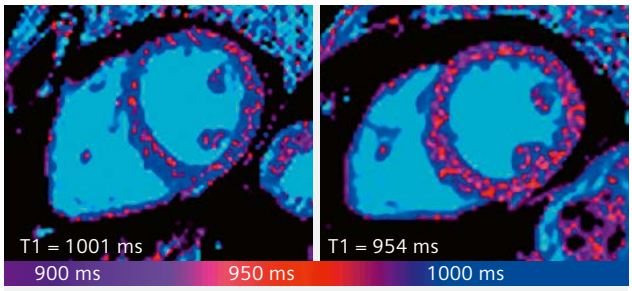

Figure 2:
Short-axis T1 MOLLI maps of the same individual before and 48 hours after administration of the first dose of anthracyclines.

Myocardial T1 and T2 mapping techniques play a pivotal role in detecting myocardial inflammation and edema as signs of acute myocardial damage that may be attributable to chemotherapy-related cardiotoxicity or to acute myocarditis in immunocompromised cancer patients – two pathologic entities with different treatment regimens.

Another increasingly important tool for tissue differentiation in these patients is the evaluation of diffuse fibrosis through extracellular volume (ECV) quantification. Several studies have shown that anthracycline therapy leads to diffuse myocardial fibrosis years after treatment, causing chronic heart failure and severe cardiovascular events in long-term cancer survivors [8, 9].

All the aforementioned capabilities of CMR in the diagnostic approach to cardiotoxicity have a common goal: To detect myocardial injury as early as possible in order to rapidly initiate therapeutic countermeasures. While early detection of cardiotoxicity remains the main strategy, there are newer studies showing the prospective benefit of CMR in the ex ante identification of patients at highest risk for the development of chemotherapy-related heart failure. In a pilot study, our working group reported that an early change of native myocardial T1 time after the first dose of anthracyclines could predict the development of systolic heart failure at the end of treatment [10]. This was also the case in our two patients – while the 55-year-old female with anthracycline-induced cardiomyopathy showed an early drop in native T1 time (see Fig. 2), the 51-year-old male with no development of cardiomyopathy maintained normal myocardial T1 values.

Further studies are underway to assess the predictive role of CMR for other agents such as trastuzumab or VEGF inhibitors. We are confident that CMR will be an increasingly important diagnostic tool in cardio-oncology and has the potential to shift the cardiotoxicity strategy from “early damage detection” to “prospective damage prevention” in the future.

References

1 Coleman MP, et al. Cancer survival in Australia, Canada, Denmark, Norway, Sweden, and the UK, 1995-2007 (the International Cancer Benchmarking Partnership): an analysis of population-based cancer registry data. Lancet. 2011; 377(9760):127-138.
2 Plana JC, et al. Multi-Modality Imaging in the Assessment of Cardiovascular Toxicity in the Cancer Patient. JACC Cardiovascular Imaging. 2018; 11(8):1173-1186.
3 Giordano SH, et al. Decline in the use of anthracyclines for breast cancer. Journal of clinical oncology : official journal of the American Society of Clinical Oncology. 2012; 30(18):2232-2239.
4 Nabhan C, et al. Disease characteristics, treatment patterns, prognosis, outcomes and lymphoma-related mortality in elderly follicular lymphoma in the United States. British Journal of Hhaematology. 2015; 170(1):85-95.
5 Alvarez JA and Russell RR. Cardio-oncology: the Nuclear Option. Current Cardiology Reports. 2017; 19(4):31.
6 Zamorano JL, et al. 2016 ESC Position Paper on cancer treatments and cardiovascular toxicity developed under the auspices of the ESC Committee for Practice Guidelines: The Task Force for cancer treatments and cardiovascular toxicity of the European Society of Cardiology (ESC). European Heart Journal 2016; 37(36):2768-2801.
7 Ylanen K, Eerola A, Vettenranta K, and Poutanen T. Three-dimensional echocardiography and cardiac magnetic resonance imaging in the screening of long-term survivors of childhood cancer after cardiotoxic therapy. The American Journal of Cardiology. 2014; 113(11):1886-1892.
8 Neilan TG, et al. Myocardial extracellular volume by cardiac magnetic resonance imaging in patients treated with anthracycline-based chemotherapy. The American Journal of Cardiology. 2013; 111(5):717-722.
9 Jordan JH, et al. Anthracycline-Associated T1 Mapping Characteristics Are Elevated Independent of the Presence of Cardiovascular Comorbidities in Cancer Survivors. Circulation Cardiovascular Imaging. 2016; 9(8).
10 Muehlberg F, et al. Native myocardial T1 time can predict development of subsequent anthracycline-induced cardiomyopathy. ESC Heart Failure. 2018; 5(4):620-629.

Contact

Professor Jeanette Schulz-Menger, M.D.
University Medicine Berlin
Charité Campus Buch, ECRC
HELIOS Clinics Berlin Buch,
Department for Cardiology and Nephrology
Schwanebecker Chaussee 50
13125 Berlin
Germany
Tel.: +49 30 040153536
jeanette.schulz-menger@charite.de


Jeanette Schulz-Menger


Fabian Mühlberg

Unusual Atrial Myxoma with Neovascularization Associated with Fistula to Right Atrium

Pairoj Charanukulchai; Kanokvalee Ponkanist

Division of Cardiovascular Medicine, Department of Medicine, Department of Radiology, Faculty of Medicine, Chulalongkorn University, Cardiac Center, King Chulalongkorn Memorial Hospital, Bangkok, Thailand

An 80-year-old woman was evaluated for the first-detected atrial fibrillation found during a regular health check. Transthoracic echocardiography revealed a 30 x 40 mm, pedunculated, inhomogeneous left atrial (LA) mass attached to the interatrial septum (Fig. 1, asterisk) with indeterminate blood flow inside. Short-axis T2-weighted MRI with fat suppression (acquired on a MAGNETOM Skyra 3T) showed the mass attached to the fossa ovalis with strongly hyperintense signal (Fig. 2), and isointense to myocardium on noncontrast T1-weighted images without (Fig. 3A) and with fat suppression (Fig. 3B). Perfusion imaging nicely demonstrated the rapid contrast uptake via the cluster of tortuous vascular channels within the tumor (Fig. 4, asterisk).

A fistula to the right atrium (RA) was suspected due to the presence of contrast leakage from the tumor into the RA cavity. Preoperative coronary angiography (Fig. 5) confirmed the large, tortuous feeding artery to the mass arising from the left circumflex artery with fistula to RA (calculated pulmonary-systemic shunt ratio 1.2:1).

The patient successfully underwent elective tumor removal with fistula closure. A gross specimen of the bisected tumor showed a large, well-formed intratumoral vessel measuring 8 mm in diameter (Fig. 6, arrow) with a diffuse area of internal hemorrhage. Histology confirmed the diagnosis of myxoma with abundant delicate blood vessel formation.

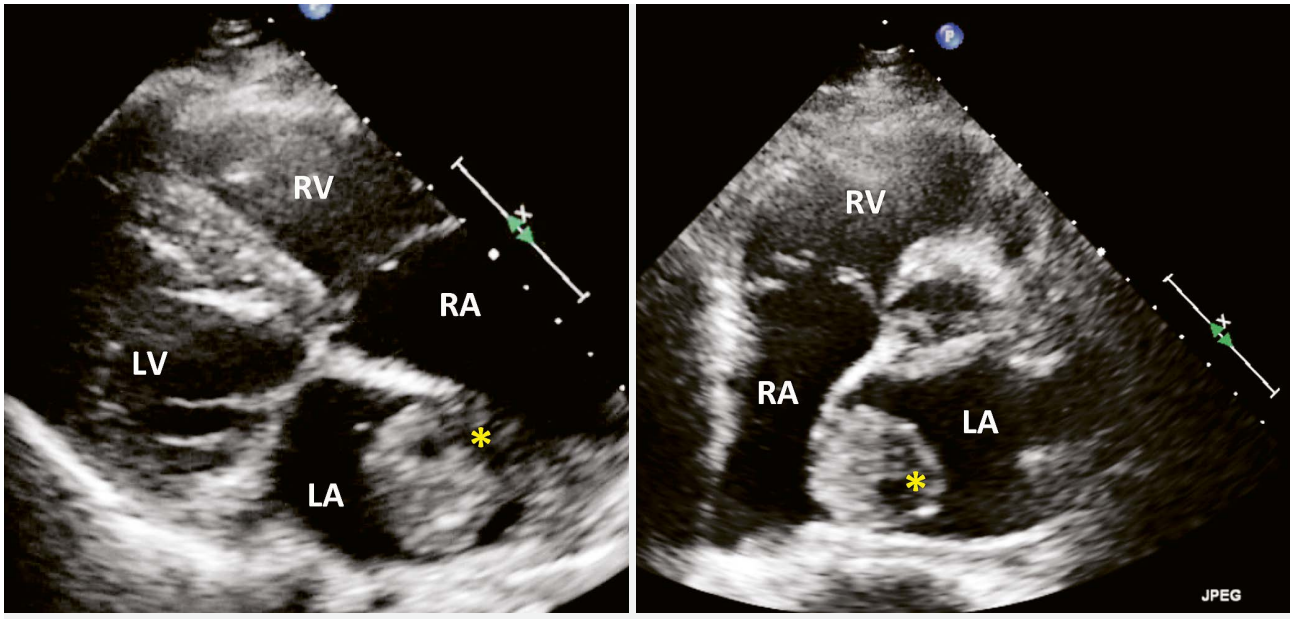

Figure 1:
Transthoracic echocardiography
Reprinted with permission [1].

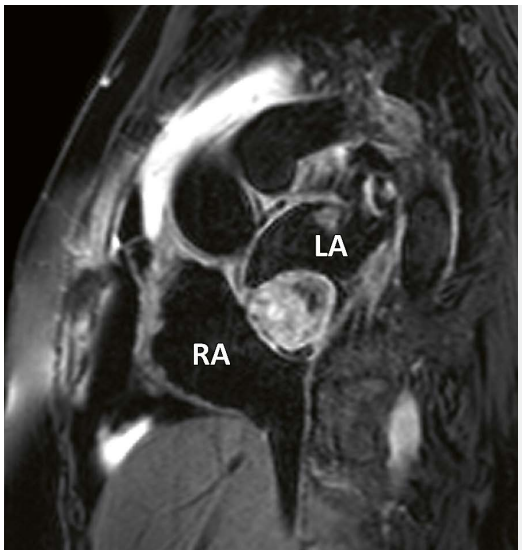

Figure 2:
Short-axis T2-weighted TSE with fat suppression;
Imaging parameters:
FOV 276 x 340 mm, slice thickness 5 mm,
TR 1860 ms, TE 62 ms, matrix 166 x 256,
pixel resolution of 1.66 x 1.33 mm, TA 11.2 s.

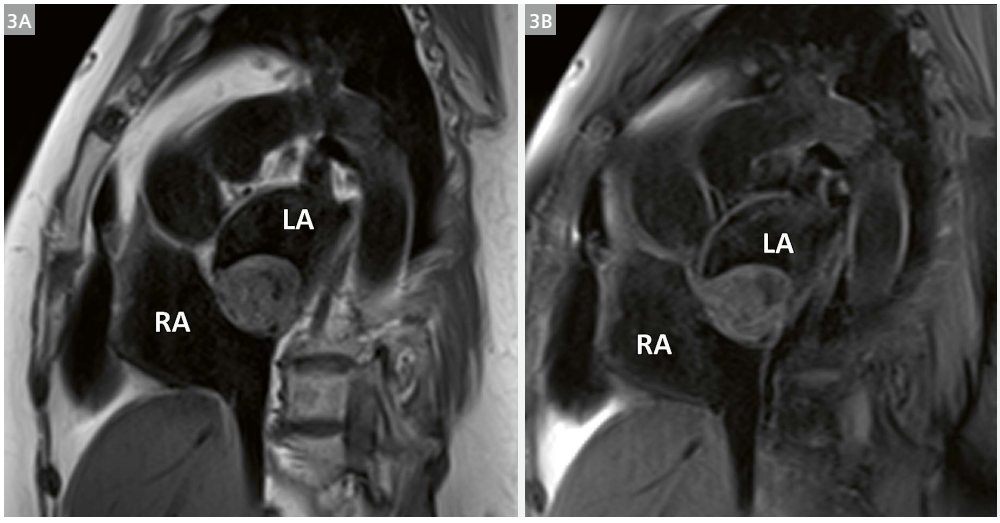

Figure 3A and 3B:
Short-axis T1-weighted TSE;
Imaging parameters:
FOV 276 x 340 mm,
slice thickness 5 mm,
TR 1320 ms, TE 29 ms,
matrix 188 x 256,
pixel resolution of 1.47 x 1.33 mm, TA 13.2 s.
Reprinted with permission [1].

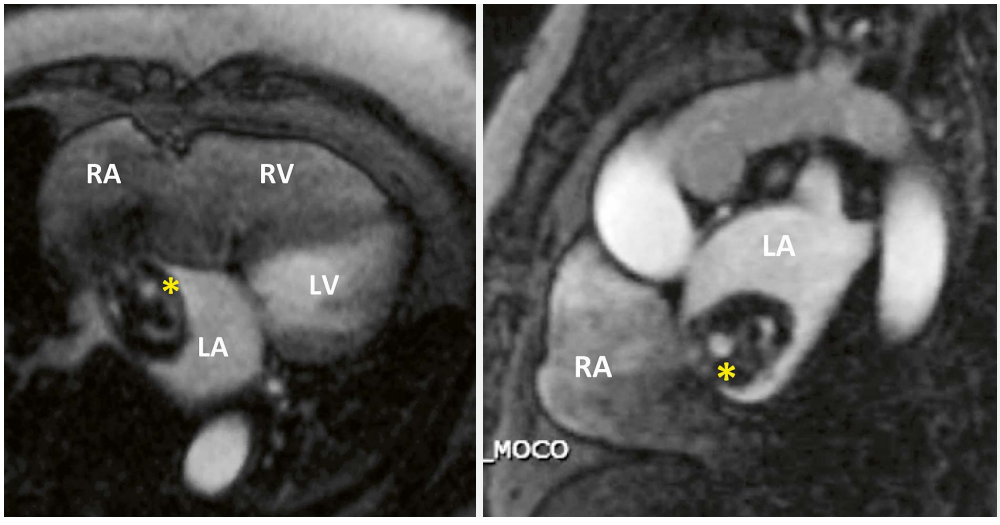

Figure 4:
Perfusion-weighted imaging (tfl2d) dynamic scan with motion correction in 4-chamber view;
Imaging parameters:
FOV 300 x 360 mm,
slice thickness 10 mm,
TR 164.8 ms, TE 1.1 ms,
TI 100 ms, matrix 146 x 256, pixel resolution of 2.05 x 1.4 mm.

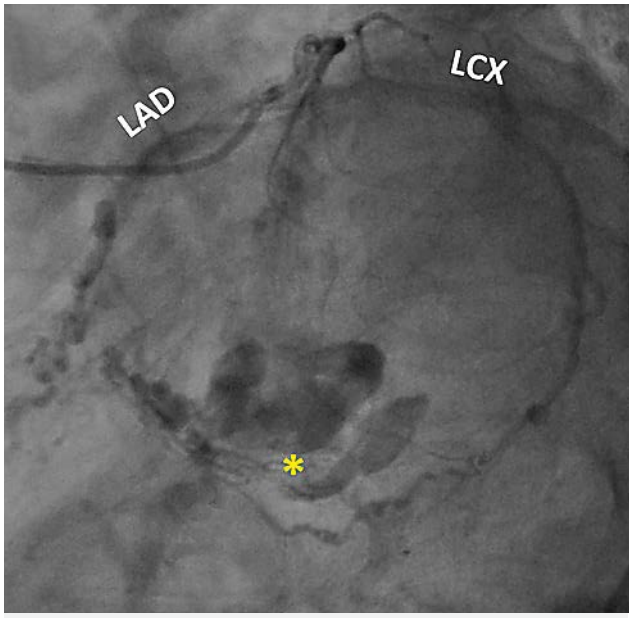

Figure 5:
Angiography
Reprinted with permission [1].

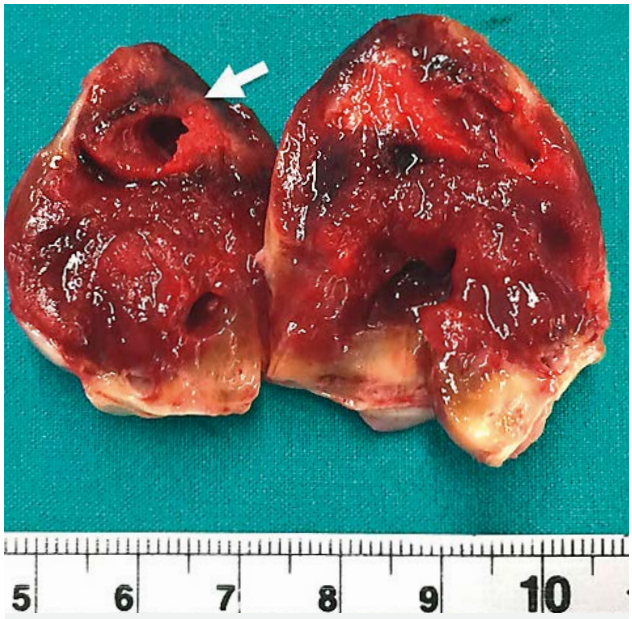

Figure 6:
Bisected tumor

Conclusion

This is the first case report of hypervascularized myxoma associated with fistula to RA that highlights the role of multimodality imaging in preoperative assessment. A high-performance CMR scanner can provide the high-resolution perfusion images, necessary for contemplating the surgical technique.

Contact

Pairoj Charanukulchai M.D., MSc
Division of Cardiovascular Medicine,
Department of Medicine, Faculty of Medicine
Chulalongkorn University, Cardiac Center,
King Chulalongkorn Memorial Hospital
Bangkok
Thailand
pairoj.md@gmail.com

Reference:

1 Huntrakul A, Numchaisiri J, Buddhari W, Chattranukulchai P. Unusual atrial myxoma with neovascularization associated with fistula to right atrium. Eur Heart J. 2017 Oct 14;38(39):2971.

Clinical Usefulness of 4D Flow in Adult Cardiovascular MRI

Stephanie Funk, M.D.; Aylin Demir; Jeanette Schulz-Menger, M.D.

Working Group Cardiac MRI, Experimental and Clinical Research Center, a cooperation between the Charité Medical Faculty, the Max-Delbrück Center for Molecular Medicine, and the Department of Cardiology and Nephrology, HELIOS Clinic Berlin Buch, Germany

4D Flow[1] is an upcoming tool for the evaluation of hemodynamics in cardiovascular magnetic resonance (CMR). Not only does it visualize flow in three dimensions and over time, it also allows for the quantification of additional parameters.

In routinely used 2D flow measurement, the blood flow is typically encoded in one direction, in one slice perpendicular to the flow. However, in cases with a complex flow pattern and changes in flow direction during the cardiac cycle, the positioning is challenging. This can lead to an underestimation of peak velocities and flow volumes [1].

Faster 4D Flow sequences[1] have enabled a broader application. In congenital heart disease, 4D Flow is used for the visual assessment of intracardiac shunts and anatomy [1–3].

In adult heart disease, several studies have shown the benefit of applying 4D Flow in patients with aortic valve or aortic pathologies [4–8]. Not only can 4D Flow help to accurately visualize and quantify the flow volume, it can also provide additional information for the evaluation of these pathologies, such as the wall shear stress (WSS) in the aorta.

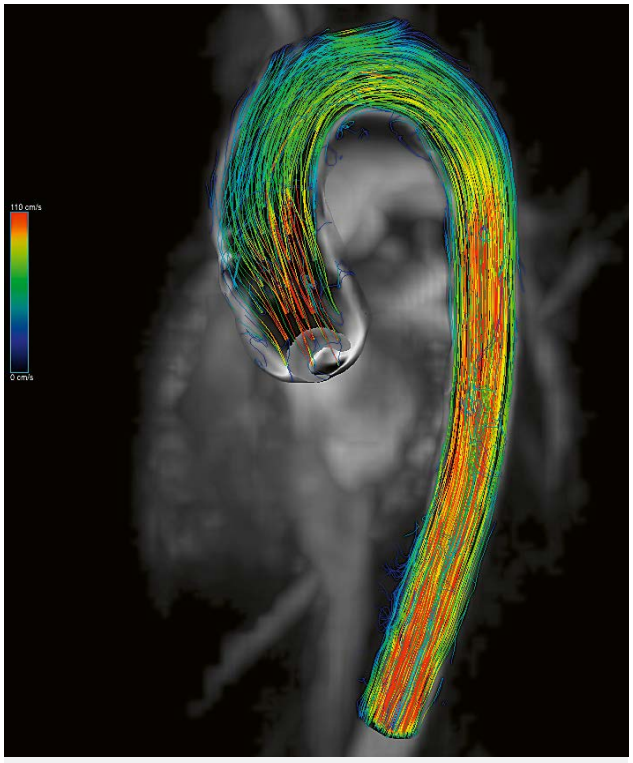

Figure 1:
Hemodynamics in a healthy volunteer. Streamlines show a regular flow.

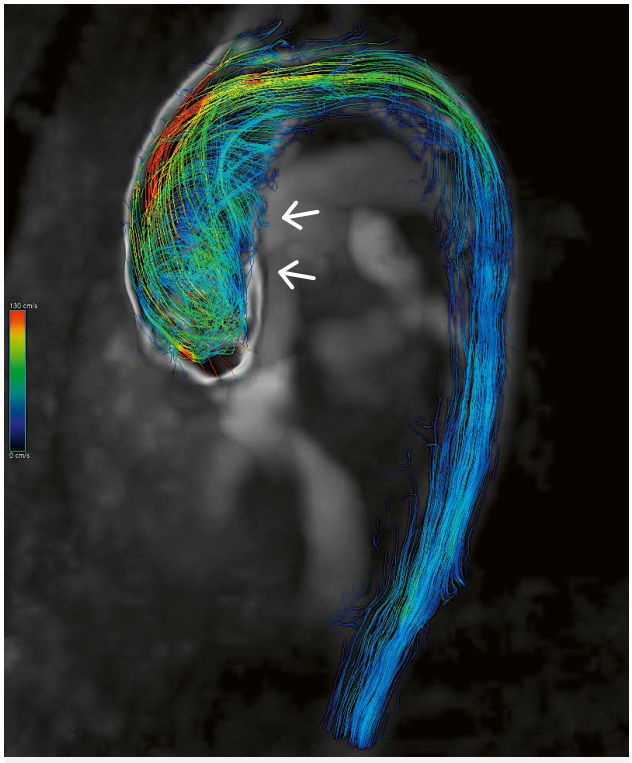

Figure 2:
Abnormal flow pattern in a patient with severe aortic stenosis showing increased helical and vortical flow pattern in the ascending aorta (white arrows).

[1] *WIP, the product is currently under development and is not for sale in the US and in other countries. Its future availability cannot be ensured.*

In aortic stenosis, abnormal flow patterns and localized increases in WSS were observed and these changes increased in line with the severity of the stenosis [5, 7]. Flow patterns changed from normal straight streamlines (for an example, see Fig. 1) to abnormal helical and vertical turbulences (for streamlines of a sample patient with aortic stenosis, see Fig. 2) [5, 7].

The highest increase of WSS could be seen in the mid-ascending aorta on the right side of the aorta (for WSS of a sample patient with aortic stenosis, see Fig. 3) [7]. In this area, aortic dilatation resulting in aortic aneurysms or even dissection are known to be more likely in patients with aortic stenosis. WSS might be an early indicator of this process.

These changes are not unique to patients with aortic stenosis. Patients with bicuspid aortic valves also experience them, even without an additional stenosis [4, 6].

Visualization and also quantification of these parameters has been made easier by several commercially available post-processing software tools for the evaluation of 4D Flow.

Flow volumes, peak velocity, and additional parameters such as WSS can be quantified by placing 2D planes at any location in the vessel (see Fig. 4, images generated with cvi42 prototype version 5.9.2[2] (Circle Cardiovascular Imaging, Calgary, Canada)). A significant advantage of 2D Flow is the possibility of creating planes after image acquisition of the whole aorta. Planes can therefore be freely set anywhere in the aorta and adjusted to the flow jet or in the direction of the vessel. Planes should be created after visual assessment of the aorta. This way, the area of interest, for example the area of the highest WSS, can be assessed visually before creating a plane for quantification.

This possibility of visualizing flow in the entire vessel as well as the option of setting planes anywhere may also help in cases with incongruent 2D flow results.

Usually in CMR, the degree of aortic insufficiency is determined by the regurgitation fraction of 2D through-plane flow imaging [9]. In some cases, however, the regurgitation fraction does not fit other indirect signs of an often more severe regurgitation. At our site, we recently treated a patient with an aortic regurgitation where 2D flow only measured a mild regurgitation fraction, but the severely dilated left ventricle indicated a more severe regurgitation. As the patient also had a dilated ascending aorta, we suspected that an abnormal flow pattern was the cause of the mismatch.

We therefore performed 4D Flow. As shown in Figure 5, 4D Flow revealed distinct abnormal flow patterns (see Fig. 5), which may have led to an underestimation of flow in 2D.

Naturally, pathologies of the aorta itself can also influence aortic hemodynamics [8]. In such cases, 4D Flow can also help to visualize hemodynamics and parameters such as WSS may help us to identify areas at risk (see Fig. 6).

4D Flow provides different information on different aortic and/or aortic valve pathologies. This information can help us to better understand the pathology and therefore has the ability to influence how therapy is guided and decisions made.

Fast sequences and robust post processing are essential for routine clinical use.

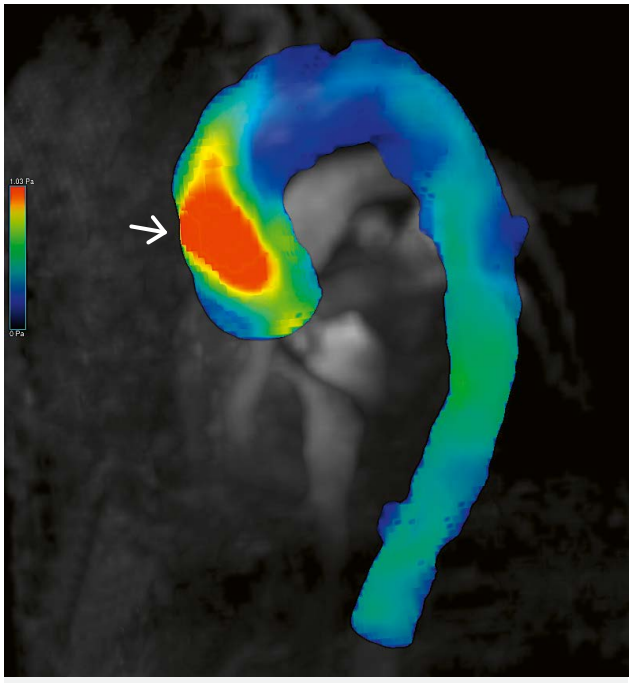

Figure 3:
Wall shear stress in the same patient with severe aortic stenosis as Figure 2. The patient's aorta is not yet dilated. However, one can observe the area of increased wall shear stress at the anterior/right side of the ascending aorta (white arrow) in the area most common for dilatation. The flow with the highest velocity was also in that area.

References

1 Markl M, et al. Advanced flow MRI: emerging techniques and applications. Clin Radiol. 2016; 71(8):779-95.
2 Crandon S, et al. Clinical applications of intra-cardiac four-dimensional flow cardiovascular magnetic resonance: A systematic review. Int J Cardiol. 2017; 249:486-93.
3 Dyverfeldt P, et al. 4D flow cardiovascular magnetic resonance consensus statement. J Cardiovasc Magn Reson. 2015; 17:72.
4 Lorenz R, et al. 4D flow magnetic resonance imaging in bicuspid aortic valve disease demonstrates altered distribution of aortic blood flow helicity. Magn Reson Med. 2014; 71(4):1542-53.

[2] *The information shown refers to products of third-party manufacturers and are thus their regulatory responsibility. Please contact the third-party manufacturer for further information.*

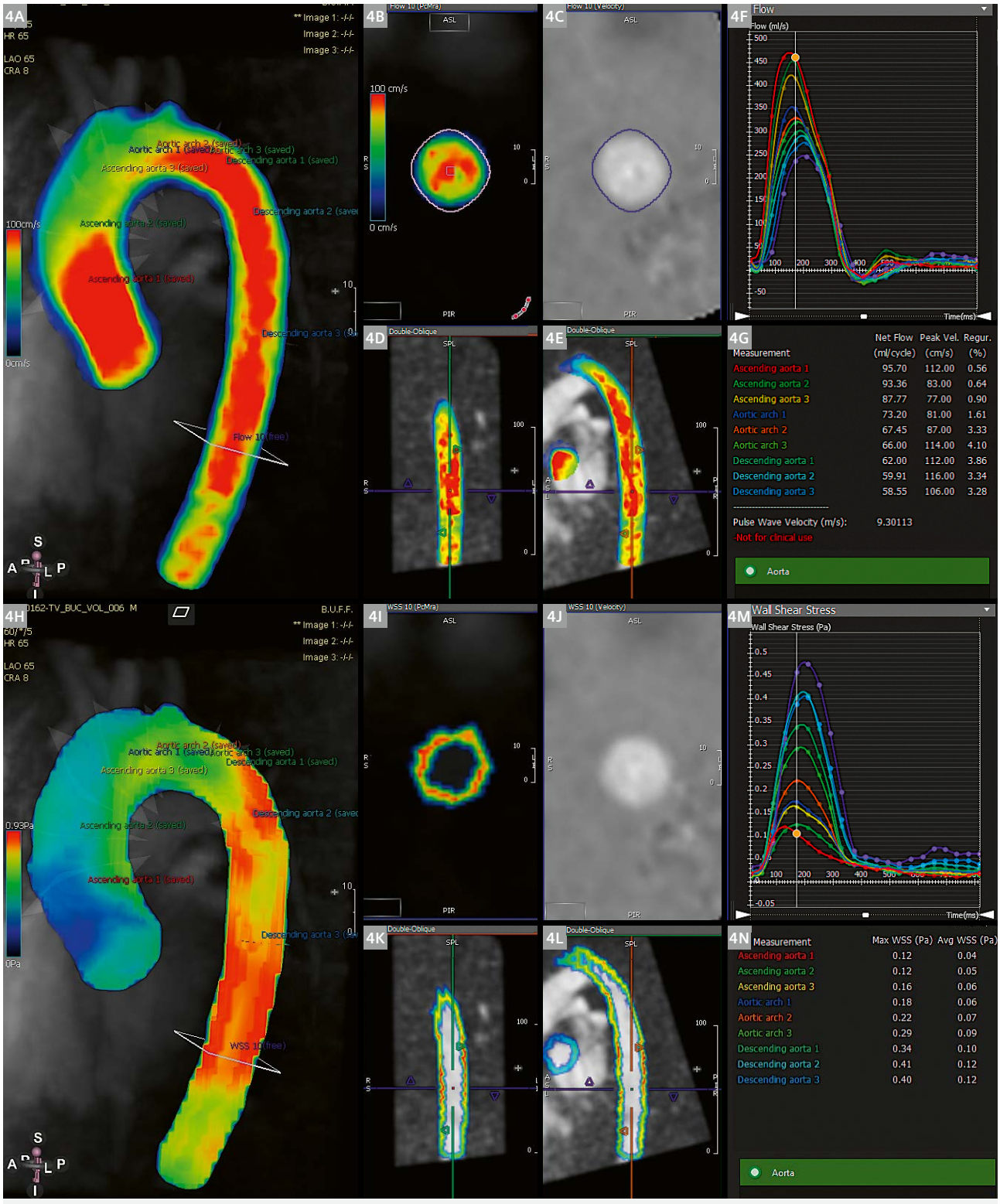

Figure 4:
Visualization and quantification of peak velocity, flow volumes **(4A–G)** and WSS **(4H–N)** by commercially available software (cvi42, Circle Cardiovascular Imaging, Calgary, Canada). Planes can be set anywhere in the aorta **(4A, 4H)** either perpendicular to the vessel or freely adjusted to flow jets **(4B–E, 4I–L)**. Parameters can be quantified over time as shown in the flow curves **(4F, M)**. Values will automatically be given for each plane **(4G, 4N)**.

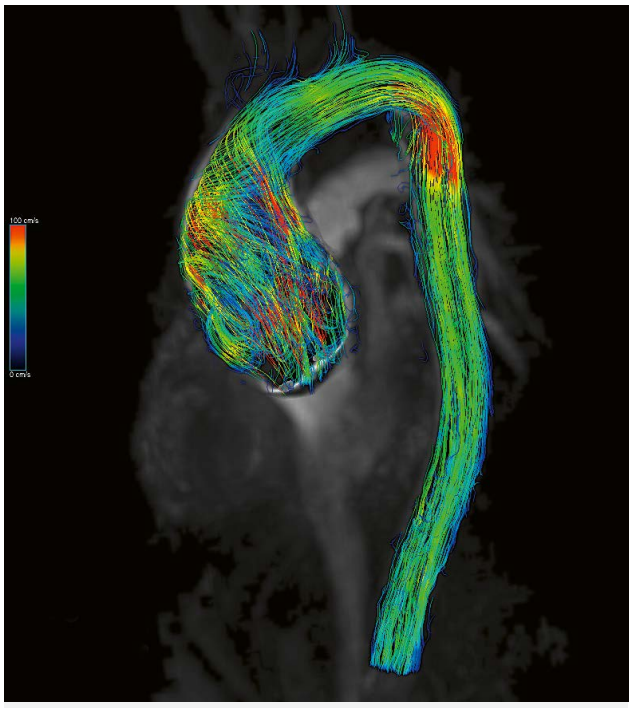

Figure 5:
Streamlines derived by 4D Flow in a patient with a low regurgitation fraction by 2D Flow, but strong indirect indicators of a more severe aortic insufficiency.

5 van Ooij P, et al. Aortic Valve Stenosis Alters Expression of Regional Aortic Wall Shear Stress: New Insights From a 4-Dimensional Flow Magnetic Resonance Imaging Study of 571 Subjects. J Am Heart Assoc. 2017; 6(9).

6 Barker AJ, et al. Bicuspid aortic valve is associated with altered wall shear stress in the ascending aorta. Circ Cardiovasc Imaging. 2012; 5(4):457-66.

7 von Knobelsdorff-Brenkenhoff F, et al. Evaluation of Aortic Blood Flow and Wall Shear Stress in Aortic Stenosis and Its Association With Left Ventricular Remodeling. Circ Cardiovasc Imaging. 2016; 9(3):e004038.

8 Geiger J, et al. Longitudinal Evaluation of Aortic Hemodynamics in Marfan Syndrome: New Insights from a 4D Flow Cardiovascular Magnetic Resonance Multi-Year Follow-Up Study. J Cardiovasc Magn Reson. 2017; 19(1):33.

9 Mathew RC, Loffler AI, and Salerno M. Role of Cardiac Magnetic Resonance Imaging in Valvular Heart Disease: Diagnosis, Assessment, and Management. Curr Cardiol Rep. 2018; 20(11):119.

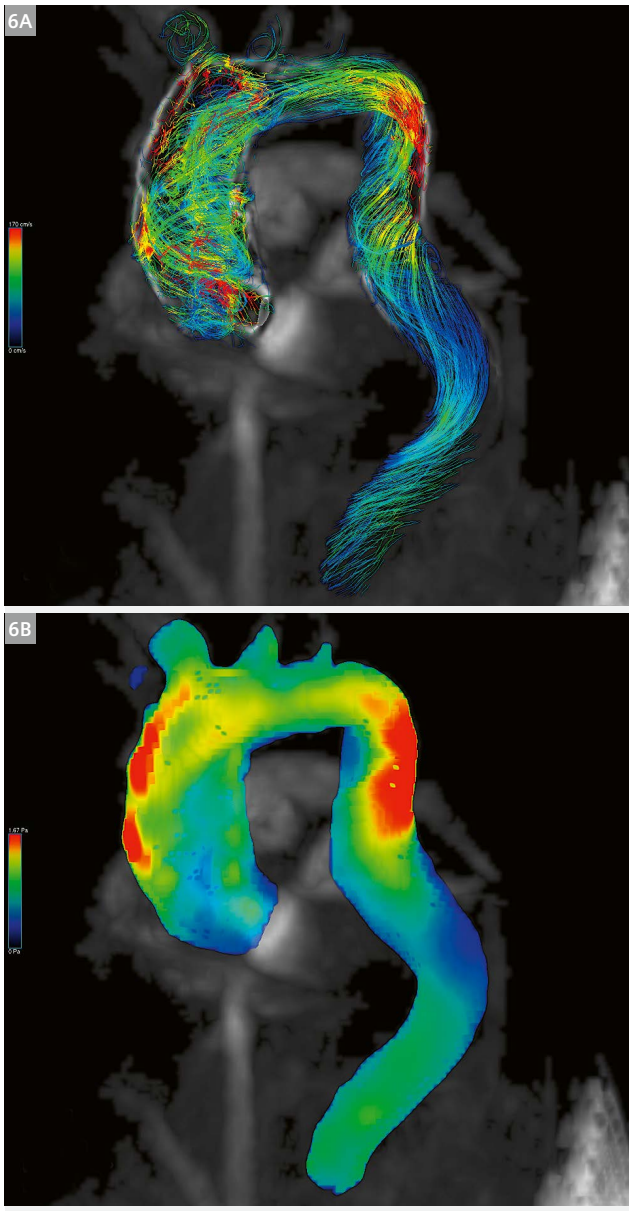

Figure 6:
Streamlines **(6A)** and wall shear stress **(6B)** in a patient with a contorted aorta. Note the abnormal flow pattern in the ascending and descending aorta and corresponding WSS.


Stephanie Funk


Aylin Demir


Jeanette Schulz-Menger

Contact

Professor Jeanette Schulz-Menger, M.D.
University Medicine Berlin
Charité Campus Buch, ECRC
HELIOS Clinics Berlin Buch,
Department for Cardiology and Nephrology
Schwanebecker Chaussee 50
13125 Berlin
Germany
Tel.: +49 30 040153536
jeanette.schulz-menger@charite.de

4-Dimensional Phase Contrast Imaging in Congenital Heart Disease: How we do it

Timothy C. Slesnick, M.D.; Sassan Hashemi, M.D.

Emory University School of Medicine, Children's Healthcare of Atlanta, Atlanta, GA, USA

Introduction

The field of phase contrast (PC) imaging has expanded greatly in the last 30 years. The fundamental principle that a moving nuclei will experience a phase shift when subjected to a magnetic field gradient that is proportional to the flow velocity, and thus measurement of this phase shift can allow measurement of the velocity of the nuclei [1, 2], has transformed our approach to flow quantification. Today, cardiac magnetic resonance (CMR) is the gold standard for quantification of vascular flows [3, 4]. Though initially confined to 2-dimensional (2D) measurements of either through plane or in-plane flow, the development of 4-dimensional phase contrast imaging (4D flow) was first applied to central nervous system vasculature in the late 1980's [5] and subsequently to cardiovascular blood flow in the late 1990's [6] and has opened new avenues and insights.

Two-dimensional phase contrast imaging is now a routine part of most CMR studies in pediatric and adult patients with congenital heart disease (CHD). Though options exist for both breath held and free breathing 2D PC sequences, our lab, like most, prefers to use free breathing techniques with multiple signal averages (NSA). Assessment of flow in the aorta (Ao) and main pulmonary artery (MPA) allows for quantification of systemic (Qs) and pulmonary blood flow (Qp). Flow in the right pulmonary artery (RPA) and left pulmonary artery (LPA) allows quantification of differential pulmonary blood flow, as well as validation of the MPA flow.

In the present work, we delineate our current practices with 4D flow imaging in children[1] and young adults with CHD, with a focus on practical tips for users to bring this technology to their programs and their patients. Illustrative cases are given with some of the ever-expanding array of applications for this technology. Finally, several recent advances are highlighted which promise to continue to evolve this new technique.

Works in progress 4D Flow

The fundamental tenants of 4D flow are flow encoding in all three directions (x, y, z-axes). True 4D flow sequences obtain a 3D volume, with the fourth dimension representing time. The works in progress (WIP) 4D flow pulse sequence[2] we currently utilize is WIP 785A, first released in January of 2016 (Figures 1A and 1B, Clip 1 – to access the .avi's please visit www.siemens.com/4Dflow). The sequence utilizes 3D Cartesian sampling with flow encoding and generalized auto-calibrating partially parallel acquisition (GRAPPA) acceleration where the reference lines are acquired separately (aka ePAT). Acceleration can be applied in both phase encoding and the partition encoding directions since the dataset is a true 3D volume, with the expected decrease in signal to noise (SNR) of square root of each of the acceleration factors. When acceleration is applied in both phase encoding

[1] *Siemens Healthineers Disclaimer does not represent the opinion of the authors: MR scanning has not been established as safe for imaging fetuses and infants less than two years of age. The responsible physician must evaluate the benefits of the MR examination compared to those of other imaging procedures.*

[2] *WIP, the product is currently under development and is not for sale in the US and in other countries. Its future availability cannot be ensured.*

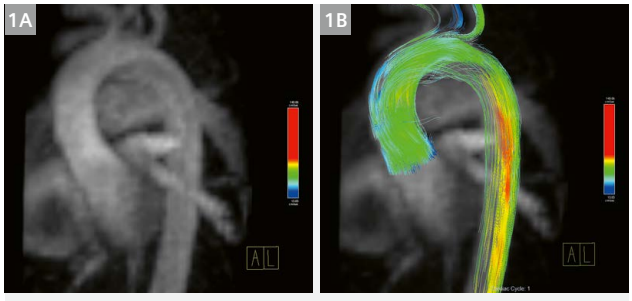

Figure 1:
4D flow magnitude **(1A)** image of an aortic arch obtained using WIP 785A, as well as particle trace image **(1B)**.

and partition encoding directions, SNR is decreased by the product of those factors, but the resultant change in the geometry factor, which also influences signal to noise loss, is less pronounced than if all acceleration is performed in one direction, so acceleration of 2 x 2 does result in less signal loss than 4 x 1. One final point on acceleration is that running 4D flow sequences post-contrast will obviously result in more signal, and thus more acceleration can be applied without loss of data integrity. On our 1.5 Tesla scanner, we typically run our 4D flow sequences post contrast (if contrast is given during the routine exam), and apply ePAT in either the phase encoding direction alone with a factor of 3 or in both the phase and partition encoding directions with factors of 2 for each (2 x 2). If no contrast is given to the patients during routine exam, we typically run the 4D flow sequence applying parallel imaging with a factor of 2 in the phase encoding direction alone.

In order to obtain this quantity of data, even for a small slab of coverage, requires substantial *k*-space sampling, far longer than is possible in a breath held study. In order to minimize respiratory motion, a respiratory navigator is typically employed (though as delineated below in the product section free breathing techniques with multiple signal averages can also be used). A cross-beam respiratory navigator is positioned on the dome of the diaphragm, and an acceptance window of ± 3–5 mm is typically used (± 3 mm for smaller children, ± 4–5 mm for larger children and young adults). Some users have reported using larger respiratory navigator windows, up to ± 8 mm, with acceptable degree of motion artifacts, but we do not have personal experience with this broad a range of respiratory navigated acceptance.

The WIP sequence can be run with either prospective or retrospective gating. In patients with an irregular heart rate, it is possible to use prospective ECG gating with a reduced acquisition window to avoid data acquisition spanning into the early systolic phase of the following heartbeat. In our experience, however, we find that even with optimal modifications to the 4D flow sequences, the validity of the data due to the inherent fluctuations in the hemodynamics of patients with significant arrhythmias continues to be challenging, and typically we choose not to perform 4D Flow imaging in these patients.

Using retrospective gating, the number of reconstructed phases ("Calculated phases") can be set by the user (Figure 2). Caution should be employed, however, that the reconstructed phases will be interpolated from the true number of cardiac phases acquired, which is determined by the heart rate and the repetition time. For example, we typically acquire 3 segments per heart beat per cardiac phase, which results in a TR of 58.2 msec. In a patient with a heart rate of 75 beats per minute (bpm), and a resultant cardiac cycle of 800 msec, this would yield 13 true cardiac phases. Though the interface allows the user to set the number of reconstructed phases to any desired value, our experience has shown that using slightly less than double the number of true phases produces values which correlate well with 2D PC data. We therefore typically calculate the actual number of phases for a given patient and sequence prescription, double the value, and then decrease slightly to allow

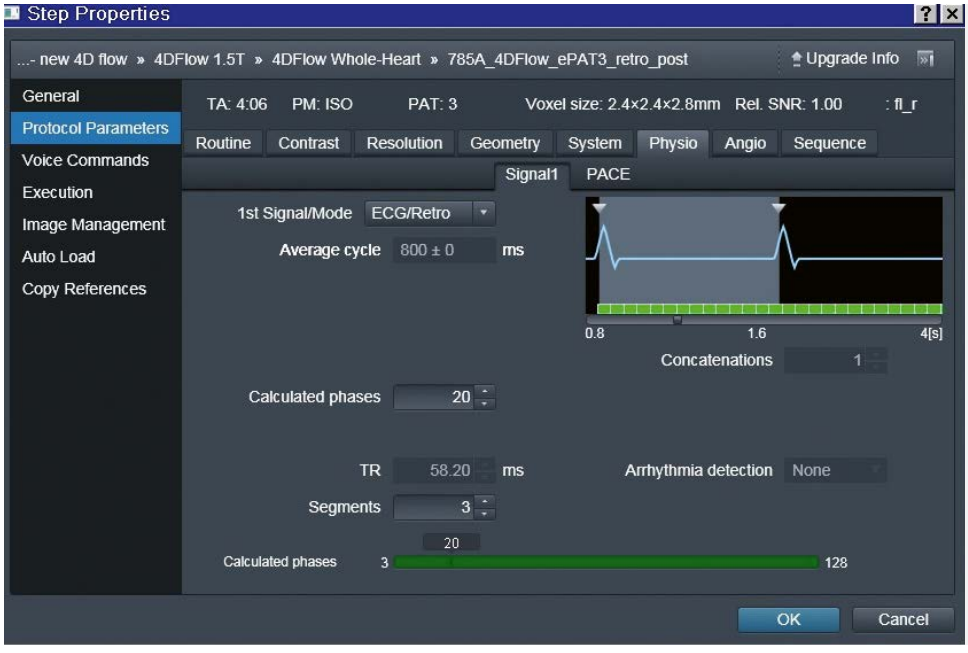

Figure 2:
Screen shot demonstrating the Physio tab on the user interface where the number of "Calculated Phases" can be adjusted and the number of true phases can be calculated (cardiac cycle length divided by the TR).

all reconstructed phases to have some component of unique data.

Though this manipulation may seem a bit cumbersome, it allows the user to tailor the sequence and results to the individual patient. For smaller children with faster heart rates, it may be necessary to decrease the number of segments to 2 to allow a shorter TR and thus more reconstructed phases. Conversely, in older patients with slower heart rates (< 50–55 bpm) we will often increase segments to 4 to speed up the acquisition without compromising the number of reconstructed phases. Since each change to the number of segments has a direct correlation to the scan length, these manipulations must be made very thoughtfully. Increasing from 3 to 4 segments will cut acquisition time by 25%, while decreasing from 3 to 2 segments will require 50% longer. For most of our scans, we aim to reconstruct 16–25 phases, adjusting the parameters as needed.

As with any 3D dataset, obtaining isotropic voxels is advantageous as it allows the user to reformat/slice the data in any plane without loss of resolution. With the 4D Flow WIP, we typically decrease the phase and slice encoding direction percentages, so the actual obtained voxels are not quite isotropic, but the reconstructed voxels are. The user must remember that the voxel size is determined by the field of view (FOV), matrix (base resolution), and the slice thickness. FOV and matrix can be changed, but this does affect the in plane resolution and the SNR. The sequence will allow decreasing slice thickness to 1.5 mm, though in our lab we typically run the sequence at 2 mm isotropic.

Slice coverage is prescribed based on the anatomy of interest. For aortic pathology, simply covering the aortic arch (with care taken that the entirety of the aortic root, which is typically the largest portion of the thoracic aorta, is fully covered) is often sufficient. Aligning the plane in a sagittal oblique geometry along the long axis of the arch allows maximal coverage in a minimum number of slices. Depending on the child's (and aorta's) size, this can often be accomplished in as few as 12–14 slices, though with more dilated aortas 16–20 slices may be necessary. For alternative underlying pathologies, coverage may be needed for the entire ventricular volumes (when heart failure or inflow/outflow assessment is desired), branch pulmonary arteries (for TOF and single ventricle [SV] patients), or systemic or pulmonary veins (particularly in patients with anomalous returns). These cases often require wider coverage and thus more slices, so the balance between voxel size and acquisition time is paramount when planning these scans. For most 4D Flow datasets, we prescribe a straight or oblique sagittal plane of some type. Axial geometries can be used if only branch PA flow is desired, but coverage in the z-direction with axial slices is often quite limited unless large slabs are obtained. Coronal orientations are also possible, but will require phase encoding in the left-right direction (as opposed to anterior-posterior in sagittal or axial oblique geometries), so FOV and acquisition duration will be increased. Additionally, some analysis platforms have difficulties processing coronal 4D Flow datasets, though this can be overcome with manipulation on the user interface.

The final component we prescribe is our velocity encoding upper limits (VENC). As explained in the case examples below, we routinely set the VENC at the highest velocity value within the imaging prescription of interest to avoid aliasing. For most aortic and pulmonary artery studies we use either 150 or 200 cm/sec, unless there is known stenosis of a valve or great artery. For single ventricle studies where the bidirectional Glenn (BDG) or Fontan circuit are the primary area of interest, either 100 or 120 cm/sec is used, with the knowledge that aliasing may occur in the aorta but that is outside the primary vessels of interest (if quantification in the aorta is desired in an SV patient, then 150 or 200 cm/sec is used).

Product 4D Flow options

True 3D datasets

The current software platforms for Siemens Healthineers magnets allow the user to prescribe a 4D Flow dataset with a true 3D volume and flow encoding in all three directions using the product sequences alone (Figures 3A and 3B, Clip 2). This derivation must start with a base product sequence which utilizes prospective ECG triggering (more on this in a moment). On our magnet (MAGNETOM Avanto^{fit} on software platform *syngo* MR E11B), we have built this option from the underlying, "BEAT_FQ" sequence, though other options are possible. On *syngo* MR E11B, the current product sequence will not support a 3D acquisition

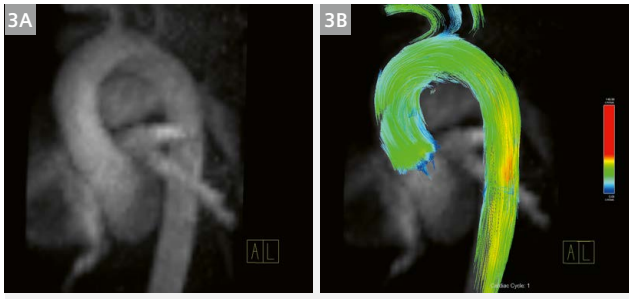

Figure 3:
4D flow magnitude **(3A)** image of an aortic arch obtained using the product 4D flow derivative, as well as particle trace image **(3B)**.

when parallel imaging with GRAPPA and reference lines obtained using "GRE/separate" (aka ePAT) is employed, so under the Resolution tab, iPAT subtab, "Integrated" must be selected to change to iPAT parallel imaging (Figure 4). On the *syngo* MR E11C and subsequent platforms 3D acquisitions are possible with ePAT image acceleration. For the product 3D acquisition, parallel imaging can only be used in the phase encoding direction. We typically run the sequence with 3 fold acceleration and perform it post-contrast to ensure adequate signal. Next, under the Sequence card, Part 1 subtab, the Dimension can be changed from 2D to 3D (for *syngo* MR E11B this option will not be available until the parallel imaging is changed from ePAT to iPAT) (Figure 5). This change will automatically convert the flow direction from "Single dir" to "Single vel" (which results in flow encoding in all three directions, represented as F>>H, Throughplane, and A>>P in a sagittal geometry) (Figure 6).

Product phase contrast sequences do not have an option for a respiratory navigator, and since data acquisition is far too long for an individual breath-hold, free breathing techniques with multiple signal averages

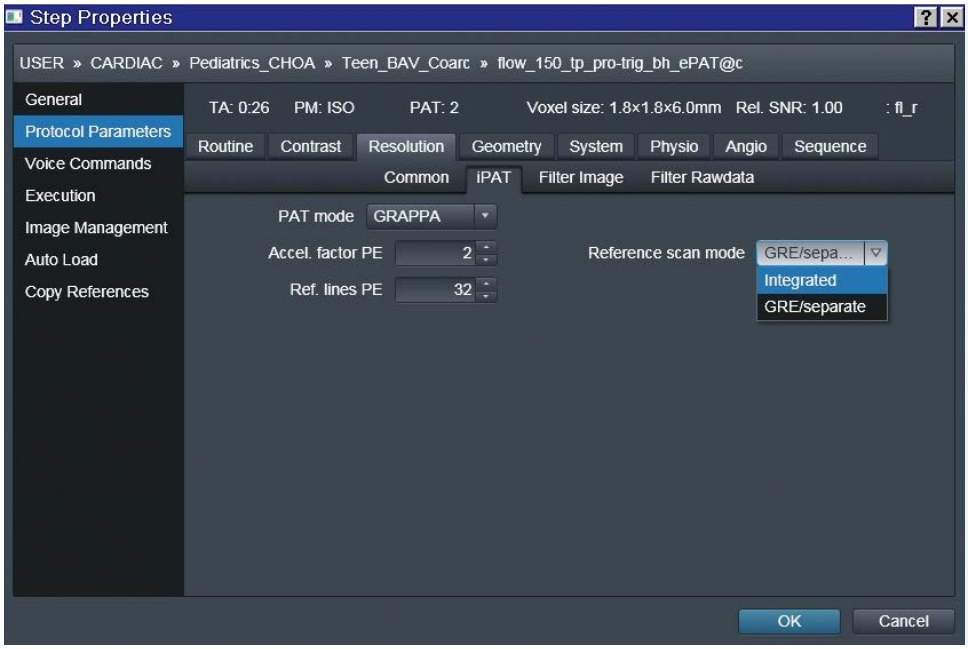

Figure 4:
Screen shot illustrating how the reference line acquisition must be changed from "GRE/separate" to "Integrated" (aka ePAT to iPAT) in order to convert the sequence as described in the text.

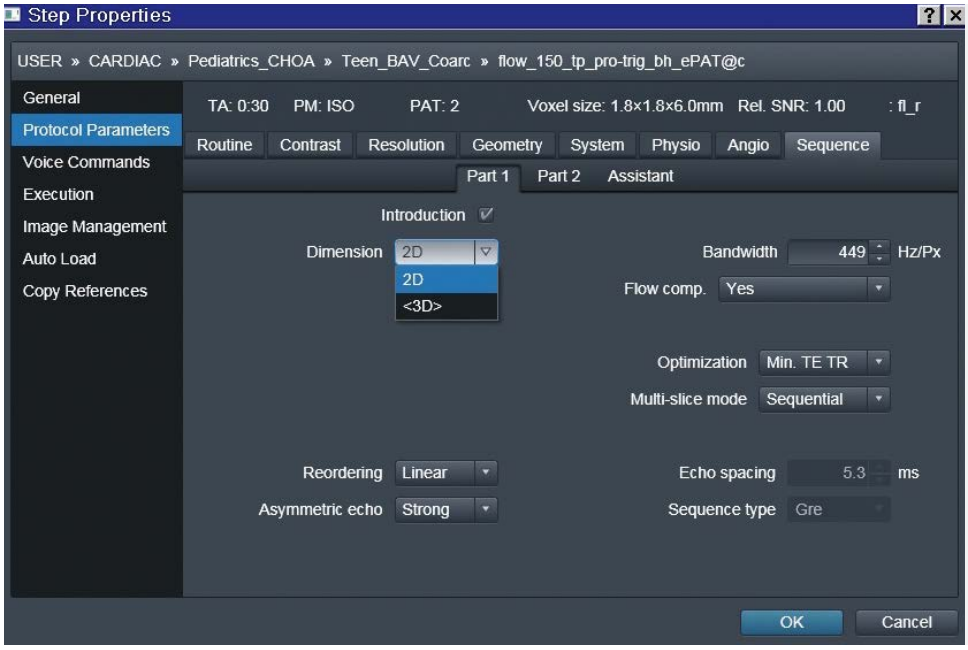

Figure 5:
Screen shot illustrating how the 2D product phase contrast sequence can be changed to a 3D volume under the Sequence tab, Part 1.

are needed. Since this variant does produce a true 3D volume, it is less respiratory motion sensitive, so we typically acquire 2 NSA.

Slice thickness can be as thin as 1 mm, though again we typically run this variant at 2–2.5 mm in the interest of acquisition time. FOV and matrix are adjusted to ensure isotropic voxels. Slice orientation and number are set to cover the regions of interest. The VENC is set as described above.

The largest difference in this variant of 4D Flow is that the Siemens Healthineers current product sequence does not support retrospective gating for 3D volumes. This fact has three important consequences. First, the end of diastole cannot be captured, and thus the sequence represents only a large portion (not the entirety) of the cardiac cycle. Second, unexpected pronounced heart rate variability result in challenges with data sampling both in mistiming at the end of the cardiac cycle and missed acquisition on the beats following shorter cardiac intervals. Finally, with prospective gating, the number of phases is fixed

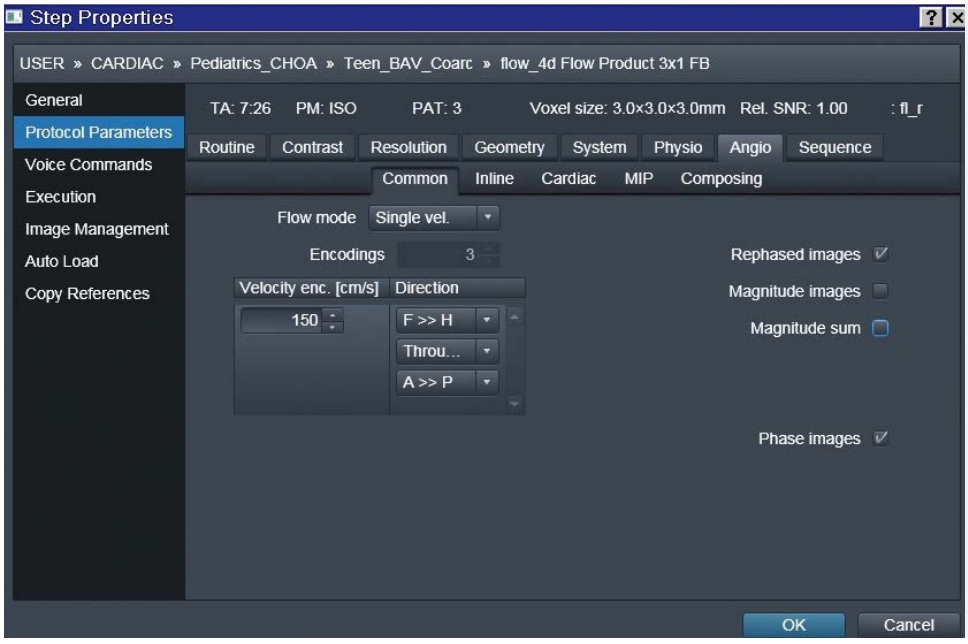

Figure 6:
Screen shot illustrating the change to the "Single vel" option with velocity encoding in all three directions (F>>H, Throughplane, and A>>P) under the Angio tab.

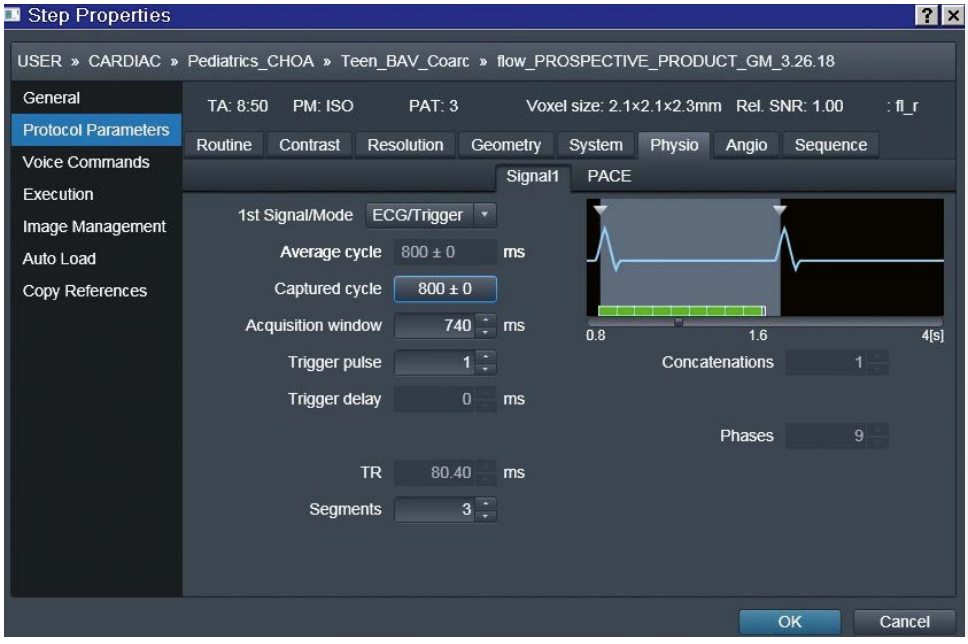

Figure 7:
Screen shot demonstrating the Physio tab on the user interface where the number of phases is displayed on the right hand side. Note, that compared to the WIP version, there is no input for "Calculated Phases" since this sequence is prospectively gated.

at the true number of acquired phases and cannot be interpolated to yield more reconstructed phases. Thus for this product 4D Flow sequence on a patient with an average heart rate of 75 bpm, a resultant cardiac cycle of 800 msec, the repetition time would be 80.4 msec (assuming 3 segments are selected) and there will only be 9 phases produced (Figure 7). If the user desires more phases, the number of segments must be reduced (with resultant increased acquisition time).

"Pseudo 4D Flow": Contiguous stack of 2D slices

An additional alternative to the product 4D Flow described above is acquisition of a contiguous stack of 2D slices, each with flow encoding in all three directions, which in summation represent a 3D volume (Figures 8A and 8B, Clip 3). The sequence can again be built starting with the base "BEAT_FQ" sequence. It is important when setting up the multiple 2D slices to utilize no slice gap (aka "Distance factor") (Figure 9). Parallel imaging can remain with "GRE/separate", and similar to the true 3D product sequence, acceleration is only possible in the phase encoding direction. We typically run the sequence post-contrast with 3 fold acceleration.

Since there is no option for respiratory navigator on the product flow sequences, again multiple signal averages are employed. As opposed to the variant described above, 2D slices are more motion sensitive, so we typically utilize 3 NSA with the patient free breathing (though with small patients and very shallow respirations, we have utilized 2 NSA with this variant).

With a contiguous stack of 2D slices, minimum slice thickness is 2.8 mm, which means that even with FOV and matrix optimization, the isotropic voxel size is larger than on other 4D flow variants. Typically, we run this variant with 3 mm isotropic voxels, which does result in decreased resolution which is readily apparent on the magnitude images (Figures 10A and 10B), but as explained below, still produces reasonable data for flow visualization and hemodynamic analysis.

Under the Angio tab, "Flow mode" can be manually changed from the standard "Single dir" to the "Single vel" (Figure 6). The VENC is set to an appropriate value. The contiguous stack of 2D slices variant does have the advantage that it, like the WIP, can be run with retrospective gating, and thus the number of reconstructed phases can be set by the user (Figure 11). As described above, we do not recommend setting the total phases greater than twice the number of actual phases as

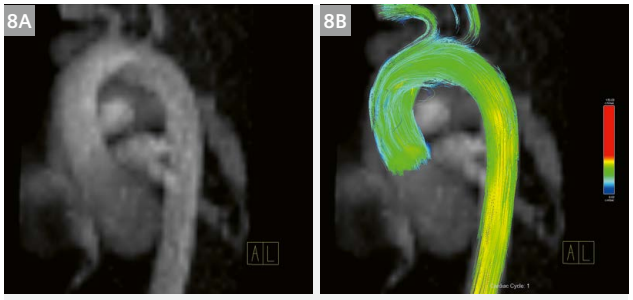

Figure 8:
4D flow magnitude **(8A)** image of an aortic arch obtained using the product "pseudo 4D flow" stack of 2D slices derivative, as well as particle trace image **(8B)**.

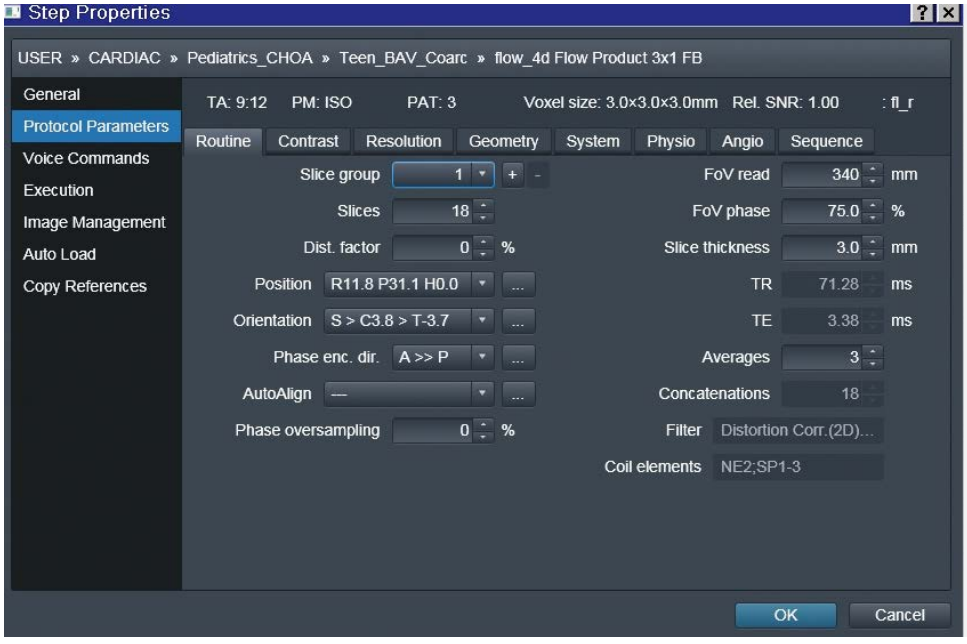

Figure 9:
Screen shot of the Routine tab where the stack of slices are composed with no gap ("Distance Factor").

determined by the repetition time and the heart rate, but you can achieve improved temporal resolution compared to the other product variant (where prospective gating is the only option).

In our experience, for similar patient's conditions and imaging data size, the continuous stack of 2D slices technique requires a shorter acquisition time than the true 3D volume product variant. This time saving does come at a price of worse spatial resolution, but offers the user improved temporal resolution compared to the other product option and also does allow retrospective gating. As described below, for flow visualization and simple quantification, we have found the resolution of this technique to be sufficient.

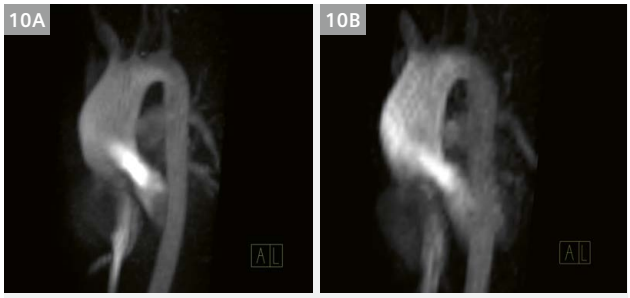

Figure 10:
Comparison of imaging on the same patient with both WIP **(10A)** and product pseudo 4D flow images **(10B)**. Note that the spatial resolution is not as good with the latter technique.

Analysis of data

Currently, we use prototype Siemens Healthineers "4Dflow v2.4" software for the majority of our 4D flow post-processing. In its current form, it is a work-in-progress software intended only for research which is equipped with good visualization and analytic options. User interface is simple and familiar since it uses the same format as in other MRI software packages in the Siemens Healthineers *syngo* ecosystem. It is divided into six consecutive tabs which guide the user from loading the data to visualization of 4D flow.

There is no PACS integration available at this time and 4D flow data should be loaded from a local disk. After loading the study ("Study Load" tab), the user can navigate between different phases and slices to find the desired structure and check for gross aliasing in different velocity encoding directions. You can also crop the dataset in phase and frequency encoding directions retrospectively (Crop Box). This helps to minimize the use of processing resources by the software, provides more accurate background phase correction and also reduces noise during visualization.

The second tab, "Corrections", provides background phase correction, anti-aliasing and motion tracking. Background phase correction extracts the stationary tissue by looking at the variance of velocities in each voxel which is deemed to be the lowest for stationary tissue. The resultant velocities in each slice are corrected so that the stationary tissue has zero velocity. As mentioned previously, cropping the dataset in the previous tab helps to eliminate wrap and ghosting artifacts which may

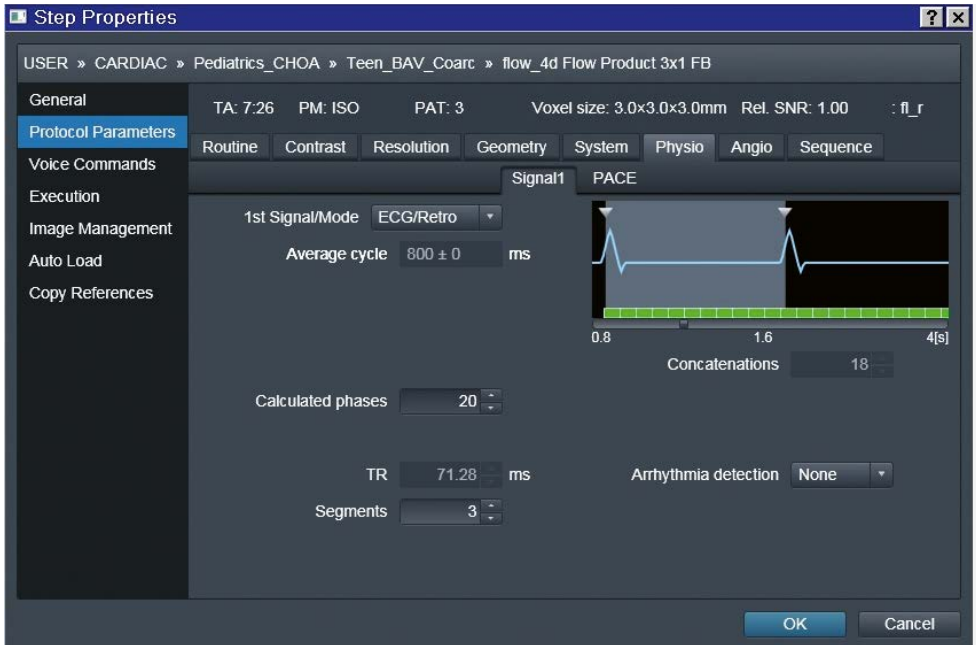

Figure 11:
Similar to Image 2, the Physio tab on the user interface with the stack of 2D slices technique gives the user the ability to input the number of "Calculated Phases".

interfere with stationary tissue extraction. The anti-aliasing algorithm looks for very large opposite jumps in the velocity-time curve for each voxel and removes the wrap introduced by insufficient velocity range. Finally, motion tracking uses a symmetric deformable registration technique to track the segmented anatomy, analysis planes and particle seeds over time. Note that motion tracking requires at a minimum of 16 slices to function properly, per the Siemens Healthineers user manual. We recommend utilizing all three correction techniques to provide the most robust data.

Before proceeding to the next tab, we adjust the "segmentation threshold" from the tools tab in the bottom toolbox. This slider controls the threshold-based segmentation according to the signal intensity. The goal is to find the balance between including the desired anatomy without going beyond vessel boundary (Figure 12). After adjusting the threshold, the mesh transparency can be adjusted or turned off from the display tab if desired.

Since the majority of our 4D flow patients have complex and abnormal flow patterns (e.g. eccentric and helical flow in ascending aorta in stenotic bicuspid aortic valve or low velocity and opposing flow directions in Fontan circuit), we have opted not to use centerline and vessel model extraction available in "Segmentation" tab and skip to "Flow evaluation". These are options within the software platform and can streamline the workflow for patients with laminar flow, but for the majority of our cases this aspect of the software often produces unreliable results (Figure 13).

Next, under the "Flow evaluation" tab, there are different functions located under sub-tabs: "Planes" and "Calc". Under Planes, the user can draw contours along the vessel(s) of interest for flow quantification and particle seeding for visualization. We recommend setting the overlay to "none" for easier recognition of the anatomy (Figure 14). One can then navigate through the vessel in the 3D viewer on the left hand side of the screen. Note that contours can only be drawn in the left upper window, marked by a red border. Therefore, the red orthogonal line should always be perpendicular to the flow at the desired location. Once a contour is drawn, the flow-time curve will be automatically shown in the lower section of the screen. After all contours are added, user can switch to calculation tab to get detailed flow quantification (e.g. net flow, velocities, regurgitation fraction) through each contour. This is a valuable option to cross-examine 2D phase contrast flow data with 4D flow, especially in cases when 2D flow data quality is suboptimal (Figure 15).

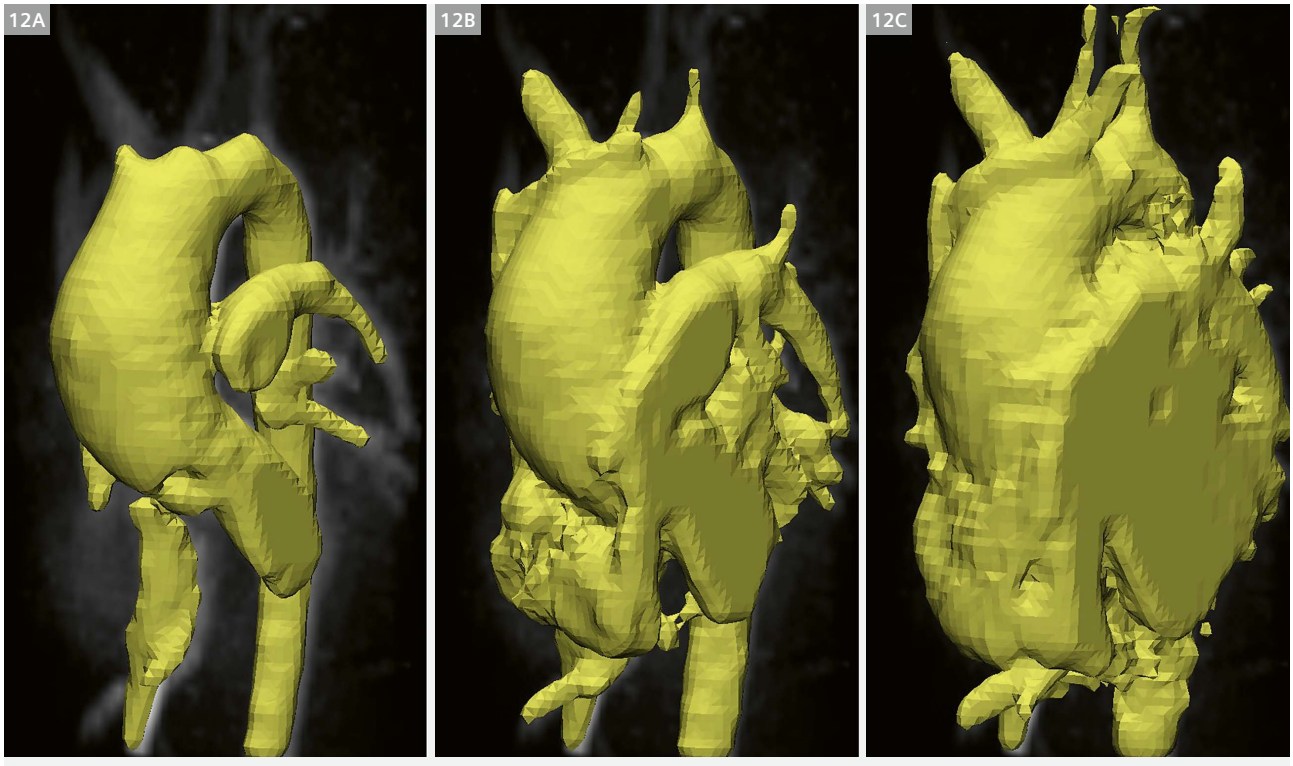

Figure 12:
Segmentation with the Threshold slider: inadequate **(12A)**, adequate **(12B)**, excessive **(12C)** threshold.

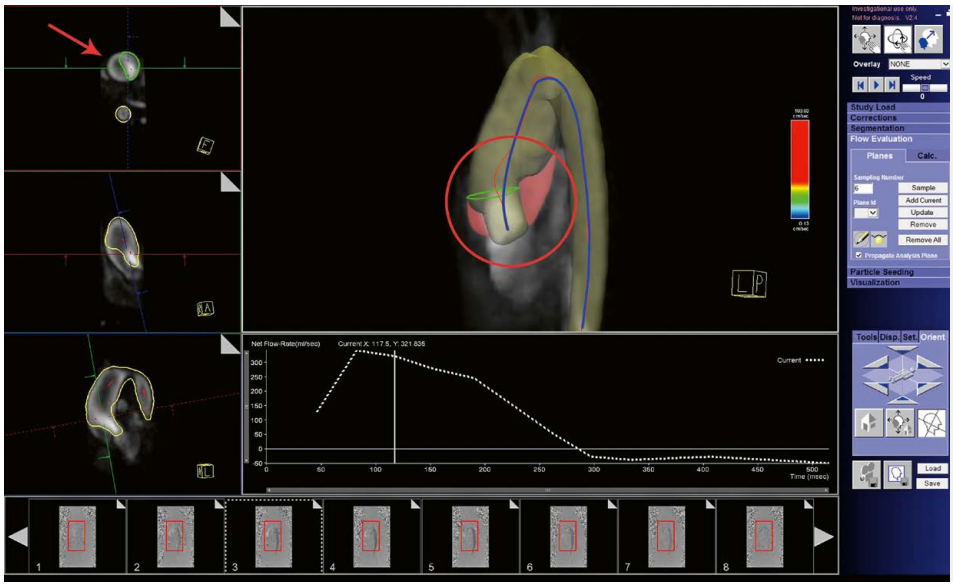

Figure 13:
Unsuccessful centerline extraction and volume segmentation in a patient with bicuspid aortic valve. The true centerline (blue) and unsegmented aortic volume (bright red) are shown. Arrow points to the unsegmented ascending aortic lumen in axial plane.

Figure 14:
Switching the overlay preset to “none” makes for easier navigation of the anatomy in the left panel (arrow).

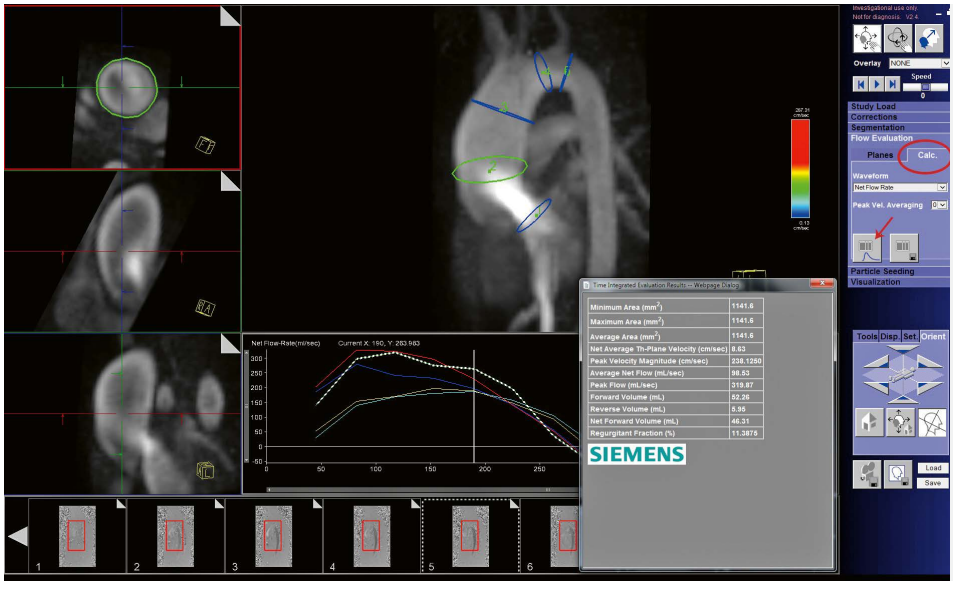

Figure 15:
Flow quantification through the desired contour by switching to the “Calc” tab in flow evaluation.

The focus of the last two tabs is visualization of 4D flow. The "Particle seeding" tab allows the user to seed each contour drawn in the previous step with either the same or different colors (up to 4 colors). In cases where there are multiple inflows, the user can assign different colors to better visualize flow contribution and behavior during mixing (e.g. color coding SVC and IVC in Fontan circuit or pulmonary veins and mitral regurgitation jet in mitral valve disease). The user can also choose between seeding the drawn contours or the entire segmented volume by switching between volume and planes in the drop down menu. There are options to control the density of particle seeds, intervals in which they are emitted and the number of cardiac cycles they are visualized throughout. In our lab, we typically only change particle density for better visualization. In general, we use higher density in cases with larger voxel size (50–60% for 2–2.5 mm voxels and 70–80% for 2.6–3 mm voxels).

The final tab offers three visualization options. "Vector Field" illustrates the velocity vectors summation in the segmented planes or volume for each voxel over the cardiac cycle. "Particle Traces" continuously creates time-resolved pathlines originating from the seed planes to visualize the dynamic change in trajectory and velocity. "Streamlines" captures the instantaneous 3D velocity vector field in each cardiac phase. Unlike "Particle Traces", it does not represent temporal evolution of flow in the vessel (Figure 16). We prefer to visualize our 4D flow data with "Particle Traces" since subjectively it is more easily understood (and has good agreement with "Streamline" visualization). Finally, the user can export desired images or movie clips or save the workflow (segmentation, centerline and contours) for future use.

Case examples

Our most common patient population in which we utilize 4D flow imaging is those with various forms of Aortopathies. Bicuspid aortic valve patients frequently have abnormal flow jets in the ascending aorta, and in extreme examples can have a left hand helix pattern (Figure 17, Clip 4). Those with genetic syndromes, such as Turner syndrome, may have vortex formations in atypical locations, such as at the base of the left subclavian artery at the terminal end of an elongated transverse arch (Figure 18, Clip 5). There is work underway to assess these abnormal flow patterns and the resultant effect on wall integrity, rate of vascular dilation, and propensity to dissection [7–9]. Using the tools we have described above, flow dynamics can be visualized and basic assessment of hemodynamics can be obtained. Calculation of wall shear stress can also be performed. In our lab, when patients are found to have altered flow patterns in various forms of Aortopathy, the frequency of their follow up is often increased, and consideration is given for how these insights help predict their risk of cardiovascular events in the scope of surgical timing and planning.

The next most common patient population is those with repaired tetralogy of Fallot (TOF). Regardless of whether a transannular patch is used at the time of TOF repair, the pulmonary valve is virtually always non-functional by the time patients reach adolescence, and severe pulmonary insufficiency (coupled often with some degree of residual obstruction) is nearly universal. Visualization of the flow in the RVOT, both stenotic and regurgitant, is very helpful to understand the progression of the disease (Figure 19, Clip 6). Flow within the main and branch PA's, with quantification of vortices, can be

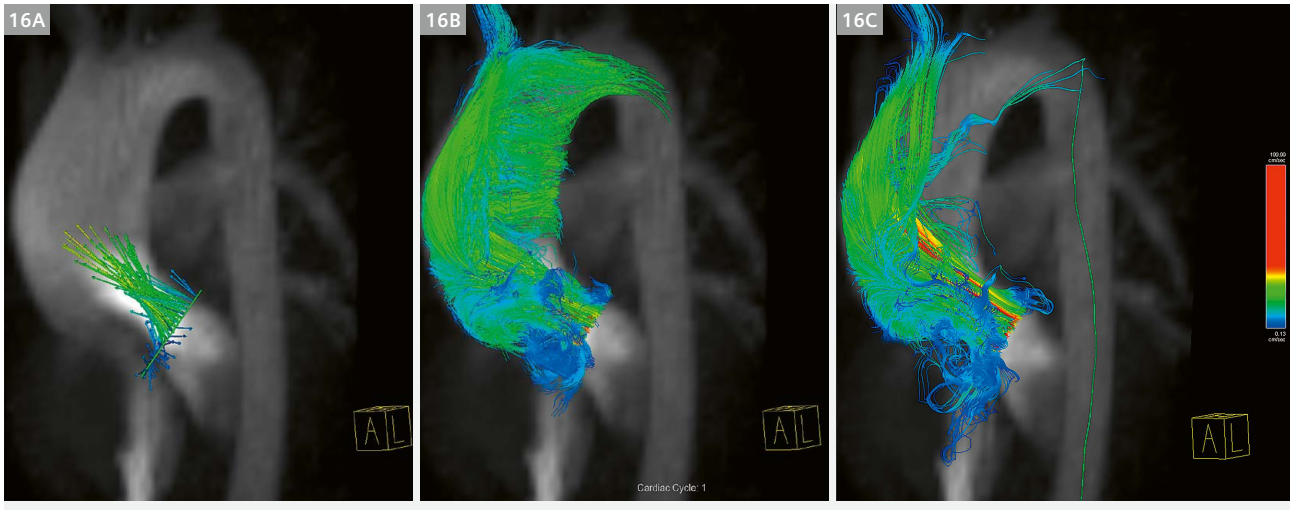

Figure 16:
Visualization options: vector field **(16A)**, particle traces **(16B)** and Steamlines **(16C)**.

studied and correlated with presence and rate of RV dilation [10–12]. In those with irregular main and branch pulmonary artery architecture, such as those with pseudoaneurysm formation, these abnormal flow patterns are even more pronounced (Figure 20, Clip 6).

In our opinion, one of the most helpful patient subgroups for 4D flow imaging are those with single ventricle anatomies. A heterogeneous group, ranging from variants such as tricuspid atresia with a single left ventricle, to those with hypoplastic left heart syndrome with a single

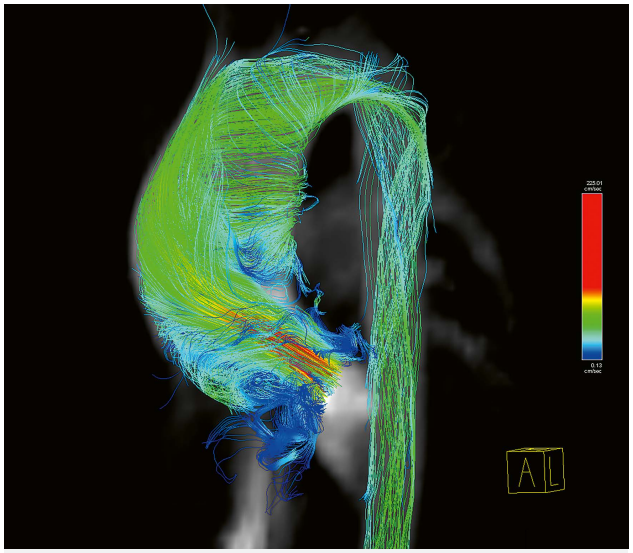

Figure 17:
Patient with a bicuspid aortic valve and a left hand helical pattern in the ascending aorta.

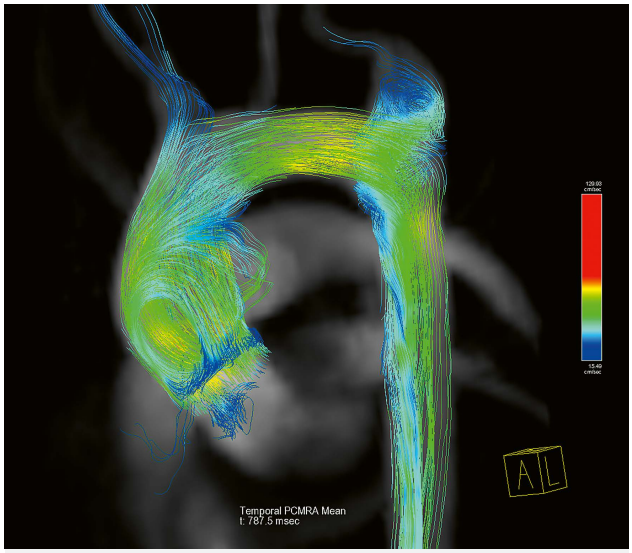

Figure 18:
Patient with Turner syndrome, no evidence of coarctation of the aorta, but with a prominent vortex formation at the base of the left subclavian artery.

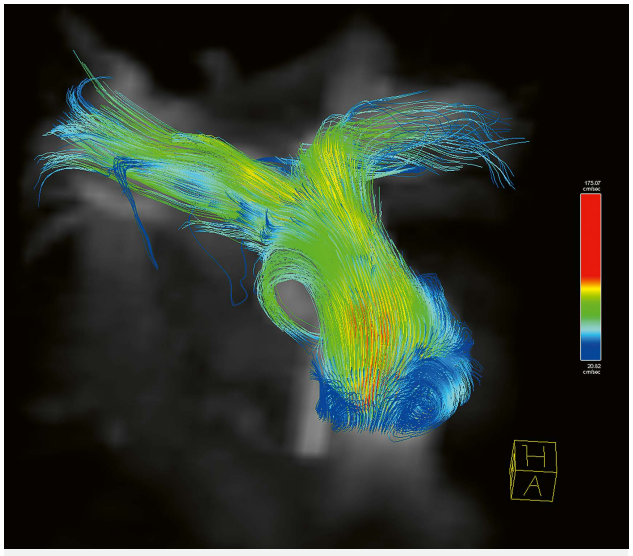

Figure 19:
Patient with repaired tetralogy of Fallot and turbulent flow noted in the main and branch pulmonary arteries.

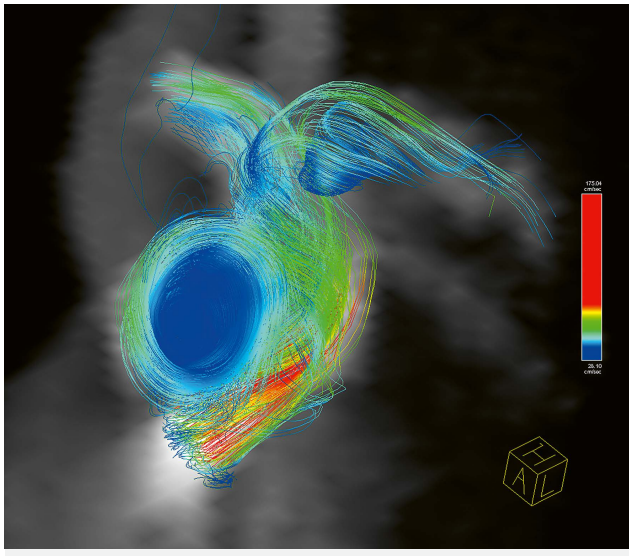

Figure 20:
Different patient with repaired tetralogy of Fallot and a pseudoaneursym on the anterior surface of the main pulmonary artery. Note the prominent vortex within the pseudoaneurysm.

right ventricle, to those with heterotaxy syndrome with a myriad of systemic and pulmonary venous anomalies on top of their intracardiac defects, these patients truly represent the extreme end of complexity in the field of congenital heart disease. The unifying feature for these patients is the series of staged palliations they undergo, culminating in a Fontan procedure. With only a single functional ventricle which must be used to pump blood to the body, the Fontan circulation relies on passive systemic venous return into the pulmonary arteries by anastomosing the superior vena cava (SVC) (Figure 21, Clip 7) directly to the PA and connecting the inferior vena cava (IVC) to the PA as well (Figure 22, Clip 8), via either an intracardiac tunnel or a separate conduit.

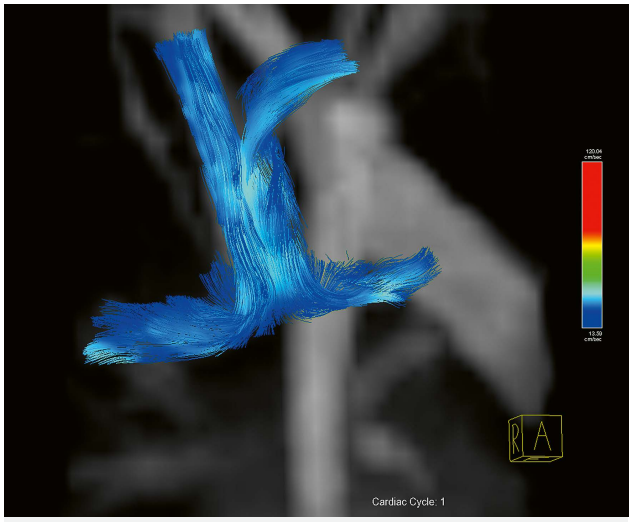

Figure 21:
Flow from the superior vena cava into the branch pulmonary arteries in a patient with single ventricle anatomy who has undergone a bidirectional Glenn anastomosis.

In patients who have undergone a Fontan completion, altered flow hemodynamics within their circuit can lead to several clinical issues. One of the most difficult to assess is formation of pulmonary arteriovenous malformations (PAVM), thought to be due to lack of a component of hepatic blood flow (termed "hepatic factor") to reach the pulmonary capillary bed in affected lung segments. Knowledge of the streaming of the inferior systemic venous return, therefore, is of paramount importance in assessing these patients' risk for development of PAVM's [13]. Traditional 2D flow imaging can assess total volumes of flow into the RPA and LPA, but cannot quantify how much of each lung's arterial supply comes from the IVC versus the SVC. While the Siemens Healthineers software mentioned above does not have specific features to quantify flow volumes produced only from select vessels, we have developed an in-house MATLAB code which allows us to perform these calculations.

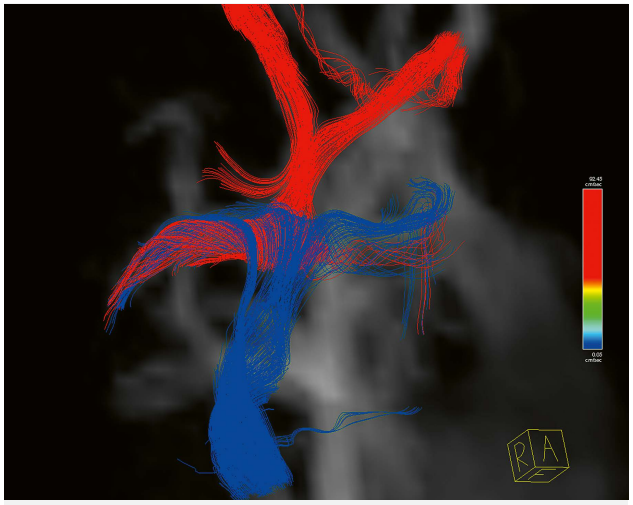

Figure 22:
Flow from the superior vena cava (colored red) and inferior vena cava (labeled blue) into the branch pulmonary arteries in a patient with single ventricle anatomy who has undergone a bidirectional Glenn anastomosis and subsequent Fontan completion. In this patient's case, there was a small fenestration placed in the Fontan baffle, seen by the blue streamlines heading rightward on the image near the lower margin of the Fontan.

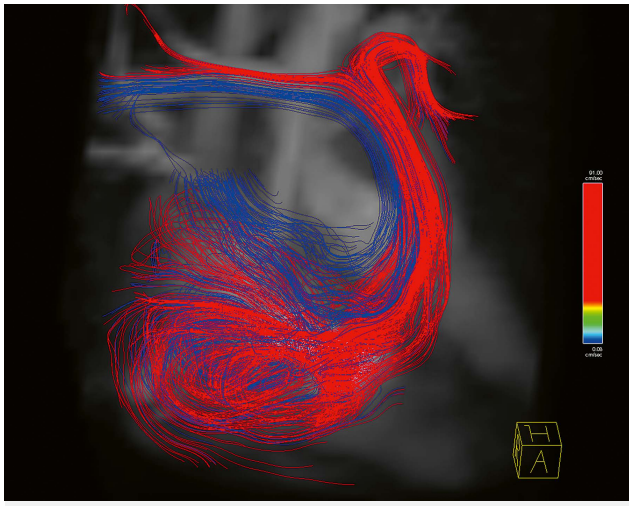

Figure 23:
Patient with Ebstein's anomaly of the tricuspid valve, with flow across the superior aspect of the tricuspid valve labeled blue and across the inferior aspect labeled red, so that the abnormal flow in the right ventricle based on portion of tricuspid inflow can be visualized.

One final application that we are increasingly using 4D flow to assess is intraventricular flow dynamics in patients with heart failure or abnormal ventricular loading. While in adult patients, this topic is much more common in those with a structurally normal heart and heart failure from ischemic cardiac disease [14], in pediatric patients many forms of native and palliated congenital heart disease lead to long-term heart failure. Labs have looked at both left and right ventricular mechanics, including in patients with repaired TOF [15] and single ventricle patients [16, 17]. An additional, less studied disease type is patients with Ebstein's anomaly, where marked tricuspid insufficiency results in very abnormal flow patterns in the right ventricle (Figure 23, Clip 9). Performing 4D flow allows visualization of these hemodynamics, which may lead to better understanding of the mechanism of ventricular dilation and dysfunction for many of these patients.

Future directions

One limitation of 4D flow is the long acquisition times required. With the addition of compressed sensing and other image acceleration techniques, data acquisition times continue to shrink, allowing increases in spatial and temporal resolution in the datasets. Many vendors and labs are now working towards a vision of having 4D flow represent a "one stop shop" for congenital cardiac magnetic resonance imaging. One can imagine that if the spatial resolution can be decreased to roughly one millimeter voxels, then full anatomic reconstructions including short axis cine stacks can be extracted from the 4D datasets for analysis. If the temporal resolution can be improved to match current 2D flow methodologies (typically 30 phases per cardiac cycle), and retrospective gating acquisitions are used, then the 4D flow data would obviate the need for additional 2D phase contrast imaging.

Thus, a high spatial and temporal resolution 4D flow dataset would provide all of the anatomic, functional, and flow data on a given patient, without need for acquiring separate double oblique 2D planes. This approach also has the advantage of being much easier for a technologist to acquire, as it is not patient specific / anatomy dependent for accurate image plane set up.

There are, however, several existing challenges to such an approach. Full chest coverage with millimeter voxels requires a large quantity of data, and this is amplified by the desire for high temporal resolution increasing the number of phases. For example, in many adolescent size patients, in order to cover the whole chest in a sagittal geometry with 1 mm slices, 100–150 slices are needed. If temporal resolution of 30 phases per cycle is desired, this will produce between 12,000 and 18,000 images. This vast array of data takes substantial time for reconstruction, made even more computationally demanding when iterative reconstruction is used with compressed sensing. Computational power and processors continue to improve, but most labs that are currently taking this type of approach to 4D flow imaging the reconstruction is done off-line and takes several hours before the data is ready.

Another challenge to this approach to 4D flow imaging is ensuring consistent, uniform signal throughout the study. As discussed above, while 4D flow sequences can be obtained with or without contrast, performing these sequences post-contrast allows increased SNR and CNR as well as higher degrees of parallel imaging acceleration. In the past, blood-pool gadolinium contrast agents such as Gadofosveset trisodium were used in several pediatric labs for performance of contrast enhanced MR angiography and 4D flow imaging [18], but this agent is no longer commercially available in the United States. Another option is non-gadolinium based contrast agents, such as ferumoxytol, which has been used for neonatal and pediatric CMR studies, though our lab does not have personal experience with this approach. Ferumoxytol has a different risk profile than gadolinium based agents, but there is data that for select patient groups these techniques can decrease the need for sedation/anesthesia (which also carries its own inherent risks) [19].

Conclusions

Application of 4D flow imaging to patients with congenital heart disease is an exciting new avenue for greater understanding of patient specific hemodynamics. Both prototype sequences as well as derivations of product pulse sequences allow acquisition of 4D flow datasets, with strengths and weaknesses in each technique. In our lab, we utilize a combination of these sequences, tailored to the individual patient anatomy, size, heart rate, and time limitations on the study. While several third party analysis platforms are available, at the current time the majority of our experience is with the Siemens 4D flow software, and we find that both the 3D visualization and quantification potential on this platform allows comprehensive use of these 4D flow data for our patients.

To access the .avi clips please visit

www.siemens.com/4Dflow

Abbreviations

2D	2-dimensional	**GRAPPA**	Generalized auto-calibrating partially parallel acquisition	**Qp**	Pulmonary blood flow
4D flow	4-dimensional phase contrast imaging			**RPA**	Right pulmonary artery
Ao	Aorta	**IVC**	Inferior vena cava	**PC**	Phase contrast
bpm	Beats per minute	**LPA**	Left pulmonary artery	**TR**	Repetition time
BAV	Bicuspid aortic valve	**MPA**	Main pulmonary artery	**SNR**	Signal to noise ratio
BDG	Bidirectional Glenn	**NSA**	Number of signal averages	**SV**	Single ventricle
CMR	Cardiac magnetic resonance imaging	**PAVM**	Pulmonary arterio-venous malformations	**SVC**	Superior vena cava
				Qs	Systemic blood flow
				TOF	Tetralogy of fallot
CHD	Congenital heart disease			**VENC**	Velocity encoding
FOV	Field of view	**PA**	Pulmonary artery	**TOF**	Tetralogy of fallot
				VENC	Velocity encoding

References

1 P. R. Moran. "A flow velocity zeugmatographic interlace for NMR imaging in humans". Magn Reson Imaging, 1, 197-203, 1982.
2 M. O'Donnell. "NMR blood flow imaging using multiecho, phase contrast sequences". Med Phys, 12, 59-64, 1985.
3 A. J. Powell and T. Geva. "Blood flow measurement by magnetic resonance imaging in congenital heart disease". Pediatr Cardiol, 21, 47-58, 2000.
4 K. K. Whitehead, K. S. Sundareswaran, W. J. Parks, M. A. Harris, A. P. Yoganathan and M. A. Fogel. "Blood flow distribution in a large series of patients having the Fontan operation: a cardiac magnetic resonance velocity mapping study". J Thorac Cardiovasc Surg, 138, 96-102, 2009.
5 C. L. Dumoulin, S. P. Souza, M. F. Walker and W. Wagle. "Three-dimensional phase contrast angiography". Magn Reson Med, 9, 139-149, 1989.
6 H. G. Bogren and M. H. Buonocore. "4D magnetic resonance velocity mapping of blood flow patterns in the aorta in young vs. elderly normal subjects". J Magn Reson Imaging, 10, 861-869, 1999.
7 L. Mirabella, A. J. Barker, N. Saikrishnan, E. R. Coco, D. J. Mangiameli, M. Markl and A. P. Yoganathan. "MRI-based Protocol to Characterize the Relationship Between Bicuspid Aortic Valve Morphology and Hemodynamics". Ann Biomed Eng, 43, 1815-1827, 2015.
8 N. Saikrishnan, L. Mirabella and A. P. Yoganathan. "Bicuspid aortic valves are associated with increased wall and turbulence shear stress levels compared to trileaflet aortic valves". Biomech Model Mechanobiol, 14, 577-588, 2015.
9 Y. Shan, J. Li, Y. Wang, B. Wu, A. J. Barker, M. Markl, C. Wang, X. Wang and X. Shu. "Aortic shear stress in patients with bicuspid aortic valve with stenosis and insufficiency". J Thorac Cardiovasc Surg, 153, 1263-1272 e1261, 2017.
10 J. Geiger, M. Markl, B. Jung, J. Grohmann, B. Stiller, M. Langer and R. Arnold. "4D-MR flow analysis in patients after repair for tetralogy of Fallot". Eur Radiol, 21, 1651-1657, 2011.
11 C. J. Francois, S. Srinivasan, M. L. Schiebler, S. B. Reeder, E. Niespodzany, B. R. Landgraf, O. Wieben and A. Frydrychowicz. "4D cardiovascular magnetic resonance velocity mapping of alterations of right heart flow patterns and main pulmonary artery hemodynamics in tetralogy of Fallot". J Cardiovasc Magn Reson, 14, 16, 2012.
12 D. Hirtler, J. Garcia, A. J. Barker and J. Geiger. "Assessment of intracardiac flow and vorticity in the right heart of patients after repair of tetralogy of Fallot by flow-sensitive 4D MRI". Eur Radiol, 26, 3598-3607, 2016.
13 P. Bachler, I. Valverde, N. Pinochet, S. Nordmeyer, T. Kuehne, G. Crelier, C. Tejos, P. Irarrazaval, P. Beerbaum and S. Uribe. "Caval blood flow distribution in patients with Fontan circulation: quantification by using particle traces from 4D flow MR imaging". Radiology, 267, 67-75, 2013.
14 J. Zajac, J. Eriksson, P. Dyverfeldt, A. F. Bolger, T. Ebbers and C. J. Carlhall. "Turbulent kinetic energy in normal and myopathic left ventricles". J Magn Reson Imaging, 41, 1021-1029, 2015.
15 P. Sjoberg, S. Bidhult, J. Bock, E. Heiberg, H. Arheden, R. Gustafsson, S. Nozohoor and M. Carlsson. "Disturbed left and right ventricular kinetic energy in patients with repaired tetralogy of Fallot: pathophysiological insights using 4D-flow MRI". Eur Radiol, 2018.
16 V. P. Kamphuis, A. A. W. Roest, J. J. M. Westenberg and M. S. M. Elbaz. "Biventricular vortex ring formation corresponds to regions of highest intraventricular viscous energy loss in a Fontan patient: analysis by 4D Flow MRI". Int J Cardiovasc Imaging, 34, 441-442, 2018.
17 J. Wong, R. Chabiniok, S. M. Tibby, K. Pushparajah, E. Sammut, D. S. Celermajer, D. Giese, T. Hussain, G. F. Greil, T. Schaeffter and R. Razavi. "Exploring kinetic energy as a new marker of cardiac function in the single ventricle circulation". J Appl Physiol (1985), 2018.
18 A. Tandon, S. Hashemi, W. J. Parks, M. S. Kelleman, D. Sallee and T. C. Slesnick. "Improved high-resolution pediatric vascular cardiovascular magnetic resonance with gadofosveset-enhanced 3D respiratory navigated, inversion recovery prepared gradient echo readout imaging compared to 3D balanced steady-state free precession readout imaging". J Cardiovasc Magn Reson, 18, 74, 2016.
19 L. M. Lai, J. Y. Cheng, M. T. Alley, T. Zhang, M. Lustig and S. S. Vasanawala. "Feasibility of ferumoxytol-enhanced neonatal and young infant cardiac MRI without general anesthesia". J Magn Reson Imaging, 45, 1407-1418, 2017.

Contact

Timothy C. Slesnick, M.D.
Director, Cardiac MRI
Children's Healthcare of Atlanta
Associate Professor
Department of Pediatrics
Emory University School of Medicine
1405 Clifton Road North East
Atlanta, GA 30322
USA
Tel: +1 404-256-2593
SlesnickT@kidsheart.com

Small Structures, Big Challenges: Fetal Cardiac Magnetic Resonance Imaging

Veronica Bianchi[1]; Jérôme Yerly[1,2]; Jerome Chaptinel[1]; Yvan Mivelaz[3]; Milan Prsa[3]; Leonor Alamo[1]; Chantal Rohner[1]; Jean-Baptiste Ledoux[1,2]; Davide Piccini[1,5]; Chris Roy[1]; Matthias Stuber[1,2]

[1] Department of Radiology, University Hospital (CHUV) and University of Lausanne (UNIL), Lausanne, Switzerland
[2] Center for Biomedical Imaging (CIBM), Lausanne, Switzerland
[3] Department of Pediatrics, University Hospital (CHUV) and University of Lausanne (UNIL), Lausanne, Switzerland
[4] Department of Gynecology-Obstetrics, University Hospital (CHUV) and University of Lausanne (UNIL), Lausanne, Switzerland
[5] Advanced Clinical Imaging Technology, Siemens Healthineers, Lausanne, Switzerland

Introduction

Congenital heart disease (CHD) is the most common birth defect affecting nearly 1% of pregnancies in Europe [1, 2]. Gestational screening has greatly improved antenatal diagnosis of heart malformations and several prenatal interventions now exist to treat CHD in utero, or soon after birth. The timing and type of treatment relies heavily on the ability to accurately visualize a given cardiac malformation. Echocardiography is the gold standard for fetal cardiac imaging [3]. This imaging technique is safe and non-invasive but, despite the progress made in the field of fetal ultrasonography, its quality varies in the presence of maternal obesity, oligohydramnios, multiple gestations, or imaging during late gestation, among other conditions [4]. Since its early applications [5], cardiac magnetic resonance imaging (MRI) has been increasingly investigated for fetal[1] heart imaging in the last decade and has now become an active area of research. A growing number of studies are exploring its applicability in the evaluation of cardiac morphology and function for both normal and abnormal hearts [6–13]. Despite encouraging advances, there remain significant challenges for fetal cardiac MRI, including the small size and the high rate of the fetal heart, the absence of a conventional fetal cardiac gating signal, and the numerous sources of motion artifacts, such as gross fetal movement, and maternal respiration [4]. However, if these challenges can be addressed, it has been shown that MRI has the potential to provide complementary information to echocardiography, improve our ability to monitor CHD diagnosed *in* utero, and better help guide treatments and decision making.

The aim of this project was to develop an MR image acquisition and reconstruction framework that can overcome the aforementioned challenges and visualize the fetal heart with high spatial and temporal resolution [8]. In this article, we describe such an approach, which combines maternal breath-hold, compressed sensing, and self-gating to produce high quality CINE images of the fetal heart. In addition, here we show preliminary results using our reconstruction framework to produce high quality CINE images of the fetal heart. For comparison, we include ultrasound images in the same orientation of those acquired with MR.

Image reconstruction framework

Our reconstruction framework for golden angle radial acquisitions is composed of three main steps. First, intermediate low-resolution images are reconstructed using compressed sensing. Second, an ECG-like self-gating signal is extracted from the intermediate images. Third, the acquired data are reordered into the identified cardiac phases (Fig. 1) [8].

Initially, low spatial and temporal resolution images are reconstructed with a sliding window approach using 15 radial readouts per window and 70% view-sharing, leading to a temporal resolution of 18.5 ms (Fig. 1B). Subsequently, the obtained images are analyzed off-line with a custom-built semi-automatic tool in MATLAB[2] (MathWorks, Natick, MA, USA). The gating signal that reproduces the contraction cycles of the fetal heart is computed by cross-correlating each intermediate frame to a diastolic and a systolic reference image, focusing on a region of interest circumscribed around the fetal heart (Fig. 1C). Finally, and owing to the characteristics that the golden angle acquisition scheme is providing us with,

[1] *Siemens Healthineers disclaimer does not represent the opinion of the authors: MR scanning has not been established as safe for imaging fetuses and infants less than two years of age. The responsible physician must evaluate the benefits of the MR examination compared to those of other imaging procedures.*

[2] *The information shown herein refers to products of 3rd party manufacturers and thus are in their regulatory responsibility. Please contact the 3rd party manufacturer for further information.*

the radial readouts are retrospectively binned into different cardiac phases (Fig. 1D) with a bin width of 25 ms and a view-sharing equal to 50%, improving the temporal resolution to 12.5 ms. Both intermediate and retro-gated images are reconstructed using an in-house script implementing a *k-t* sparse SENSE algorithm model [14].

Image acquisition and analysis

To validate the proposed framework, six pregnant patients (gestational age 29.7 ± 2.1 weeks at the time of the MRI exam) with a suspicion of fetal non-cardiac pathology were recruited to undergo both MRI and fetal echocardiography. Written informed consent, according to the recommendations of the local ethics committee, was obtained from all subjects prior to examination.

MR acquisition was performed on a 1.5T clinical MR scanner (MAGNETOM Aera, Siemens Healthcare, Erlangen, Germany) with a 32-channel spine coil and an 18-channel body array coil for signal measurement. Data were collected under maternal breath-hold with a prototype radial golden angle bSSFP sequence (Fig. 1A) and acquisition parameters are summarized in Table 1 [8]. For each patient, three standard views (four-chamber, three-vessel and short-axis view), that are routinely targeted in the clinical fetal echocardiographic examination, were acquired (Fig. 2) in 20.1 s each. Echocardiographic images were acquired on a Voluson E8 Expert or Voluson E10 (GE Healthcare, Waukesha, WI, USA)

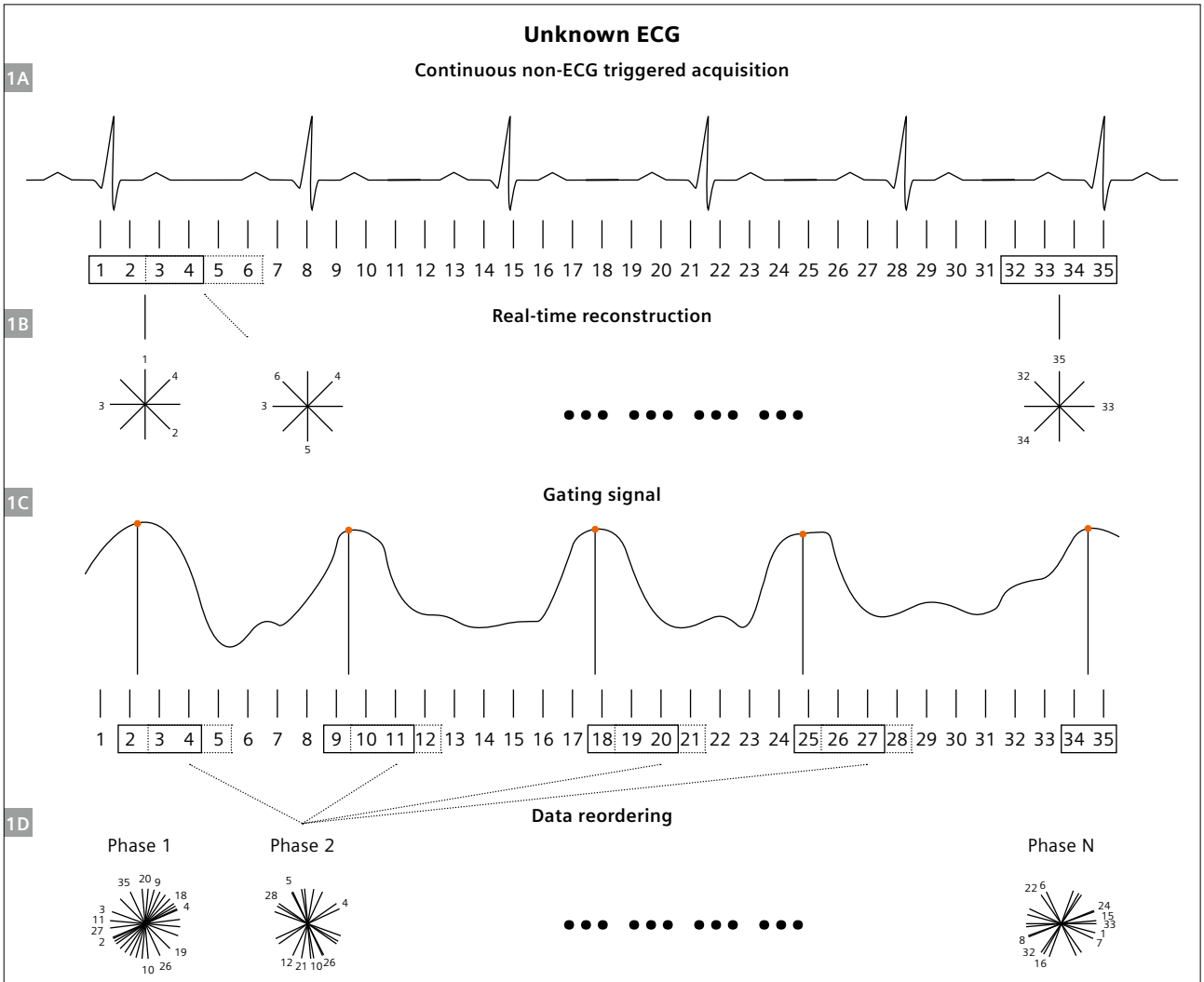

Figure 1:
Schematic overview of the MRI acquisition and reconstruction framework. The data, acquired with a golden angle continuous acquisition technique **(1A)**, were reconstructed applying a sliding window binning **(1B)** and intermediate images were obtained. The low-resolution images were subsequently analyzed to extract an ECG-like gating signal that represents the contraction cycles of the fetal heart **(1C)**. The self-gating signal was then used to retrospectively bin the radial data in different cardiac phases during which they were acquired **(1D)**. *(Figure adapted from Chaptinel et al. [8], with permission according to https://creativecommons.org/licenses/by/4.0/).*

Parameter	Value
Field-of-view	260 x 260 mm²
Base resolution	256 x 256 pixels
Pixel size	1.0 x 1.0 mm²
Slice thickness	4.0 mm
TE/TR	1.99/4.1 ms
RF excitation angle	70°
Slices	3
Shot per slice	1
Radial readouts per slice	1600
Acquisition time per slice	6.7 s
Bandwidth	1028 Hz/pixel
Reconstructed temporal resolution	12.5 ms (shared phases)

Table 1: Values of the MR acquisition parameters.

with the RM6C 3D/4D curved array transducer with a frequency comprised in the range 1.0–7.0 MHz. Finally, MR and echocardiographic images were qualitatively and quantitatively compared to demonstrate the capability of both imaging techniques to visualize and measure heart structures. Two experienced pediatric cardiologists visually evaluated the quality of the images obtained with both modalities. Subsequently, they measured the diameter of aorta, main pulmonary artery, mitral valve annulus and tricuspid valve annulus using ClearCanvas (Synaptive Medical, Toronto, Canada) on both MR and echocardiographic images for each patient.

Results and discussion

MR images were successfully acquired on all patients. Figure 3 shows an example of fetal heart images in a 4-chamber (Fig. 3A), a short-axis (Fig. 3B) and a three vessel view (Fig. 3C) acquired in a 31-week-old fetus. MR images (columns on the left) are visually compared to the images obtained with the gold standard, echocar-

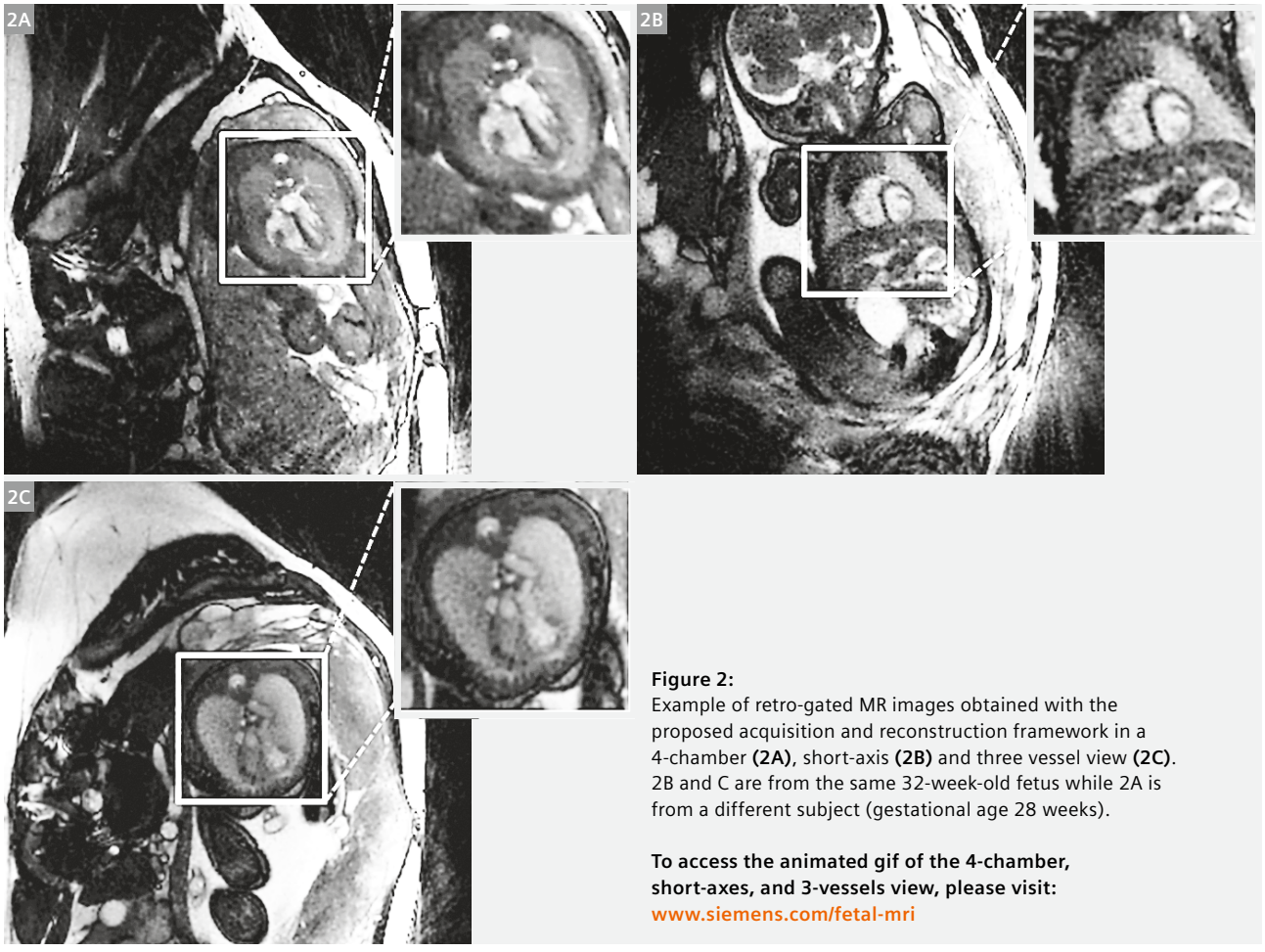

Figure 2:
Example of retro-gated MR images obtained with the proposed acquisition and reconstruction framework in a 4-chamber **(2A)**, short-axis **(2B)** and three vessel view **(2C)**. 2B and C are from the same 32-week-old fetus while 2A is from a different subject (gestational age 28 weeks).

To access the animated gif of the 4-chamber, short-axes, and 3-vessels view, please visit:
www.siemens.com/fetal-mri

diography (column on the right). The two imaging techniques proved to be comparable in terms of qualitative visualization of cardiac structures. The overall MR image quality was considered satisfying to perform quantitative measurements for all patients except for one in which the mitral valve and the tricuspid valve were not clearly recognizable. Moreover, one patient was excluded from the quantitative comparison because the echocardiographic images were not compatible with the software used for the analysis. Therefore, the diameter of aorta and main pulmonary artery were measured in five patients, while instead mitral valve annulus and tricuspid valve annulus were measured on the images of four patients. As shown in Figure 4, the quantitative measurements performed on the MR images are in good agreement with the measurements by

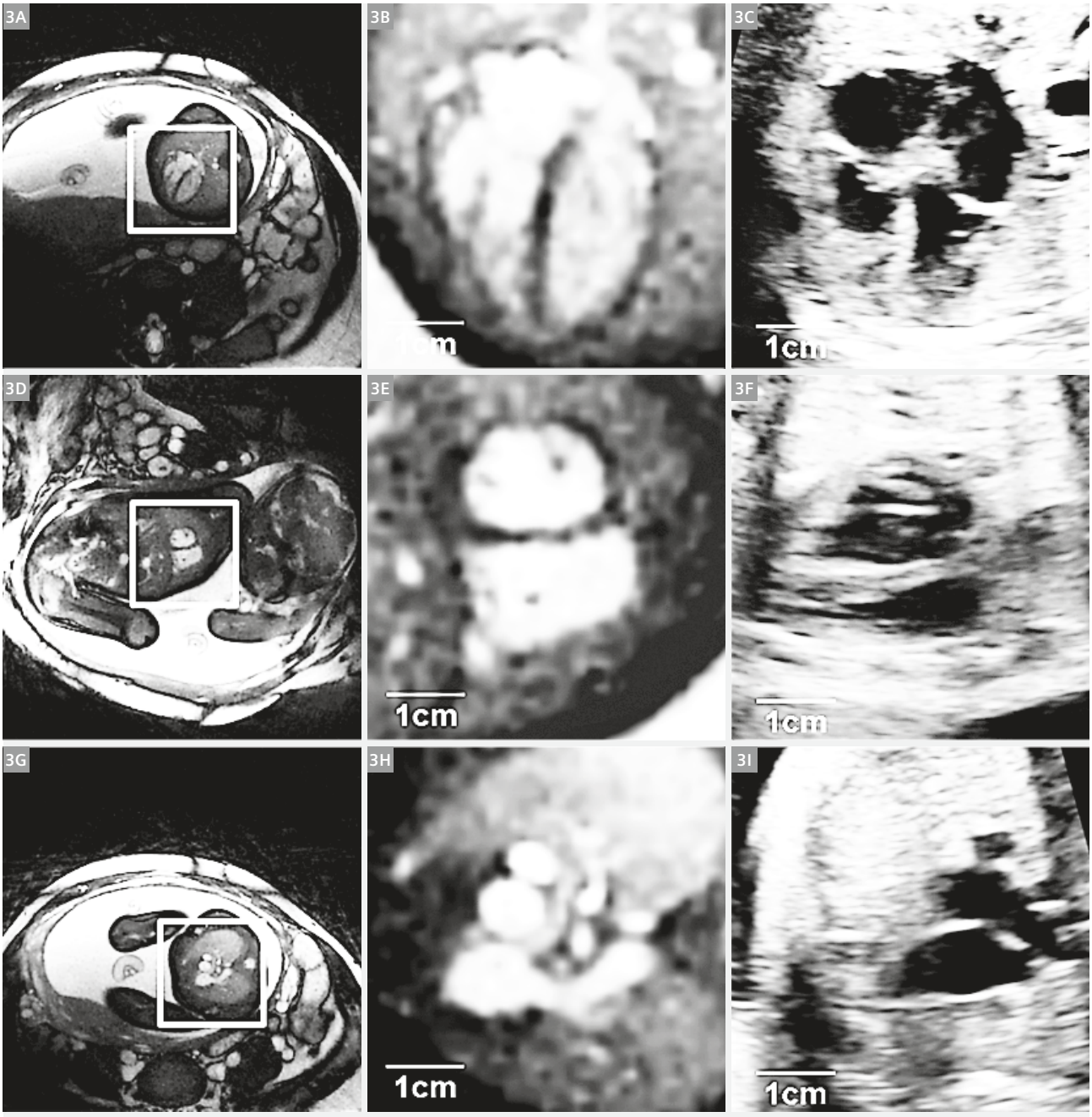

Figure 3:
Comparison between MR and echo images in 4-chamber **(3A–C)**, short-axis **(3D–F)** and three vessel view **(3G–I)** from one of the patient. *(Figure adapted from Chaptinel et al. [8] with permission according to https://creativecommons.org/licenses/by/4.0/).*

echocardiography. This study demonstrated that MRI is a promising technique for acquiring high spatial and high temporal resolution images of the fetal heart, and that it is critically enabled by advanced acquisition and reconstruction schemes that have recently been developed. These include golden angle acquisition, self-gating that obviates the need for an ECG, and compressed sensing reconstruction. Preliminary results show the potential of our acquisition and reconstruction framework for the visualization and measurement of normal fetal cardiac structures. MRI could offer a reliable easily repeatable and safe complementary imaging modality for patients in whom echocardiography is inconclusive. Further study is now required to assess the diagnostic capability of fetal cardiac MRI in the presence of cardiac abnormalities.

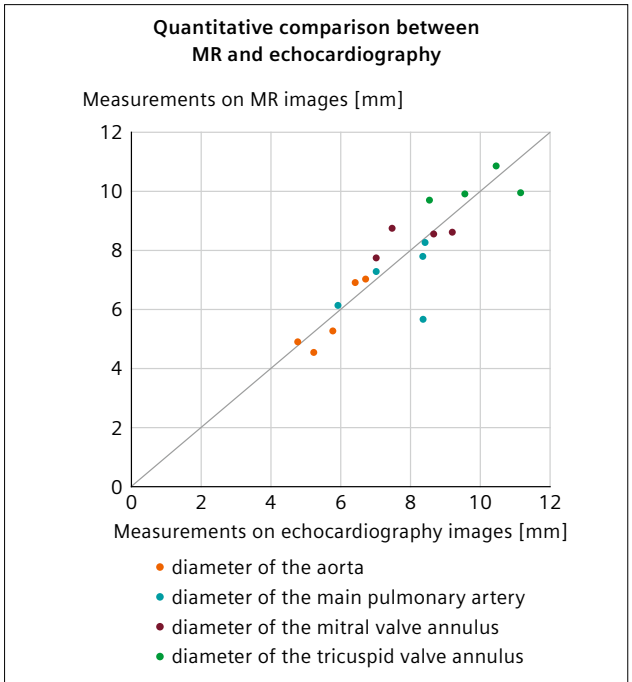

Figure 4:
Comparison between quantitative measurements performed on MR and echocardiographic images of normal fetal hearts. The graph shows the average values of the measurements performed by two pediatric cardiologists on the best-quality image for each methodology. The diameter of aorta and main pulmonary artery were measured on five fetal patients, while the mitral valve annulus and the tricuspid valve annulus were quantified for four fetal patients.

Contact

Prof. Matthias Stuber
Center for BioMedical Imaging (CIBM)
Centre Hospitalier Universitaire Vaudois (CHUV)
Rue de Bugnon 46, BH 8.80
1011 Lausanne
Switzerland
Matthias.stuber@chuv.ch

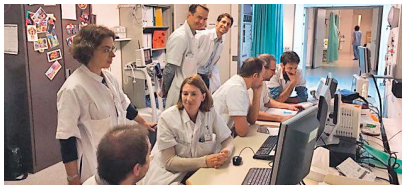

References:

1 Dolk H, Loane M, Garne E, for the European Surveillance of Congenital Anomalies (EUROCAT) Working Group. Congenital heart defects in Europe: prevalence and perinatal mortality, 2000 to 2005. Circulation 2011; 123:841–9.
2 EUROCAT Access Prevalence Tables. Available at: http://www.eurocatnetwork.eu/ACCESSPREVALENCEDATA/PrevalenceTables. Accessed September 11, 2018.
3 Donofrio MT, Moon-Grady AJ, Hornberger LK, et al. Diagnosis and treatment of fetal cardiac disease: A scientific statement from the american heart association. Circulation 2014; 129:2183–2242. doi: 10.1161/01.cir.0000437597.44550.5d.
4 Wielandner A, Mlczoch E, Prayer D, Berger-Kulemann V. Potential of magnetic resonance for imaging the fetal heart. Seminars in fetal & neonatal medicine 2013; 18(5):286-297.
5 Meyer-Wittkopf M, Cook A, McLennan A, Summers P, Sharland GK, Maxwell DJ. Evaluation of three-dimensional ultrasonography and magnetic resonance imaging in assessment of congenital heart anomalies in fetal cardiac specimens. Ultrasound Obstet Gynecol 1996; 8(5):303–8. doi: 10.1046/j.1469-0705.1996.08050303.x.
6 Votino C, Jani J, Damry N, Dessy H, Kang X, Cos T, Divano L, Foulon W, De Mey J, Cannie M. Magnetic resonance imaging in the normal fetal heart and in congenital heart disease. Ultrasound Obstet Gynecol 2012; 39(3):322-329. doi: 10.1002/uog.10061.
7 Manganaro L, Savelli S, Di Maurizio M, et al. Assessment of congenital heart disease (CHD): Is there a role for fetal magnetic resonance imaging (MRI)? Eur J Radiol 2009; 72:172-180. doi: 10.1016/j.ejrad.2008.06.016.
8 Chaptinel J, Yerly J, Mivelaz Y, Prsa M, Alamo L, Vial Y, Berchier G, Rohner C, Gudinchet F Stuber M. Fetal cardiac cine magnetic resonance imaging in utero. Sci Rep 2017; 7(1):15540. doi: 10.1038/s41598-017-15701-1.
9 Gorincour G, Bourliere-Najean B, Bonello B, Fraisse A, Philip N, Potier A, Kreitmann B, Petit P. Feasibility of fetal cardiac magnetic resonance imaging: preliminary experience. Ultrasound Obstet Gynecol 2007; 29:105-108. doi: 10.1002/uog.3924.
10 Tsuritani M, Morita Y, Miyoshi T, Kurosaki K, Yoshimatsu J. Fetal Cardiac Functional Assessment by Fetal Heart Magnetic Resonance Imaging. J Comput Assist Tomogr 2018; 00:00–00. doi: 10.1097/RCT.0000000000000781.
11 Roy CW, Seed M, Kingdom JC, Macgowan CK. Motion compensated cine CMR of the fetal heart using radial undersampling and compressed sensing. J Cardiovasc Magn Reson 2017;19:1–14. doi: 10.1186/s12968-017-0346-6.
12 Amerom JFP, Lloyd DFA, Murgasova K, et al. King's Research Portal Fetal Cardiac Cine Imaging Using Highly Accelerated Dynamic MRI with Retrospective Motion Correction and Outlier Rejection. doi: 10.1002/mrm.26686.
13 Haris K, Hedström E, Bidhult S, et al. Self-gated fetal cardiac MRI with tiny golden angle iGRASP: A feasibility study. J Magn Reson Imaging 2017 doi: 10.1002/jmri.25599.
14 Yerly J, Ginami G, Nordio G, Coristine AJ, Coppo S, Monney P, Stuber M. Coronary endothelial function assessment using self-gated cardiac cine MRI and k-t sparse SENSE. Magn Reson Med 2016; 76:1443–1454. doi: 10.1002/mrm.26050.

n° 31

AN EXTRAORDINARY VOYAGE IN THE CITY OF JULES VERNES

AUGUST 28th - 30th

SMRA

Nantes France 2019

The Society for Magnetic Resonance Angiography, founded in 1989 to bring together scientists, clinicians and industry experts, is widely recognized as the sole international conference exclusively devoted to MR angiography.

SMRA 2019 Workshop Topics

- Vascular disease mechanisms
- Vessel wall plaque and thrombus imaging
- Quantification of blood flow dynamics
- Vessel lumen imaging
- Contrast agents
- MRA of the brain, neck, heart, aorta, abdomen and extremities
- Artificial Intelligence in MRA
- Cardiac MR, assessment of cardiac structure and function
- Clinical studies and study design
- Future perspectives and new MRA techniques
- Comparing MRI with other imaging modalities

Venue

La Cité des Congrès de Nantes
5 Rue de Valmy, 44000 Nantes, France

Pre-Conference Educational Workshop

CME accreditation will be available for all attendees. The education workshop will include presentation by international experts in the field of MRA techniques and application covering the following areas: Basic MRA methods and techniques, contrast enhanced MRA, MRA of the head, neck, peripheral arteries, and cardiovascular system.

31st Annual Conference Organizers

Hosts: Jean-Michel Serfaty and Philippe Douek
President: Michael Markl

Magnetic Resonance Angiography

society4mra.org

Pre-conference
Educational workshop
August 27th

3D Localization for Cardiac Views: Saving Time While Increasing Accuracy

Julian Gan

Head of Product & Clinical Imaging, Siemens Healthineers, Singapore

2D single-slice scans in a variety of anatomical planes are the mainstay of cardiac functional and flow imaging. This requires fast and accurate planning. However, localization of cardiac views can be difficult in cases of deviant anatomy.

'Standard' cardiac views for the left ventricle (LV) typically comprise 2-chamber, 3-chamber, 4-chamber, short-axis (SAX) views, or coronal LVOT. Right ventricle (RV) views typically comprise RVOT and RV 2-chamber views.

Other common views are the main pulmonary artery, aortic arch 'candy cane', en face views of the aortic / mitral / tricuspid / pulmonary valve for function, or just distal to the valve leaflets for flow measurements.

More esoteric views might include, e.g., right and left pulmonary artery, coronary sinus, the right and left superior / inferior pulmonary veins, as well as SVC and IVC view of the right atrium etc. In cases of pathology, patient-specific custom views might be required to visualize abnormal flow due to shunts, defects, or stenosis.

Current planning tools

1. Multiple 2D single-shot localizers. A 'pseudo' or close approximation view is obtained, and planning is then iteratively refined using the most recent cine view. However, multiple breath-holds are required for each localizer; inconsistent breath-holding can result in slices becoming incongruent. Also, as planning is prospective, it is always necessary to wait for the latest image, which may be inefficient.

2. 3-point localizer tool. This assumes that the point selected is actually the optimum location – which may not be the case if there is no stack of 2D or 3D images to choose. Furthermore, tortuous anatomy may necessitate some compromise for all structures to be seen, e.g., the optimum plane showing the ascending arch and descending aorta in its entirety (the candy cane view) may not pass through the exact center of the vessel.

3. Specialized software such as the Cardiac Dot Engine. Through training and recognition of landmarks, this will automatically and consistently localize the 2C , 3C, 4C, and SAX views after the acquisition of an 'AA scout'. However, automatic alignment for other specialized views is not yet available. This software is licensed and is not available on older software platforms such as VA, VB, and VC lines.

3D localization technique

An alternative method of localizing cardiac views involves the use of 3D Task Card to generate MPR images, which are then imported back onto the Exam Task Card to copy the center slice location.

1. The only images required are a stack of triggered single-shot images in breath-hold. TrueFISP bright blood or HASTE dark blood anatomical datasets are fine, and are typically routinely acquired anyway.

The recommended orientation is axial, leaving no gap. According to the standard triggered trufisp_single-shot_tra protocol in the Siemens-Heart-Morphology, the only modifications are to:

- set **Distance Factor = 0**, and a slice thickness of **6–8 mm**, which should allow coverage of the heart to the aortic arch in about 25 slices. For pediatric cases, slice thickness should be reduced to 4–5 mm.
- **Geometry = Ascending** is preferred, so that the more critical slices covering the heart are acquired first, in case the patient's breath-hold capability deteriorates midway through the measurement.
- **Cardiac Shim** (optional for 1.5T, mandatory for 3T). The green shim volume box should be positioned over the heart.
- **Capture Cycle** ensures that acquisition is conducted in the diastolic window.
- **Properties** – Auto Open Inline Display is also helpful for monitoring the acquisition and obtaining a real-time overview of the cardiac anatomy.

2. Load the dataset onto 3D Task Card. The stack of gapless 2D single-shot images is sufficient to visualize most cardiac anatomy in mult planar images with acceptable resolution. The orientation of the MPR lines can be set to obtain the desired views (as described later). Either click the quick 'Save' button (all images are put into an MPR Series), or the 'Save As' button to give the MPR series a unique name (this could be helpful to avoid mix-up, e.g., if doing across section of the right and left pulmonary arteries).

3. Drag and drop the newly created MPR series from the browser, directly into the GSP (it may also be loaded onto the stamp segment for quick access).

Open the Cine scan for planning:

- Right click – **Copy Image Position** on the MPR image to inherit that exact image position.
- If **Lock rotation** is enabled (within the Phase Encode '...' Properties), the scan will automatically be inplane rotated to be parallel to the posterior of the patient. This works well for transverse or sagittal oblique scans. For coronal LVOT scans, a manual rotation may be preferred.

To avoid misalignment:

- The Cine scan must be conducted in the same respiration state as the trufisp_tra series. Expiration is recommended for consistency.
- Do not use REF mode. The Cine scan must either be in **ISO mode**, or FIX for the same table position as the TrueFISP tra series.

An effective way of doing this is to ensure that the table is always centered correctly from the very beginning, and then to keep all protocols saved with FIX = H0.

4. Press the Scan button to apply this sequence. A copy will automatically be appended and opened ready for another immediate Copy Image Position on the next MPR view. In this way, all the Cine scans can be quickly queued up and ready to go. The acquired Cine should match very closely with the predicted MPR image (Figs. 1 and 2). Further corrections and tweaking on the newly acquired Cines are generally not required.

This technique is not exclusive to single-slice scans, of course – a 3D slab or 2D stack (odd-numbered) could also benefit from using the Copy Image Position of an MPR image to quickly inherit the center slice location.

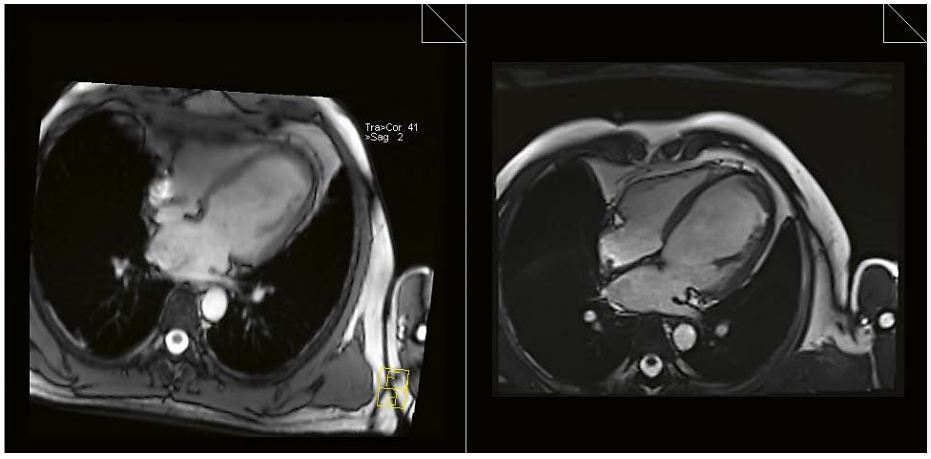

Figure 1:
MPR image (left) and actual Cine (right) of the 4-chamber view showing an identical anatomic view. The auto inplane rotation feature has optimally aligned the FOV to the patient's back, and previewing the actual image has allowed aggressive setting of the rFOV to shorten breath-hold time.

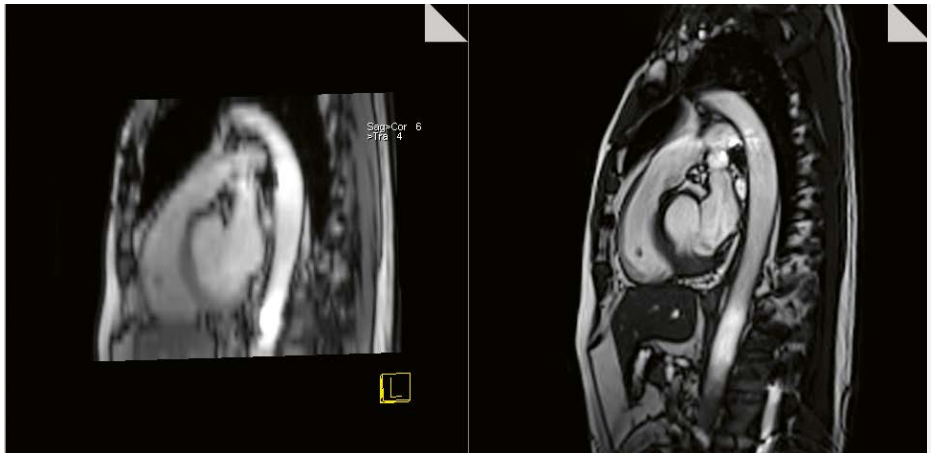

Figure 2:
MPR image (left) and actual Cine (right) of the RVOT showing an identical anatomic view.

Localizing of the common left lentricular (LV) views: 2C, 3C, 4C, SAX, LVOT

As the planning sequence is nearly identical to the traditional method using 2D localizers, no additional learning effort is required.

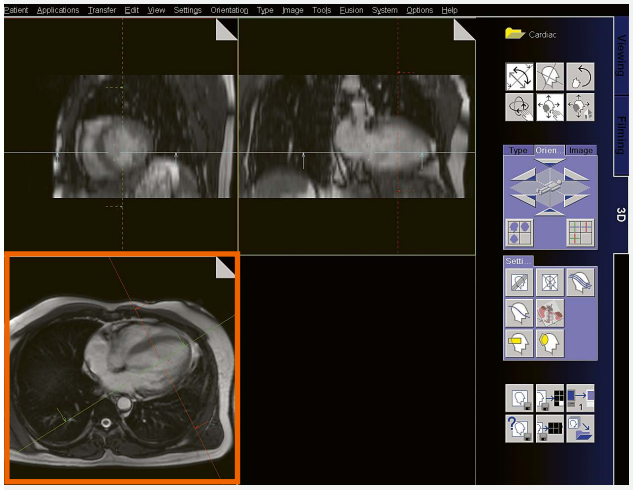

Figure 3:
Step 1: Start with the true axial in the bottom left, and align the long axis (green) roughly from middle of mitral valve to apex. Align the other axis (red) perpendicularly.

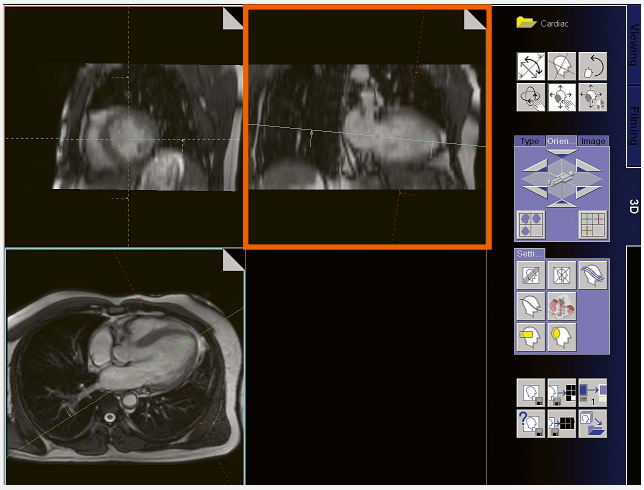

Figure 4:
Step 2: Moving anti-clockwise to the upper right image (pseudo 2C view): Align the long axis (blue) from mitral valve to apex. Align the other axis (red) perpendicularly.

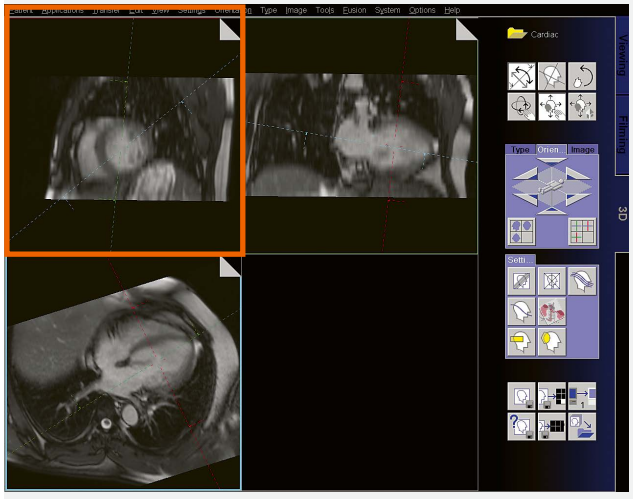

Figure 5:
Step 3: Moving anti-clockwise to the upper left image (SAX view), align the 2C orientation (green line) parallel to the RV insertion points, and the 4C orientation (blue line) passing through the apex. Iteratively make fine adjustments on all segments to further correct the 2C, 4C, and SAX orientations, until the localization is perfect. Highlight each desired segment and click 'Save' or 'Save As'.

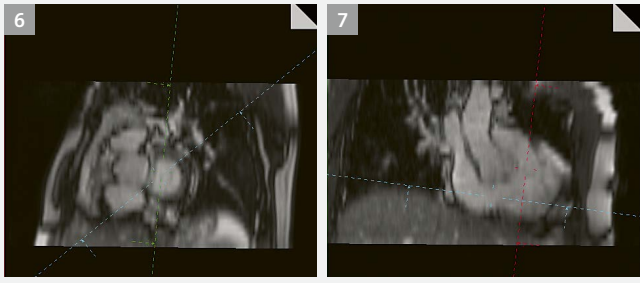

Note that one may obtain more accurate 4C orientation by:
a) scrolling to a more basal SAX slice and checking that the slice does not cut into the outflow tract. Adjusting the angulation allows to dynamically check the resulting 4C view to ensure that the septum is clear (Fig. 6).
b) moving the 2C line (green) over to the RV, thereby obtaining the RV 2 chamber view, and checking that the slice passes through the middle of the tricuspid valve (Fig. 7).

Figure 6:
Basal short axis slice to check the outflow tract.

Figure 7:
RV 2-chamber view, to show the tricuspid valve and RV inflow and outflow tracts.

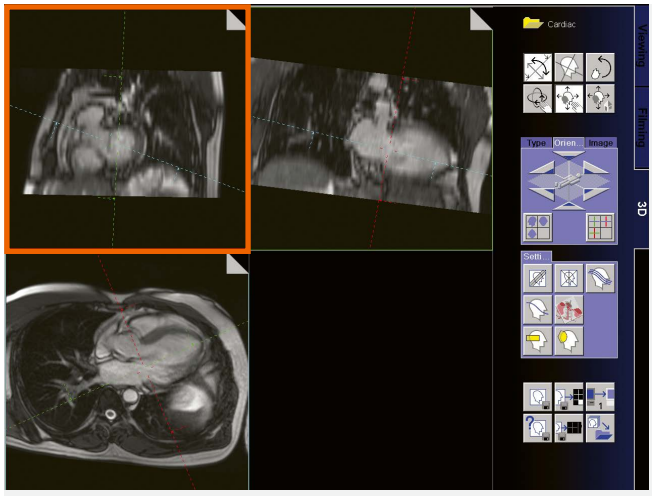

Figure 8:
Step 4: Scroll the SAX series to a basal SAX slice, and align either the blue or the green long-axis line through the LVOT to obtain the 3-chamber view.

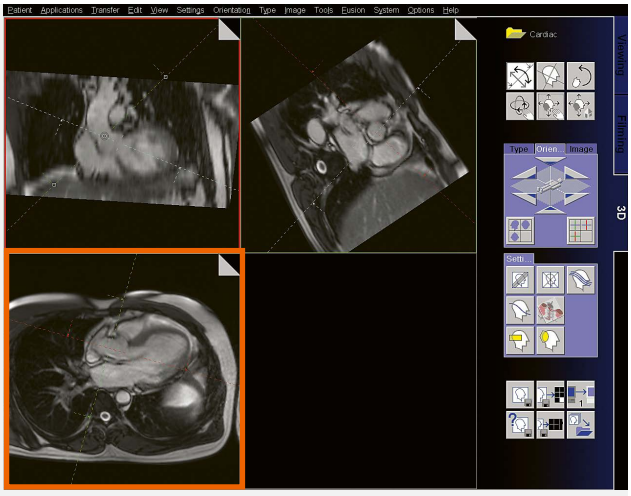

Figure 9:
Step 5: Aligning a long-axis slice through the LVOT on the 3-chamber view (bottom left) will obtain the coronal LVOT projection (top left). At the same time, the en face aortic valve view can be planned by placing the cross-sectional lines perpendicularly, on both orthogonal views. It can be confirmed on the resultant view that the vessel appears circular (top right). Of course, on a static single-shot, the movement of the valve leaflets cannot be seen; thus a long-axis Cine acquistion is required for accurate prescription of the valve view.

Localizing the RVOT

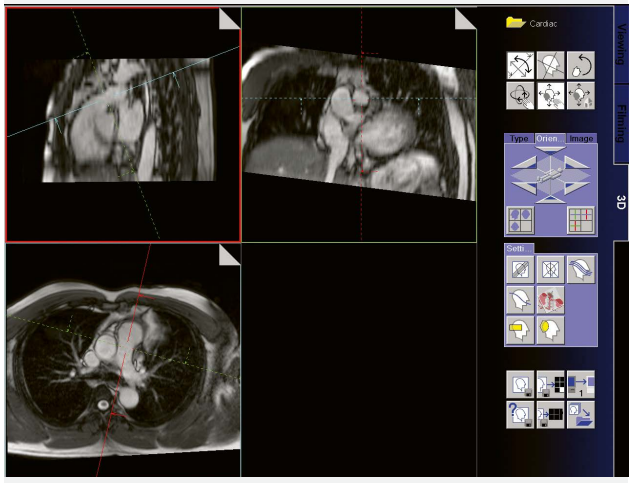

Figure 10:
Click on the Reset Orientation icon to return to the initial straight MPR views. On the axial MPR (bottom left), locate the main pulmonary artery. Angle the sagittal (red) line along the MPA, and the other line perpendicularly. On the resultant pseudo RVOT (top left), angle the coronal (blue) line along the RVOT, and the other line perpendicularly. The sagittal red line can now be adjusted and rotated to optimize the degree of RV vs. RVOT visualization, and previewed accordingly. The en face pulmonary valve view can also be checked.

Localizing the pulmonary arteries

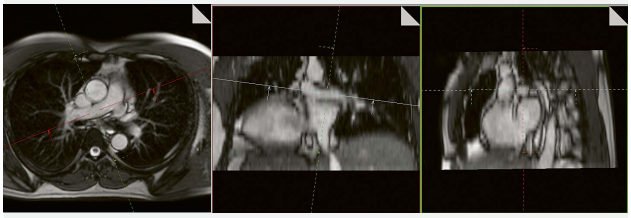

Figure 11:
Right PA – On the axial MPR, look for the right pulmonary artery branch and angle the long- and short-axis lines accordingly. Do the same on the resulting orthogonal long axis view. The en face RPA view can be directly copied for through-plane flow studies, without further localization scans.

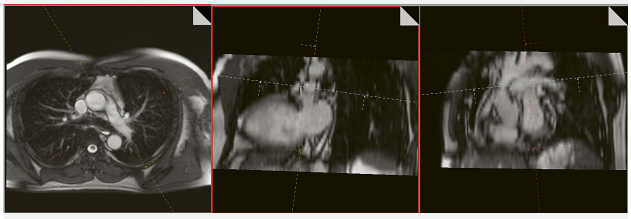

Figure 12:
Left PA – On the axial MPR, look for the left pulmonary artery branch, and angle the long- and short-axis lines accordingly. Do the same on the resulting orthogonal long axis view. As there is usually only a narrow space between the main LPA and further branches, previewing the circular en face projection allows accurate prescription for through-plane flow studies.

Localizing the coronary sinus

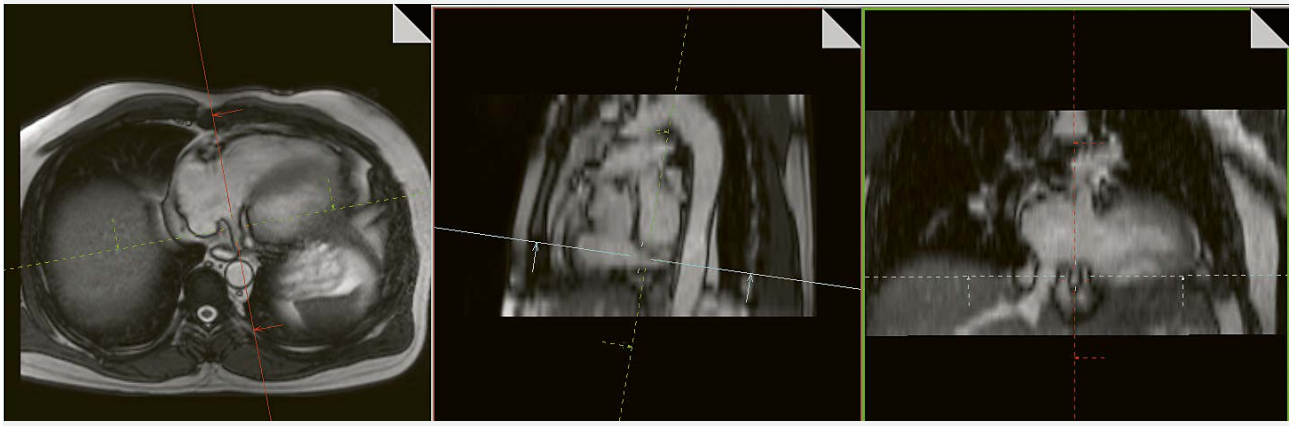

Figure 13:
Coronary Sinus – Starting from the axial MPR, examine the right atrium for the coronary sinus and angle the long and short-axis lines accordingly. Do the same on the resulting orthogonal long-axis view.

Localizing the SVC and IVC

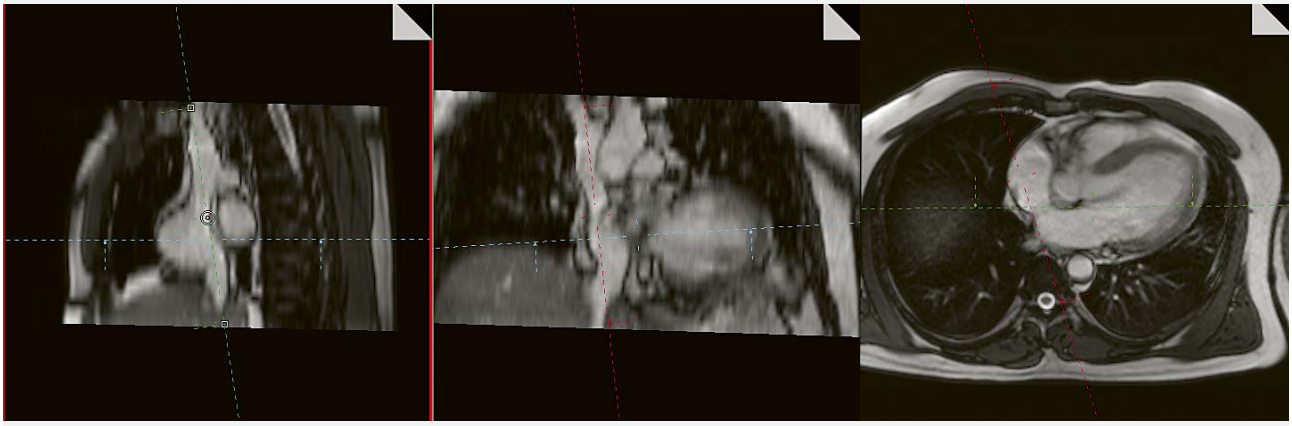

Figure 14:
SVC and IVC. Starting from the sagial MPR, examine the right atrium for the opening of the IVC and SVC and angle the coronal long-axis line along both. On the resultant coronal MPR, adjust the sagittal MPR line to pass through the IVC and SVC. Check the preview and make fine adjustments accordingly.

Localizing the pulmonary veins

Figure 15:
Right superior PV. The four pulmonary veins are distinct, yet in close proximity. Careful scrolling of the axial MPR stack can distinguish the individual vessels.

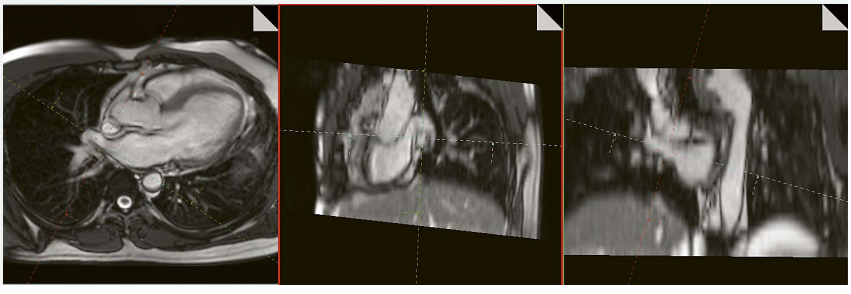

Figure 16:
Right inferior PV. Usually easy to locate due posterior direction.

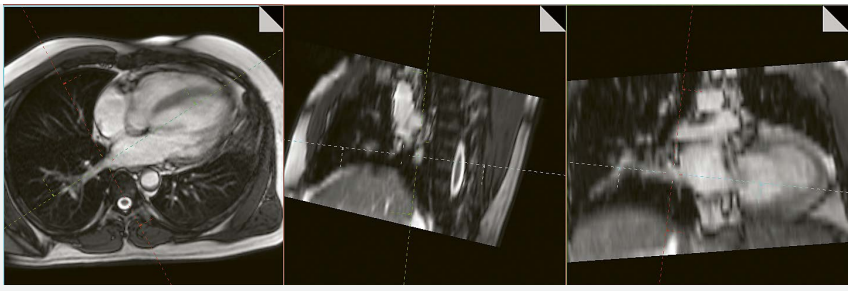

Figure 17:
Left superior PV. Can be difficult to locate due to the presence of many vessels above and below.

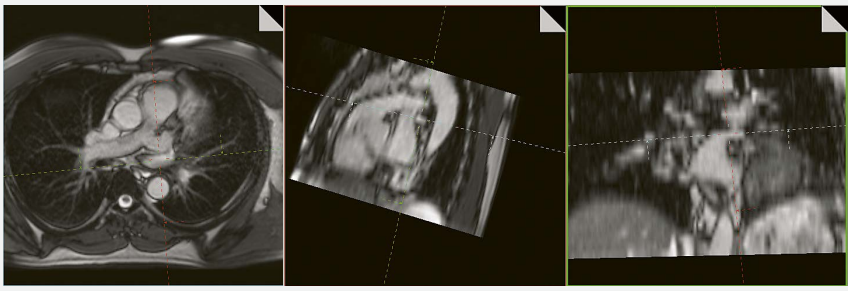

Figure 18:
Left inferior PV. Usually easy to locate due posterior direction.

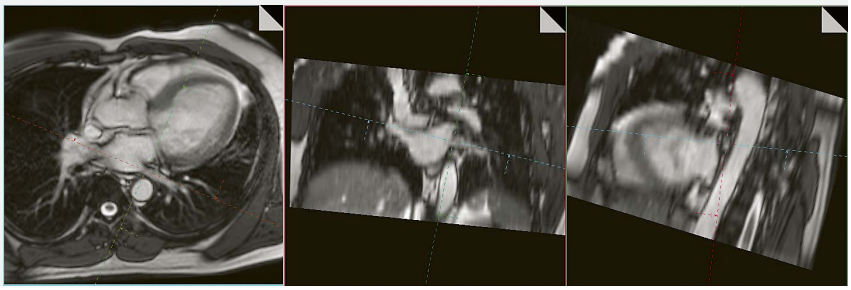

Summary

The 3D Localization technique is an efficient and reliable way to localize cardiac views, especially in unfamiliar anatomical territory e.g. complex cardiomyopathies, post-surgical changes, or animal scans. For new trainees, the ability to visualize anatomy in 3D also promotes a better understanding and appreciation of the required angulations.

The unique advantages are:

- Time saving. It uses the same stack of transverse single-shot TrueFISP or HASTE_db images, which is usually routinely acquired for every examination. No additional 2D localizers are required, thus fewer breath-holds for the patient.
- Higher accuracy from the beginning, due to the benefit of visualizing all other planes. This avoids the initial pseudo or approximation views.
- Reliability and consistency, due to the ability to preview the exact appearance of the projection. This is useful, for example to avoid the aortic outflow tract appearing on the 4C view, or to adjust the appearance of the RVOT and pulmonary valve. It also allows optimization of the rFOV to shorten scan time or avoid aliasing without guesswork or test scans.
- Allows multi-tasking. Since planning is done retrospectively in the 3D Task Card, this can be done while other scans are running. If an MRWP console is available, another person could perform the planning simultaneously (e.g., in complex cases) – saved MPR images will be automatically available on the AWP for the operator.

Contact

Julian Gan
Head of Product & Clinical Imaging
Siemens Healthineers
Singapore
Tel.: +65 8123 4341
Julian.Gan@Siemens-Healthineers.com

The Various Definitions of TR

Gary R. McNeal, MS (BME)

Cardiovascular MR R&D Team, Siemens Healthineers, Chicago, IL, USA

Introduction

In the practice of Cardiac MRI, various definitions of the parameter TR (Time of Repetition) have evolved as gated pulse sequence have become increasingly complex. Understandably this causes significant confusion among most users. In some cases, the original concept of TR seems to be lost. This article describes the various definitions of TR.

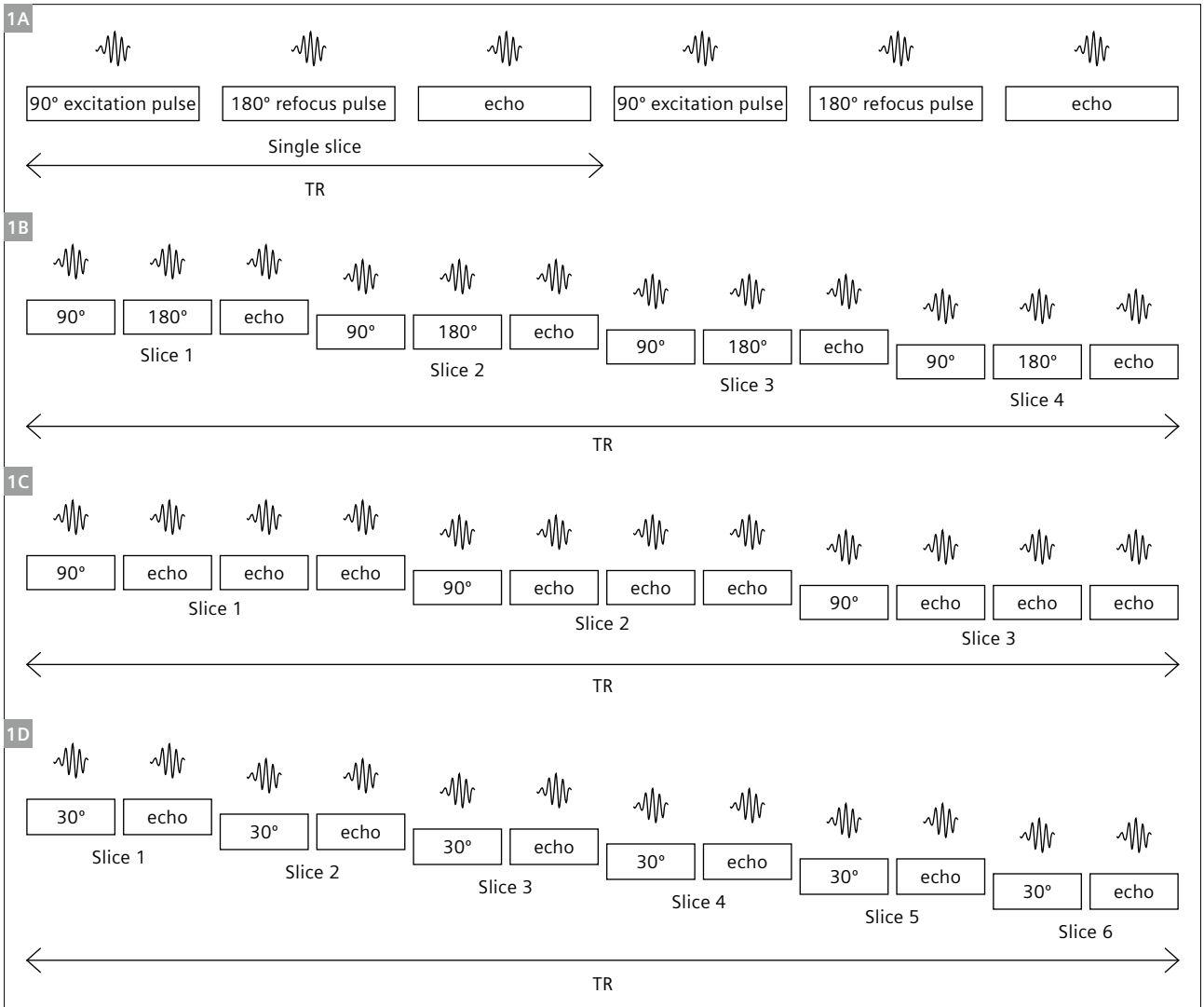

Figure 1:
1A: Single-slice Spin Echo pulse sequence.
1B: Multi-slice Spin Echo pulse sequence.
1C: Multi-slice Turbo Spin Echo pulse sequence.
1D: Multi-slice Gradient Recalled Echo pulse sequence.

Definition 1

The conventional definition of TR is the repetition time between successive excitation pulses for the same slice. This is demonstrated by a single-slice Spin Echo (SE) pulse sequence in which each slice consists of a 90° excitation pulse, a refocusing pulse, and an echo (Fig. 1A).

This conventional definition of TR also applies to a multi-slice SE pulse sequence in which as many slices as possible are interleaved within the selected TR (Fig. 1B). For T1 weighting we typically select a relatively short TR (< 1000 ms),or for T2 weighting a relatively long TR (> 2000 ms).

This conventional definition of TR also applies to a multi-slice Turbo Spin Echo (TSE) pulse sequence in which each slice consists of a single excitation pulse with multiple refocusing pulses and multiple echoes (Fig. 1C). Since there are more echoes per slice, a TSE sequence requires fewer repetitions than a SE sequence with the same TR, but accordingly fewer slices may be acquired within the selected TR.

This conventional definition of TR also applies to a multi-slice Gradient Recalled Echo (GRE) pulse sequence which contains no refocusing pulses at all (Fig. 1D). Each slice consists of a single excitation pulse and a series of gradient reversals to form an echo. TR is defined as the time between successive excitation pulses for the same slice in a GRE sequence, just like in SE and TSE sequences.

Definition 2

When a pulse sequence is cardiac triggered, the definition of TR can become a bit more complicated. Often the TR displayed in the user interface does not reflect the conventional definition of TR, but instead is used to define some other aspect of sequence timing relative to the cardiac cycle. In the discussion that follows, the TR displayed to the user will be denoted $TR_{protocol}$, while the effective TR, defined conventionally as the time between successive excitation pulses, will be indicated as $TR_{effective}$.

When cardiac triggering is used in a multi-slice spin-echo sequence, the $TR_{effective}$, according to the conventional definition, is the repetition time between successive heartbeats. This is demonstrated by a cardiac triggered multi-slice SE pulse sequence (Figure 2A), but may apply as well to multi-slice TSE and GRE pulse sequences. Each slice is excited only once per heartbeat, so $TR_{effective}$ equals the R-R interval. As the heart-rate increases, the $TR_{effective}$ decreases because the R-R interval decreases. Since each slice is acquired at a different phase of the cardiac cycle, this technique is often called a multi-slice multi-phase cardiac triggered pulse sequence. On the other hand, $TR_{protocol}$ for such a sequence is defined as the time actually used to acquire all the slices within the cardiac cycle.

A common method to increase the $TR_{effective}$ is to trigger the pulse sequence on every second or third heartbeat (Fig. 2B), in which case $TR_{effective}$ is twice or three times the R-R interval. This strategy is often used to control the image contrast for T2-weighted or IR-weighted pulse sequences.

Definition 3

Cardiac triggered cine pulse sequences create a movie effect of the beating heart or flowing blood by acquiring a series of images at different phases throughout the cardiac cycle. Various types of cine techniques include TrueFISP, Flash, Phase Contrast, and Grid-Tagging pulse sequences. The $TR_{protocol}$ definition for a cine sequence is the repetition time between consecutive cardiac phases, also known as the Temporal Resolution of the sequence. This definition of TR is demonstrated by a simple cardiac triggered cine pulse sequence (Fig. 3A), in which only one echo is acquired per cardiac phase (non-segmented). In this non-segmented acquisition, the $TR_{protocol}$ represents both the repetition time between successive cardiac phases (Temporal Resolution) and the repetition time between successive excitation pulses ($TR_{effective}$).

Often, however, multiple echoes are acquired per cardiac phase to reduce the required number of repetitions (Fig. 3B), a scheme called “segmented” data collection. In a segmented cine pulse sequence the $TR_{protocol}$ represents the repetition time between the center echo of successive cardiac phases (Temporal Resolution) but no longer represents the repetition time between successive excitation pulses ($TR_{effective}$). The Temporal Resolution in Figure 3B is five times longer than in Figure 3A, although the echo spacing ($TR_{effective}$) is the same in both.

If the center echo is re-sampled between successive segments, and echoes are shared from the prior and next segments, the Temporal Resolution can be improved by reducing the center-spacing between successive phases (Fig. 3C). In an “echo-shared segmented” cine pulse sequence, $TR_{protocol}$ represents the repetition time between the center echo of successive cardiac phases (Temporal Resolution), and is always less than the comparable $TR_{protocol}$ without echo-sharing. In this example of an echo-shared segmented cine pulse sequence, the total number of echoes acquired per repetition is six (5 + 1), however the $TR_{protocol}$ (Temporal Resolution) after echo-sharing is only three echoes (6 : 2).

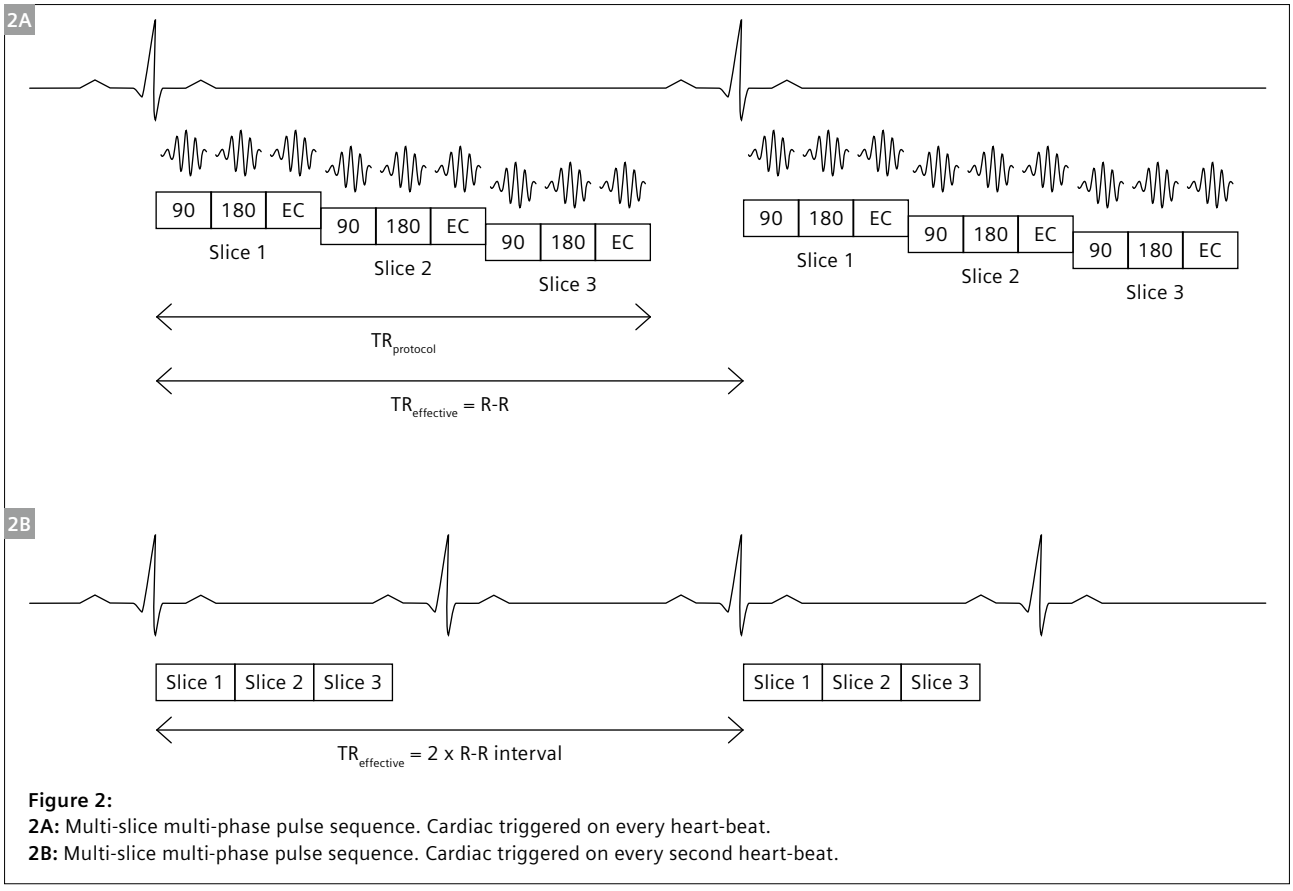

Figure 2:
2A: Multi-slice multi-phase pulse sequence. Cardiac triggered on every heart-beat.
2B: Multi-slice multi-phase pulse sequence. Cardiac triggered on every second heart-beat.

Figures 3D and 3E demonstrate an example of an echo-shared segmented GRE cine pulse sequence.
In this example the total number of echoes acquired per repetition is twenty four (23 + 1), however the effective temporal resolution with echo-sharing is only twelve echoes (24 : 2) with a spacing of 43.32 ms between the centers of successive phases.

- The total number of cardiac phases is 17.
- The number of echoes per phase is 23.
- The temporal resolution per phase is 43.32 ms.

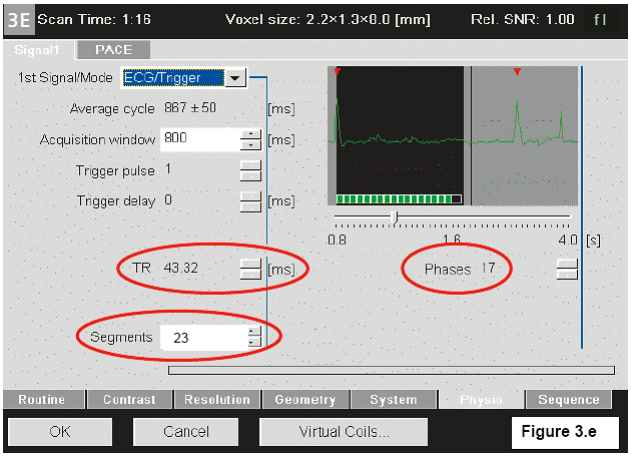

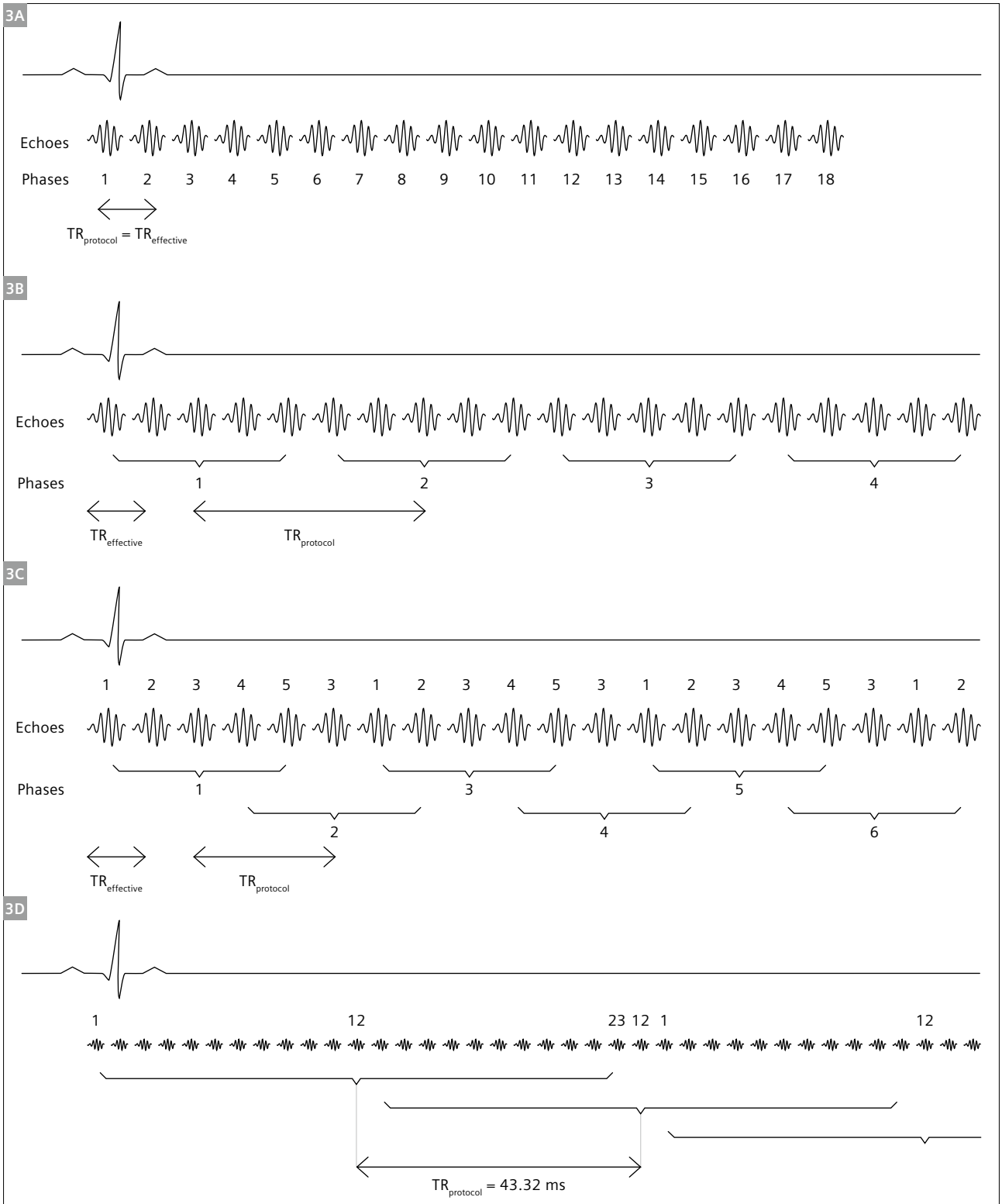

Figure 3:
3A: Cardiac triggered cine pulse sequence. Non-segmented data collection.
3B: Cardiac triggered cine pulse sequence. Segmented data collection.
3C: Cardiac triggered cine pulse sequence. Echo-shared segmented data collection.
3D: Echo-shared segmented GRE sine pulse sequence.

Definition 4

Some cardiac triggered pulse sequences produce a single static image rather than cine images of the heart, and have yet a different definition of $TR_{protocol}$ (Figs. 4A, B). The $TR_{protocol}$ represents the minimum time needed to collect the train of echoes for a single diastolic-triggered segment. You should always set the $TR_{protocol}$ to its minimum possible value in this situation. You can still think of the minimum $TR_{protocol}$ as the Temporal Resolution of the sequence, but there is only one image produced rather than a cine series. This applies to any non-cine cardiac triggered pulse sequence containing no Inversion Recovery (IR) or Saturation Recovery (SR) preparation pulses. Examples of cardiac triggered pulse sequences using this definition of TR include TrueFISP 2D localizers and Flash 2D angiography techniques.

As demonstrated in the *syngo* Physio Taskcard for a segmented TrueFISP 2D localizer pulse sequence (Fig. 4B):

- The total number of echoes in the segment is 41.
- The temporal resolution of the segment is 152.3 ms (green bar).
- The trigger delay prior to the segment is 647 ms (grey bar).

In the previous example of a TrueFISP 2D localizer pulse sequence (Fig. 4B) only 41 echoes were collected per heartbeat, so several heartbeats were required to completely create the image. Such a scheme is known as "segmented" data collection. However, the same pulse sequence could be slightly modified to operate as a "single-shot" data collection in which all the echoes needed to create the image are collected in one long segment within a single heartbeat (Fig. 4C). The temporal resolution is still defined as the minimum time to collect all the echoes (minimum $TR_{protocol}$), but it is much greater than in the previous example because many more echoes are collected in the segment.

As demonstrated in the *syngo* Physio Taskcard for a single-shot TrueFISP 2D localizer pulse sequence (Fig. 4C):

- There is only 1 segment which contains of all the required echoes.
- The temporal resolution of the segment is 343.5 ms (green bar).
- The trigger delay prior to the segment is 456 ms (grey bar).

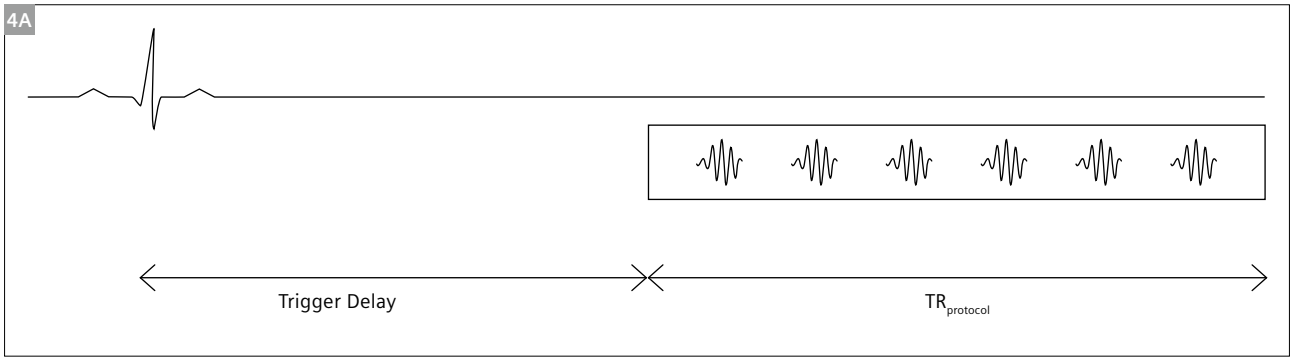

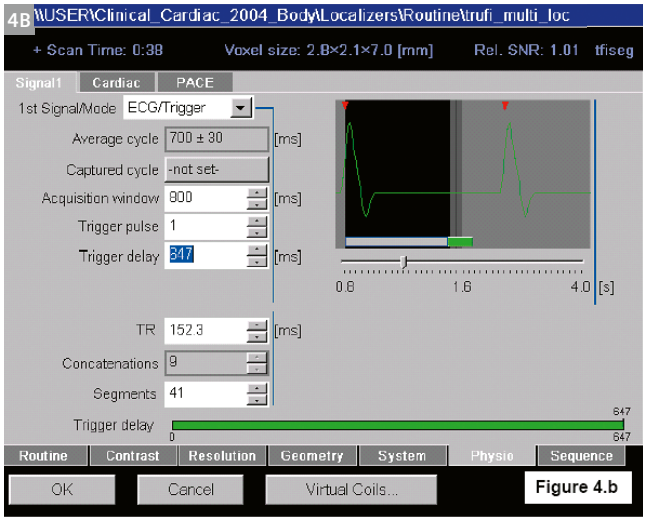

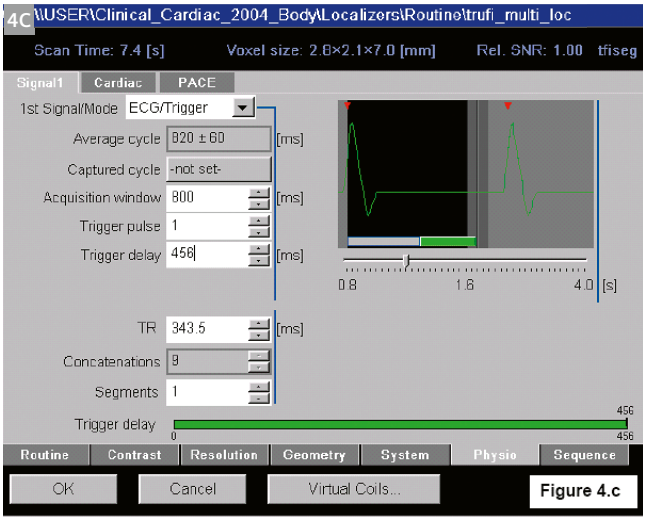

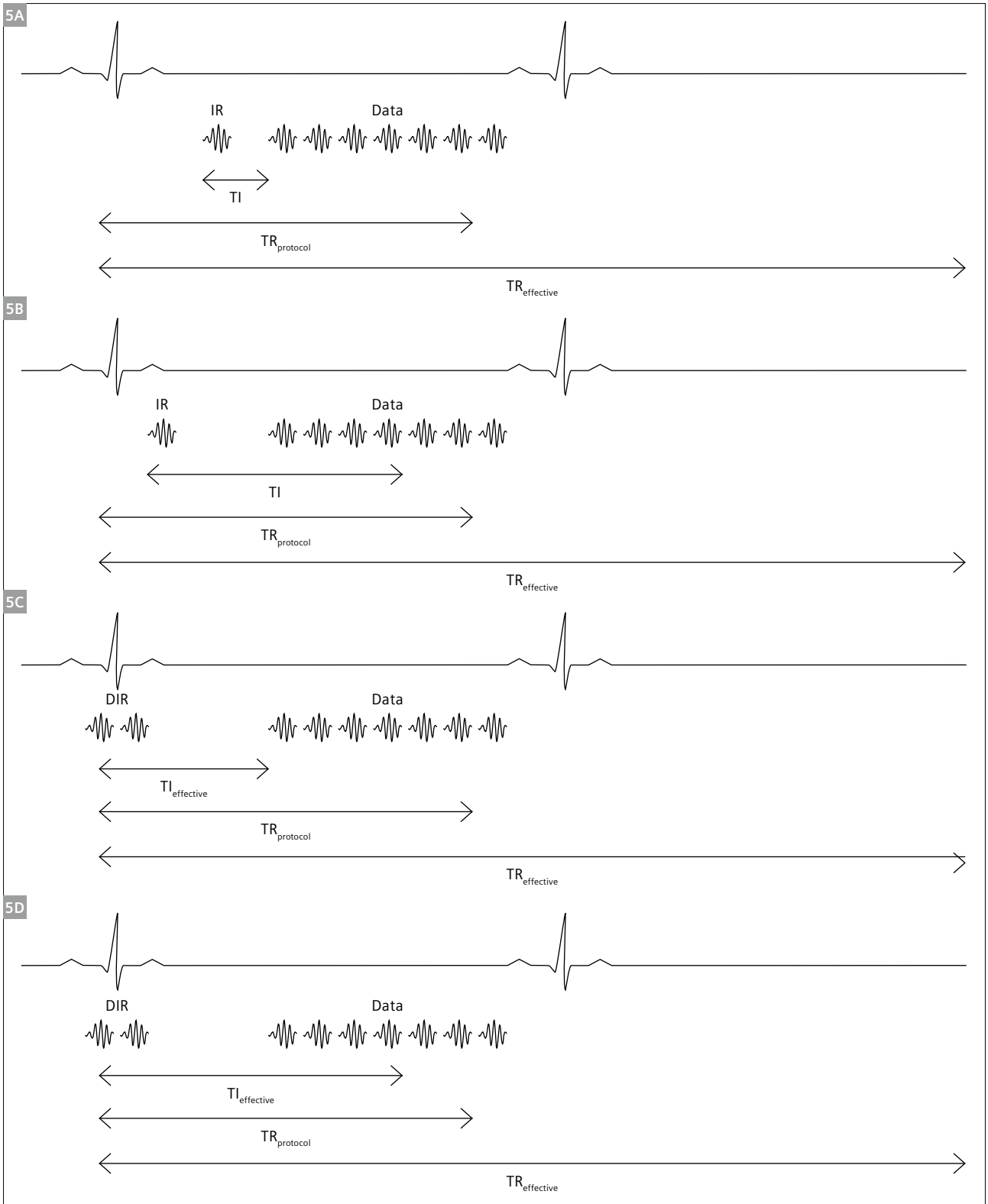

Figure 5:
5A: Cardiac triggered IR TSE pulse sequence. Adjust TI for optimal fat nulling.
5B: Cardiac triggered IR GRE pulse sequence. Adjust TI for optimal myocardial nulling.
5C: Cardiac triggered DB TSE pulse sequence. Adjust $TR_{protocol}$ for optimal blood nulling.
5D: Cardiac triggered DB GRE pulse sequence. Adjust $TR_{protocol}$ for optimal blood nulling.

Definition 5

Yet another definition of TR applies to a cardiac triggered pulse sequence containing an Inversion Recovery (IR) preparation pulse (Figs. 5A, B). The $TR_{protocol}$ is defined as the time between the QRS trigger and the end of the data segment, and is used to adjust the timing of the data segment within the cardiac cycle. In an IR TSE pulse sequence the TI is defined as the time between the IR preparation pulse and the beginning of the data segment (Fig. 5A), and is typically adjusted for optimal fat nulling. In an IR GRE pulse sequence the TI is defined as the time between the IR preparation pulse and the center of the data segment (Fig. 5B), and is typically adjusted for optimal myocardial nulling. In these sequences the data segment is typically acquired every other heartbeat, so the $TR_{effective}$ is twice the R-R interval.

In order to null the signal from flowing blood, we can apply a Double Inversion Recovery (DIR) preparation pulse at the QRS trigger and wait several hundred milliseconds to acquire the data segment in the late diastolic portion of the cardiac cycle (Fig. 5C). The DIR pulse, also known as a Dark Blood (DB) pulse, is available for Turbo Spin Echo, TrueFISP, and TurboFlash pulse sequences. The TR in the protocol ($TR_{protocol}$) is defined as the time between the DB pulse and the end of the data segment. Since there is no TI available in a DB protocol, the $TR_{protocol}$ is used to adjust the location of the data segment for optimal blood nulling. Figure 5C demonstrates a cardiac triggered DB TSE pulse sequence in which the effective inversion delay time for blood nulling ($TI_{effective}$) is measured from the DB pulse to the beginning of the data segment. Figure 5D demonstrates a cardiac triggered DB GRE pulse sequence in which $TI_{effective}$ is measured from the DB pulse to the center of

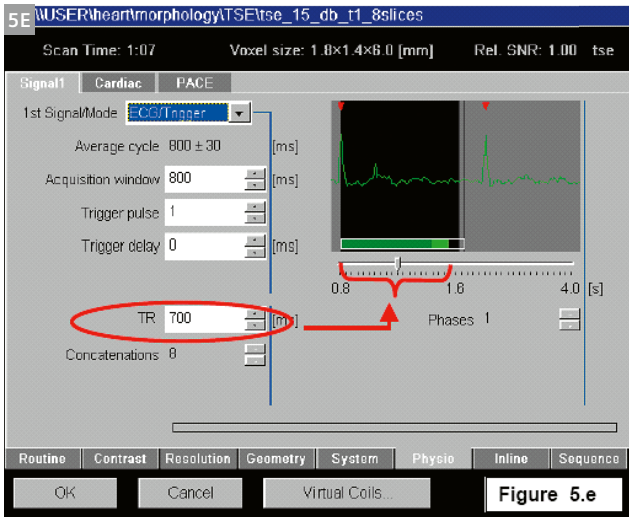

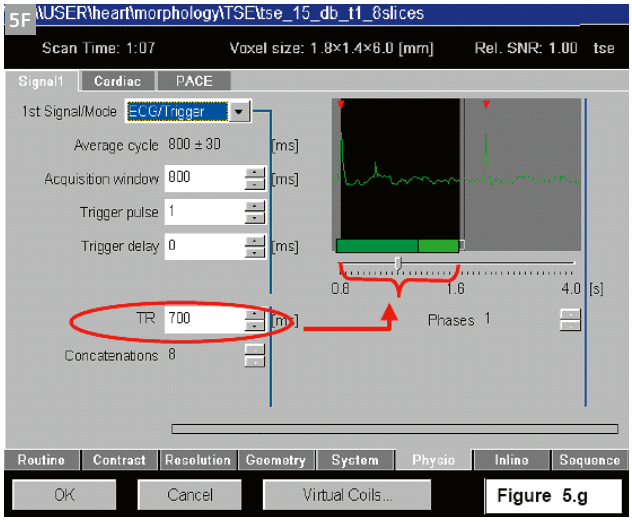

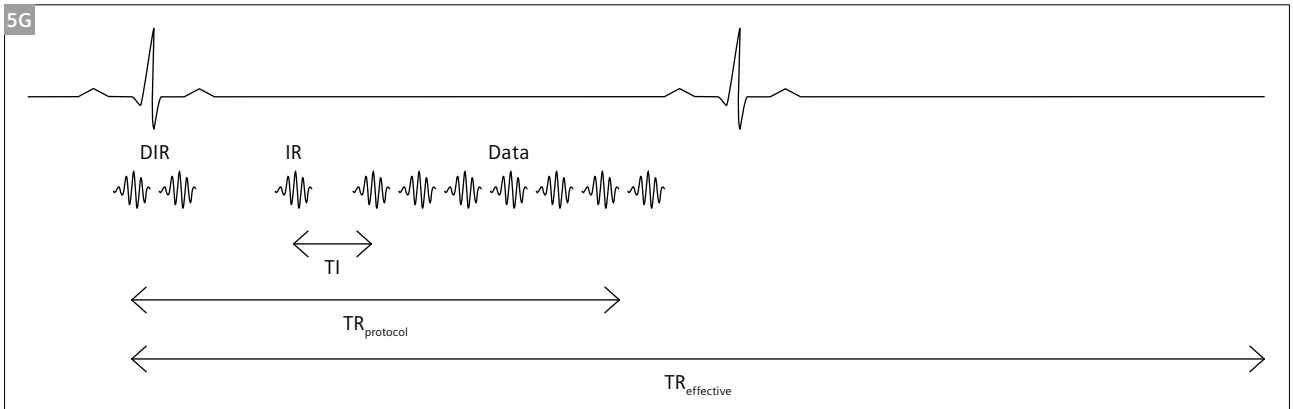

Figure 5:
5G: Cardiac triggered DB STIR pulse sequence. Adjust $TR_{protocol}$ for optimal blood nulling. Adjust TI for optimal fat nulling.

the data segment. In these sequences the data segment is typically acquired every other heartbeat, so the $TR_{effective}$ is twice the R-R interval.

In the example of the *syngo* Physio Taskcard for a DB TSE pulse sequence (Fig. 5E) the TR of 700 ms includes the DB pulse (at the ECG trigger), the inherent inversion delay time (dark-green bar), and the data segment (light-green bar). Trigger delay must be zero because the inversion delay is included within TR.

If we add a third IR preparation pulse to a double IR TSE pulse sequence, we have a Dark Blood STIR pulse sequence (Fig. 5G). $TR_{protocol}$ is adjusted for optimal blood nulling and $TI_{protocol}$ is adjusted for optimal fat nulling. In these sequences the data segment is typically acquired every other heartbeat, so the $TR_{effective}$ is twice the R-R interval.

Figure 5F is an example of the *syngo* Physio Taskcard for a DB STIR pulse sequence. The dark-green bar within the TR includes the Double IR pulse and the inversion delay time for blood nulling. The light-green bar within the TR includes the single IR pulse and the inversion delay time for fat nulling, plus the data segment. Trigger delay must be zero because the inversion delay is included within the TR.

Another example is a FatSat IR Flash 3D pulse sequence for coronary angiography, without a Navigator pulse (Fig. 5H) or with a Navigator pulse (Fig. 5I). The TI is measured from the IR pulse to the beginning of the data segment (centric ordering) and is adjusted for optimal myocardial nulling. The FatSat pulse immediately precedes the data segment. The navigator pulse immediately precedes the FatSat pulse. There is no double IR pulse for blood nulling.

Definition 6

Yet another definition for TR is used in the IR- or SR-prepared GRE (TurboFlash or TrueFISP) pulse sequences (Fig. 6A). These sequences can be used for T1-weighted single-shot imaging that requires multiple slices acquired within a single heartbeat with high temporal resolution. $TR_{protocol}$ consists of the minimum time duration needed for the SR preparation pulse, plus the delay period thereafter, plus the data segment. $TR_{protocol}$ can be thought of as the "time per slice." TI is measured from the IR- or SR-preparation pulse to the center of the data segment, and is adjusted for optimal myocardial signal.

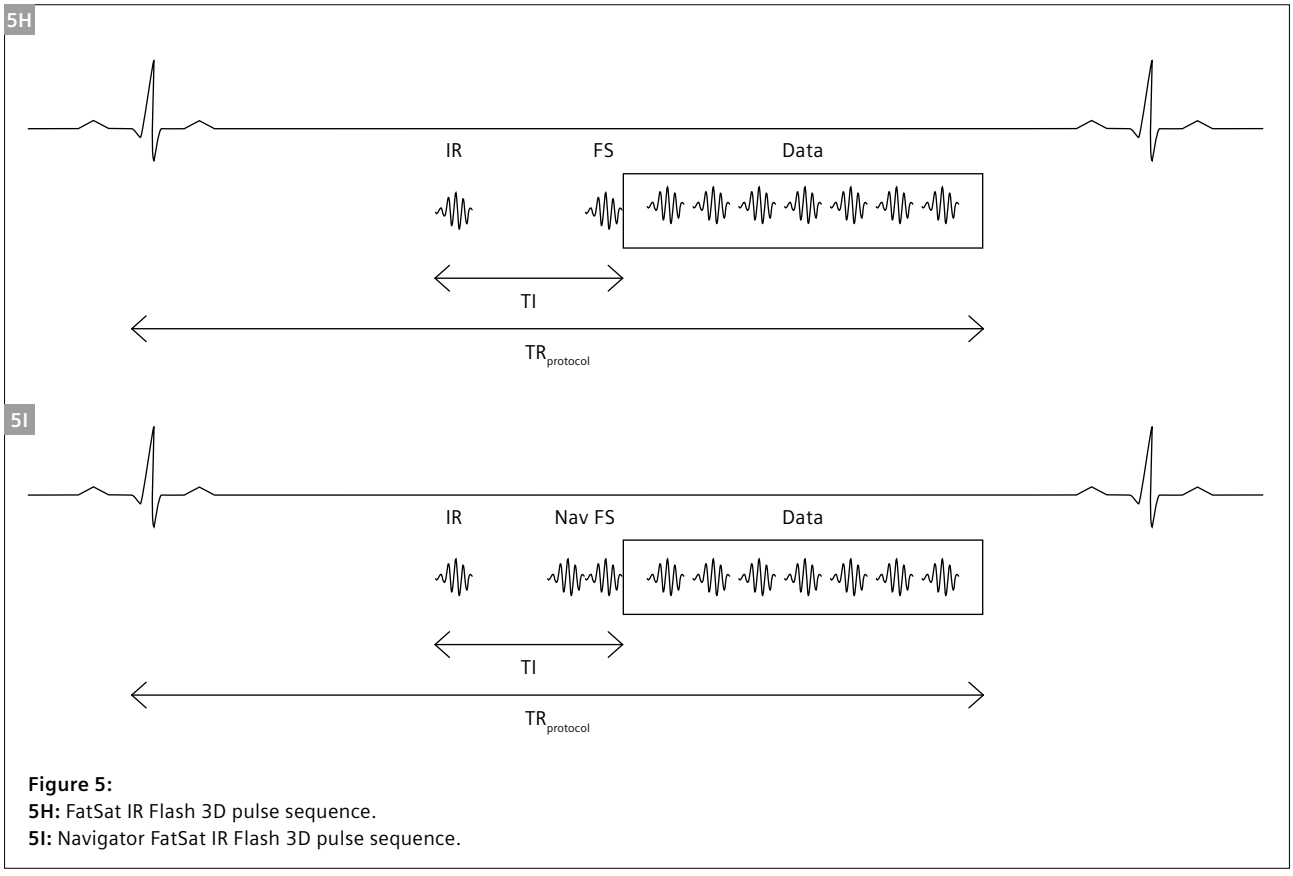

Figure 5:
5H: FatSat IR Flash 3D pulse sequence.
5I: Navigator FatSat IR Flash 3D pulse sequence.

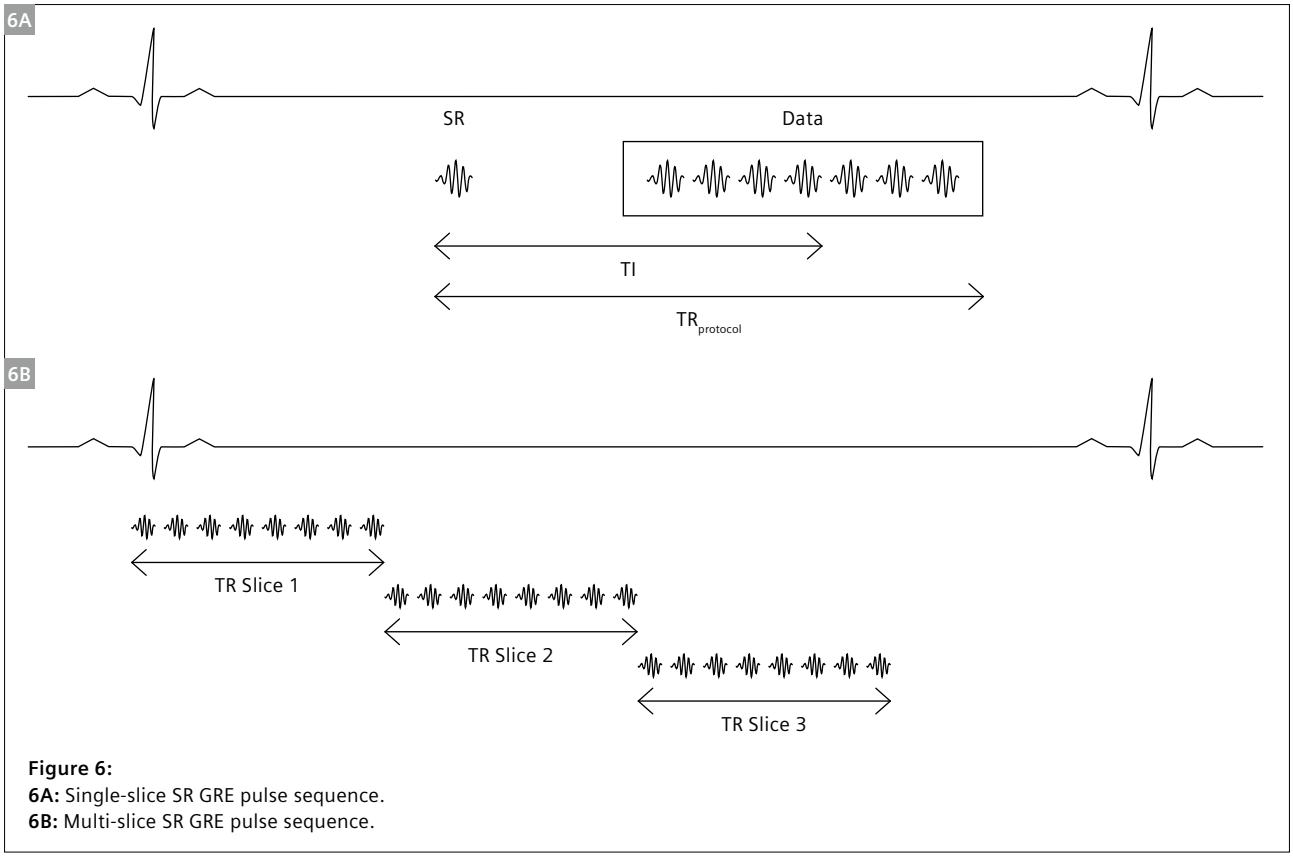

Figure 6:
6A: Single-slice SR GRE pulse sequence.
6B: Multi-slice SR GRE pulse sequence.

SR Data

In an SR GRE pulse sequence the data segment is a "single-shot" of all required echoes for the entire slice. Typically, 3 to 5 slices can be acquired within each heartbeat (Figs. 6B, C).

While the physical definition of TR will always mean only one thing, the time between successive excitation pulses, a number of variations have resulted from the necessity of controlling a pulse sequence within the cardiac cycle. Hopefully, this brief explanation with diagrams will make it a little easier for everyone to understand.

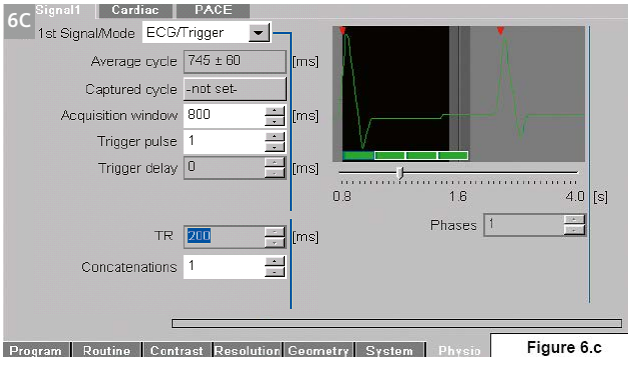

Figure 6.c

Contact

Gary McNeal, MS (BME)
Advanced Application Specialist,
Cardiovascular MR Imaging
Siemens Healthineers
737 N. Michigan Ave, Ste 1600
Chicago, IL, 60611
USA
gary.mcneal@siemens-healthineers.com

Meet Siemens Healthineers

Siemens Healthineers: Our brand name embodies the pioneering spirit and engineering expertise that is unique in the healthcare industry. The people working for Siemens Healthineers are totally committed to the company they work for, and are passionate about their technology. In this section we introduce you to colleagues from all over the world – people who put their hearts into what they do.

Erlangen, Germany

Michaela Schmidt

trained as a radiographer at the University Hospital in Erlangen, Germany. She then went on to work for several years as an MRI research assistant at the University Hospital Zurich, Switzerland. In 1999 she returned to Erlangen to join the cardiovascular MRI group at Siemens Healthineers where she has since been an enthusiastic team member. Michaela works as an application developer for cardiovascular imaging; her main focus lies in the design and development of examination workflows for cardiac MRI scans – Dot Engines, collaborating with clinical partners, and developing and evaluating new imaging technologies. Over the last few years her principle focus has been on applying compressed sensing techniques to cardiovascular MRI.

How did you first come in contact with MRI?
During my training in Erlangen I visited the MR factory where, thanks to Sabine Vitt, we were given a really interesting volunteer demo. It was there and then that I decided that I would like to work in the field of MRI development. As a result, and following a 6-month stint in the X-ray and CT departments of the University Hospital Zürich, I soon switched to the MR section. A few years later I was promoted to the position of MR research assistant, with my main focus on contrast-enhanced MR angiography, postprocessing, and open MRI and interventions.

What is most fascinating about MRI?
MRI never gets boring! Not only can you visualize the whole body in such perfect detail, you can even display most of its functionality, from brain activity to the beating heart. As an application specialist visualizing the heart with MR is especially challenging and interesting. I particularly like working in small interdisciplinary teams with people from different backgrounds to improve the workflow or to create fascinating new ways of seeing inside the heart and great vessels.

What do you think are the most important developments in MRI and in Healthcare?
I find it hard to pick one – it would be biased, I'm afraid. I think for MR the most important developments are those which make scanning faster, more robust and easier to operate. From a healthcare point of view, I believe there should be even more focus on motivating the public to invest in disease prevention. A healthy life style has a significant impact on life expectancy, the quality of life and overall healthcare costs.

Outside of work ...
I love to be outside – in forests, up on top of mountains, in the sea. I enjoy taking walks with my dog, calming my mind with qigong, or maintaining my cardiovascular fitness with running, biking, scuba-diving or skiing. I also like travelling, learning from different cultures and discovering new things.

Carmel Hayes

studied chemistry at universities in Dublin and Glasgow before going on to do a Ph.D. in polymer physics at the Ecole de Physique-Chimie in Paris. Following research positions at the Institut Laue-Langevin in Grenoble, France, and the Institute of Cancer Research in Sutton, UK, she joined Siemens Healthineers in 2001. The main focus of Carmel's current work is in the development of applications for cardiovascular MRI. Together with colleagues and collaborators she transforms new image acquisition, reconstruction and processing methods into commercially-available products. In this role, she maneuvers all of the latest cardiac MR imaging technologies through the product development phase. Carmel's recent projects culminated in the release of PSIR Heart Freeze and Compressed Sensing Cardiac Cine for 3T MAGNETOM Vida and 1.5T MAGNETOM Sola.

Erlangen, Germany

How did you first come in contact with MRI?
I first became interested in spin choreography while working in the field of neutron spin echo spectroscopy. Since there are a number of interesting parallels between neutron and proton spin echoes, I took a chance and applied for a research position as MRI physicist at the Institute of Cancer Research, even though I'd never seen an MRI system in my life before; according to what I read, it sounded just like something I'd like to do. During my first year of acquaintanceship with MRI I must have worked with at least twenty different MRI systems located all over the UK. From my base at the Royal Marsden Hospital in London I was able to get first-hand knowledge of the role MRI plays in the diagnosis and treatment of cancer. Since that decision to switch domains over 20 years ago, I am still a huge MRI fan.

What is most fascinating about MRI?
Magnetic resonance imaging is a highly interdisciplinary modality, with aspects varying from physics to mathematics and statistics, electronic and software engineering, physiology, pharmacokinetics and anatomy, to name but a few. I find this diversity very interesting, there's always something new to do. The images we can now acquire of the human body are of captivating detail, the methods are adaptive to motion; we can see the brain thinking, valves opening and shutting, blood flowing, muscles working. The fact that MRI can be paired with other modalities such as PET, can be used in combination with treatment devices, even during intervention makes it all the more fascinating. As a matter of course, there's nothing more aesthetically pleasing than a four-chamber cine of the heart.

What do you think are the most important developments in MRI and in Healthcare?
Increased diagnostic and therapeutic precision has surely made a huge difference to millions of people's lives. In this respect, imaging modalities such as MRI and CT can themselves be considered major developments in healthcare. MRI has seen many significant improvements over the last few decades, not least, in many cases anyway, due to mathematical discoveries such as compressed sensing.

Outside of work ...
My family, their hobbies, as well my own hobbies keep me rather busy after work. For example, I like making things such as dresses, bags, jackets, the more technically demanding the better. I also get a kick out of fixing and refurbishing smart phones and tablets, lately I tackled a drone. In order to keep myself physically fit I regularly attend pilates classes and I love cycling, swimming, or going for long walks. I especially like competing with relatives in step-counting challenges. Last but not least, I think there's nothing like getting stuck in a good book. I've just finished reading J.M.G Le Clézio's latest novel "Bitna, sous le ciel de Séoul" and am currently having trouble putting down Benedict Well's book "Vom Ende der Einsamkeit" ("The End of Loneliness").

The entire editorial staff at Northwestern University, and at Siemens Healthineers extends their appreciation to all the radiologists, technologists, physicists, experts, and scholars who donate their time and energy – without payment – in order to share their expertise with the readers of MAGNETOM Flash.

MAGNETOM Flash – Imprint

Publisher:
Siemens Healthcare GmbH
Magnetic Resonance,
Karl-Schall-Str. 6, D-91052 Erlangen, Germany

Editor-in-chief:
Antje Hellwich
(antje.hellwich@siemens-healthineers.com)

Guest editor:
James C. Carr, M.D.
Chairman Department of Radiology
Northwestern Medical Group;
Professor of Radiology, Medicine & Biomedical Engineering, Northwestern University, Feinberg School of Medicine

Editorial Board:
Rebecca Ramb, Ph.D.; Sunil Kumar S. L., Ph.D.; Wellesley Were; Gary R. McNeal, MS (BME)

Review Board:
Gaia Banks, Ph.D.; Kelvin Chow, Ph.D.; Daniel Fischer; Christian Geppert, Ph.D.; Christian Schuster, Ph.D.; Efrén Ojeda; Christianne Leidecker, Ph.D.

Copy Editing:
Sheila Regan, Jen Metcalf, UNIWORKS, www.uni-works.org
(with special thanks to Kylie Martin)

Layout:
Agentur Baumgärtner,
Friedrichstr. 4, D-90762 Fürth, Germany

Production:
Norbert Moser,
Siemens Healthcare GmbH

Printer:
G. Peschke Druckerei GmbH,
Taxetstr. 4, D-85599 Parsdorf b. Munich, Germany

Note in accordance with § 33 Para.1 of the German Federal Data Protection Law: Despatch is made using an address file which is maintained with the aid of an automated data processing system.

MAGNETOM Flash is sent free of charge to Siemens Healthineers MR customers, qualified physicians, technologists, physicists and radiology departments throughout the world. It includes reports in the English language on magnetic resonance: diagnostic and therapeutic methods and their application as well as results and experience gained with corresponding systems and solutions. It introduces from case to case new principles and procedures and discusses their clinical potential. The statements and views of the authors in the individual contributions do not necessarily reflect the opinion of the publisher.

The information presented in these articles and case reports is for illustration only and is not intended to be relied upon by the reader for instruction as to the practice of medicine. Any health care practitioner reading this information is reminded that they must use their own learning, training and expertise in dealing with their individual patients. This material does not substitute for that duty and is not intended by Siemens Healthcare to be used for any purpose in that regard. The drugs and doses mentioned herein are consistent with the approval labeling for uses and/or indications of the drug. The treating physician bears the sole responsibility for the diagnosis and treatment of patients, including drugs and doses prescribed in connection with such use. The Operating Instructions must always be strictly followed when operating the MR system. The sources for the technical data are the corresponding data sheets. Results may vary.

Partial reproduction in printed form of individual contributions is permitted, provided the customary bibliographical data such as author's name and title of the contribution as well as year, issue number and pages of MAGNETOM Flash are named, but the editors request that two copies be sent to them. The written consent of the authors and publisher is required for the complete reprinting of an article.

We welcome your questions and comments about the editorial content of MAGNETOM Flash. Please contact us at magnetomworld.team@siemens-healthineers.com

Manuscripts as well as suggestions, proposals and information are always welcome; they are carefully examined and submitted to the editorial board for attention. MAGNETOM Flash is not responsible for loss, damage, or any other injury to unsolicited manuscripts or other materials. We reserve the right to edit for clarity, accuracy, and space. Include your name, address, and phone number and send to the editors, address above.

MAGNETOM Flash is also available online:

www.siemens.com/magnetom-world

Not for distribution in the US

On account of certain regional limitations of sales rights and service availability, we cannot guarantee that all products included in this brochure are available through the Siemens sales organization worldwide. Availability and packaging may vary by country and is subject to change without prior notice. Some/All of the features and products described herein may not be available in the United States.

The information in this document contains general technical descriptions of specifications and options as well as standard and optional features which do not always have to be present in individual cases, and which may not be commercially available in all countries. Due to regulatory reasons their future availability cannot be guaranteed. Please contact your local Siemens organization for further details.

Siemens reserves the right to modify the design, packaging, specifications, and options described herein without prior notice. Please contact your local Siemens sales representative for the most current information.

Note: Any technical data contained in this document may vary within defined tolerances. Original images always lose a certain amount of detail when reproduced.

Siemens Healthineers Headquarters
Siemens Healthcare GmbH
Henkestr. 127
91052 Erlangen, Germany
Phone: +49 9131 84-0
siemens-healthineers.com

Published by Siemens Healthcare GmbH · Order No. A91MR-1000-137M-7600 · Printed in Germany · 6823 01190.5 ·